UNIVERSIDADE DE LISBOA
FACULDADE DE CIÊNCIAS
DEPARTAMENTO DE FÍSICA

An optical metrology system for the measurement of the refractive index of glass

Inês Meira Leite

Mestrado Integrado em Engenharia Física

Dissertação orientada por:
Dr. Alexandre Pereira Cabral

2020

Dedicado aos meus pais, irmão e avó.

Agradecimentos

Em primeiro lugar, gostaria de dar o meu profundo agradecimento ao meu orientador, Dr. Alexandre Cabral, que com o seu vasto e profundo conhecimento (e infinita paciência) me guiou, e sem o qual este trabalho nunca teria sido possível. Muito obrigada.

Gostaria também de deixar o meu agradecimento a toda a equipa do Laboratório de Óptica Lasers e Sistemas do Departamento de Física da Faculdade de Ciências pelo apoio de alguma forma prestado ao longo do trabalho. Destaco também a ajuda prestada pelo Dr. João Coelho, nas simulações em Zemax e a quem também deixo o meu muito obrigada.

Por último, mas não menos importante, gostaria de agradecer à minha família – aos meus pais, Maria José Leite e Armindo Leite, irmão Ricardo Leite e avó Mariana Lopes – pelo contínuo amor e apoio incondicional, sem o qual nunca chegaria tão longe. Aos meus amigos, cada um com sua maneira especial, pelo apoio e motivação dados – obrigada.

Muito obrigada a todos.

Resumo

A medição do índice de refracção de amostras de vidro é uma actividade comum e fundamental em muitos domínios de especialidade – pode ser necessário conhecer o valor do índice de refracção de forma a melhor caracterizar o vidro para diferentes aplicações específicas. Por exemplo, o grupo VICARTE solicitou ao grupo de investigação em óptica a medição do índice de refracção de amostras, por eles feitas, de concentradores solares luminescentes. Este tipo de vidros, dopados com um material capaz de absover radiação ultravioleta pode ser aplicado como um concentradores solar – a sua eficiência está no entanto directamente ligada ao valor do índice de refracção.

Apesar de ser possível efectuar medições simples com equipamento normalmente existente no laboratório, por exemplo utilizando a simples refracção, geralmente não é o suficiente, e instrumentos dedicados para este tipo de medições, com uma incerteza razoável, normalmente têm uma complexidade mais elevada. Não sendo portanto possível realizar este tipo de medições com os requisitos necessários surgiu a ideia de se tentar construir um sistema para esta finalidade. Algumas das técnicas de medição do índice de refracção, que têm sido aplicadas ao longo de décadas, podem actualmente não ser as mais viáveis ou eficientes – algumas podem não se enquadrar tão bem com equipamento disponível, podem também ser mais complexas do que o pretendido ou até mesmo serem inadequadas (relativamente ao tipo de amostras que conseguem analisar, por exemplo).

Esta tese visa portanto explorar os métodos existentes, adaptando e optimizando um para ser utilizado em ambiente de laboratório com a maior precisão possível. Uma vez que a medição do índice de refracção tem vários métodos estabelecidos, o desafio centrou-se na criação de um sistema optimizado capaz de fornecer resultados com uma incerteza igual ou melhor do que 10^{-2}. As medições por ele efectuadas podem ter outras aplicações úteis no laboratório óptico: a verificação das propriedades de amostras testemunha (amostras de materiais e/ou revestimentos ópticos usados para testar as propriedades ou o desempenho, sem utilizar o componente real) e a determinação das propriedades de componentes ópticos (úteis para determinar um bom substituto quando a informação sobre o original não está disponível).

O primeiro passo foi então fazer um estudo do estado da arte e construir modelos teóricos baseados em técnicas com potencial a implementar na medição do índice de refracção de amostras de vidro, opticamente simples e de placas paralelas. Os modelos teóricos serviram também para auxiliar na identificação dos principais parâmetros que contribuiam para o valor da incerteza associada ao valor do índice de refracção medido. A medição do índice de refracção do vidro utiliza conceitos simples em óptica e, como já foi dito, existem vários métodos para o fazer – com base na reflexão ou transmissão da luz das superfícies, entre eles o desvio do feixe de refracção, interferometria, reflectometria e elipsometria. A partir da informação recolhida, ficou claro que o sistema iria ser implementado recorrendo a um de dois métodos que asseguravam uma implementação de reduzida complexidade – através do desvio lateral (do feixe refractado) ou de uma técnica simples de interferometria.

Após testar experimentalmente os dois métodos com maior potencial a implementar, de acordo com um conjunto de objectivos previamente estabelecidos, desvio lateral e interferometria, o primeiro foi seleccionado para implementar o sistema. Foi construída uma configuração e todos os parâmetros foram exaustivamente testados sendo que, através da utilização de um balanço de incerteza, a incerteza das medições foi cuidadosamente monitorizada a vários níveis – desde certificados de calibração dos componentes utilizados, passando também por estudos específicos de desempenho e modelos teóricos. Assegurando que o sistema seria capaz de fornecer resultados com a incerteza especificada, foi desenvolvido um programa de software em LabVIEW, capaz de controlar o equipamento e adquirir

dados automaticamente – os dados recolhidos são exportados para um Excel personalizado que automaticamente calcula o valor do índice de refracção, sendo também calculado os valores da incerteza e erro associados.

Para validar e calibrar as medições feitas pelo sistema, foram utilizadas amostras conhecidas e calibradas, pelo que apenas depois dos resultados obtidos pelo sistema estarem em conformidade com a informação fornecida, validando efectivamente o sistema, o mesmo pôde ser empregue na análise das restantes amostras disponíveis. O sistema é capaz de fornecer resultados com uma incerteza de 10^{-3} (amostras ópticas de média qualidade) a 10^{-4} (amostras de calibração, de alta qualidade).

A optimização, baseada na análise rigorosa do sistema nas suas várias vertentes e respectivas incertezas associadas, permitiu obter resultados na ordem de 10^{-4}, uma ordem superior ao que inicialmente se esperava apenas com base no estudo do estado da arte. Algumas melhorias podem ser feitas no futuro, no entanto, o sistema está pronto para ser utilizado em ambiente de laboratório.

Palavras-chave: Índice de Refracção, Deslocamento Lateral, Metrologia, Óptica, Vidro

Abstract

The measurement of the refractive index of glass samples is a common and fundamental activity in numerous fields of expertise – depending on the application, other information can be linked to the value of the refractive index. As the measurement techniques have been employed over decades, some may no longer be as viable or as efficient – this thesis aims therefore to explore existing methods and to adapt and optimize one to be used in a lab environment with the highest possible accuracy.

Since the measurement of the refractive index has several established methods, the challenge of this thesis focused on creating an optimized system capable of providing results with an uncertainty equal or better than 10^{-2}. The measurements made by it can have multiple useful application in the optics lab: the verification of witness sample or coatings properties and the determination of optical component properties (useful to determine a good replacement when information about the original is not available).

The first step was then to make a study of the state of the art and construct theoretical models based on techniques with potential to be implemented in the measurement of the refractive index of paralleled plate glass samples. The theoretical models also served to identify and study the influence of the main parameters of the technique in the uncertainty budget of the measurements. The measurement of the refractive index of glass uses simple concepts in optics and as it has been said, there are several methods to do so – based on the reflection or transmission of light from surfaces, among them refraction beam deviation, interferometry, reflectometry and ellipsometry.

After experimentally testing the two methods with the most potential to be implemented, in accordance to a set previously established objectives, lateral displacement and interferometry, the first was selected to implement the system. A setup was constructed and all parameters were extensively tested and, through the use of an uncertainty budget, the uncertainty of the measurements was carefully monitored. Ensuring that the system would be able to provide results with the specified uncertainty, a software program was developed in LabVIEW, capable of controlling the equipment and acquiring data automatically – the collected data was then transposed to a custom made Excel that finds the value of the refractive index and its associated uncertainty and error were known.

To validate and calibrate the measurements made by the system, known samples were used and only after obtaining favourable results were the remaining unknown samples be measured. The system is able to provide results with an uncertainty from 10^{-3} (medium quality optical samples) to 10^{-4} (high quality calibration samples).

The optimization, based on the rigorous analysis of the system as a whole and its associated uncertainties, made it possible to achieve results in the range of 10^{-4}, one order higher than what was initially expected based on the study of the state of the art. Some improvements can be made in the future, but nonetheless, the system is ready to be employed in a lab environment.

Keywords: Refractive Index, Lateral Displacement, Metrology, Optics, Glass

Contents

Agradecimentos III
Resumo IV
Abstract VI
Contents VII
List of Figures IX
List of Tables XV
List of Abbreviations, Acronyms and Symbols XVI
1. Motivation, Objectives and Approach 1
2. Introduction 3
2.1 Glass and its refractive index 3
2.2 Refractive index measurement techniques 4
2.2.1 Refraction 4
2.2.2 Interferometry 6
2.2.3 Comparison of available techniques 7
3. Analysis of candidate techniques for refractive index measurement 10
3.1 Lateral Displacement 10
3.2 Michelson Interferometer 14
3.3 Experimental Implementation 18
3.3.1 Lateral Displacement 19
3.3.2 Michelson Interferometer 19
3.4 Trade-off analysis 21
4. Refractive Index of Glass by Optimized Lateral Displacement 24
4.1 Uncertainty Budget 25
4.2 Lateral displacement uncertainty components 29
4.3 Glass plate thickness uncertainty components 34
4.4 Angle of incidence uncertainty components 35
4.4.1 Glass plate wedge effect uncertainty component 40
5. GOLD Control System, Data Acquisition and Processing 43
5.1 GOLD Control System and Data Acquisition 44
5.1.1 Phase I: Camera Configuration & Sample Alignment 44
5.1.2 Phase II: Lateral Displacement Position Acquisition 48
5.2 GOLD Data Processing 50
6. GOLD System Calibration 54

7. Measurement of unknown samples 57
7.1 Unknown Lab Samples 57
7.2 LSC Samples 61
8. Conclusions and future work 69
9. Bibliography 71
10. Annex 73
10.1 LabVIEW Codes 73
10.2 Processing of data acquired from GOLD system 80
10.3 Published Work 84

List of Figures

Figure 2.1 – Main techniques and the basic principles used in each to determine the refractive index of samples. 4

Figure 2.2 – Simple schematic drawing of the lateral displacement d suffered by the beam (with incident angle θi) when it passes through a glass plate of thickness t. 5

Figure 2.3 – Beam deflection, δ, by a prism with an apex angle α, with an incident angle θ_i and output angle β. 6

Figure 2.4 – Working principle of a Michelson interferometer. An interference pattern is created based on the splitted beam optical path difference by introducing an additional distance of δL to one of the interferometers' arms. 6

Figure 2.5 –Illustration of some techniques used to determine the refractive index of glass samples, in terms of their complexity and the associated uncertainties. 8

Figure 3.1 – Lateral displacement, d, in a 2D sensor (camera), of the beam with an incident angle θi, by a glass sample with a thickness t. 10

Figure 3.2 – Simulation of the expected results of the lateral displacement of the beam (a) and associated refractive index of glass (b) in an ideal, error free, environment, considering a glass plate with 10mm thickness, $\theta i = [-30; 30]°$ and an initial value for the RI of glass of 1.50. 11

Figure 3.3 – Analysis of the impact of an offset in the three variables needed to know in order to determine the RI of glass. Top, introduction of an offset in the incident angle, θ_i. Middle, introduction of an offset in thickness of the sample, t. Bottom, introduction of an offset in the lateral displacement, d. 12

Figure 3.4 – Top: Schematic of a Michelson interferometer (a) and the OPD created by the glass sample (b). Bottom: Schematic of the beam path with an incident angle θ_i in the glass sample (with refractive index $nglass$) surface and chosen variables to associate the OPD with the RI. 14

Figure 3.5 – Top: Simulation of the expected results of the OPD between the two arms of the interferometer (a) and associated refractive index of glass (b) in an ideal, error free, environment, considering a glass plate with 10 mm thickness, $\theta i = -30; 30°$ with 1° steps, an initial value for the RI of glass of 1.50 and L = 10 cm (distance between the first glass surface and the mirror)). Bottom: Number of fringes produced with respect to the angle of incidence in the glass sample. 15

Figure 3.6 – Analysis of the impact of an offset in the three variables needed to know in order to determine the RI of glass. Top, introduction of an offset in the incident angle, θ_i. Middle, introduction of an offset in thickness of the sample, t. Bottom, introduction of an offset in the optical path difference, OPD. 17

Figure 3.7 – Experimental setup (a) of the system. It is composed by a laser, beam splitter, two mirrors, rotating stage and glass sample, a camera, a lens and a detector (b, bottom). The 2D sensor can be deviated from the beam path, adding or removing it from the setup as necessary (b, top). 18

Figure 3.8 – Left: Spot image captured by the 2D CMOS sensor with the setup as shown in Figure 3.7. Interference can be seen due, mainly, to internal reflections in components along the beam path. 19

Figure 3.9 – Captured signal when the sample is rotated from $\theta i = -\alpha$ to $\theta i = \alpha$, with $\alpha \lesssim 5°$(a, $\theta i \neq 0°$, b, $\theta i \approx 0°$) – on the right (c) is the registered signal in the oscilloscope for this rotation. 20

Figure 3.10 – Signal captured when light taps are made on the breadboard. 21

Figure 3.11 – Evaluation of the uncertainty (u.), with the lateral displacement technique, of the measurements of θ_i, t and d, respectively, required to keep the uncertainty of n_{glass} equal or below 1%. 21

Figure 3.12 – Evaluation of the uncertainty (u.), with the interferometer technique, of the measurements of θ_i, t and OPD, respectively, required to keep the uncertainty of n_{glass} equal or below 1%. 22

Figure 4.1 – Optimized Lateral Displacement system setup (left) and operating principle (right). 24

Figure 4.2 – Main component sources and their weight (in percentage), that contribute to the uncertainty in the measurements of the RI, associated to each parameter. The achievable magnitude of uncertainty, for every component, is indicated between brackets. 29

Figure 4.3 - Motion induced pattern shift in the captured spot image using the glass neutral density optic filter. 30

Figure 4.4 – (a) Top: Camera setup with a ND6 filter adapted at the end of a 80mm opaque tube; Bottom: image before and after the application of the tube). Captured images using an optical neutral glass filter (b) and an optical neutral film filter (c). 30

Figure 4.5 – Experimental setup (left) to verify the accuracy of spot measurements by two different methods (Centroid and Gaussian fit) over the camera area (right), where blue dots illustrate the measuring sweep along the x axis, for three different vertical positions. 31

Figure 4.6 - Summary of the standard deviation shift (in mm) in each data set obtained in the study to determine the best method to find the centre coordinates of the laser spot. Purple markers represent results obtained for three different vertical positions with a distance between laser source and camera of 25 cm and green markers represent 50 cm. 32

Figure 4.7 – Step deviation value for three horizontal sweeps in three different vertical positions (blue, red and green dots) for two values of L. 32

Figure 4.8 – Fitted model and associated equation (red) used to define the uncertainty in the accuracy of measurements made by the camera (blue). 33

Figure 4.9 – Standard deviation of the lateral displacement, for five sweeps and wide angles, without tampering with the sample. 33

Figure 4.10 – Left: Rotation of the glass sample creates an optical path difference (only visible in the left image at the entry and exit laser points). Right: Top view schematic of the GOLD setup. 35

Figure 4.11 – Study of the spot position shift in the y coordinate (left) or x coordinate (right) by rotating a 10mm thick sample x or y axis, respectively, from -30º to 30º..... 36

Figure 4.12 – Acquired data (red line) over the camera area in ideal conditions (a) and the influence of a tilt in the y axis (b) and x axis (c)..... 36

Figure 4.13 – Sample suitability to the sample holder. (a) round calibration samples and no detected problems. (b) square LSC sample, difficult to secure in sample holder. (c) small square LSC sample adapted with parts to stay in place..... 37

Figure 4.14 – Alignment of the beam with the help of the diaphragm and transmitted image. (a) the diaphragm is completely open; (b) the diaphragm is closed and a reflection by the glass surface can be seen (pink spot); (c) the diaphragm is closed, and the sample is correctly aligned. 38

Figure 4.15 – Section of the LabVIEW user interface that helps the user set the laser spot zero (x_0 ; y_0) in real time, with an accuracy up to 0.1 pixel..... 38

Figure 4.16 – Plotted data of the measured values for the RI of the sample. The middle 50% of the measurements not used for the calculation of the difference between left and right averages of the RI..... 39

Figure 4.17 – Three point plot of the value of df from three sets of results. The angle offset corresponds to $df = 0$ (red dot)..... 40

Figure 4.18 – Beam path crossing a sample with a wedge (proportional to α) (left) and its influence in the measurement of the lateral displacement (right). 40

Figure 4.19 – Study of the spot position shift in the y coordinate due to the introduction of a wedge in the sample of, respectively, +0.01º (top), +0.1º (middle) and +1º (bottom). 41

Figure 5.1 – Process diagram of the steps that need to be performed to obtain the value of the RI of a glass sample. The blue dashed squares indicate steps assisted by the LabVIEW user interface..... 43

Figure 5.2 – Simplified block diagram of the LabVIEW program behaviour to carry out measurements of the xy coordinates (centroid) of the spot..... 44

Figure 5.3 – First page of the front panel of the program in which the user can interact. The user made configurations of the camera and sample in this first phase influence the measurements made in the second phase of the code..... 45

Figure 5.4 – Steps to perform (yellow arrows) , and influence of the parameters, to achieve an adequate image spot for lateral displacement measurements..... 46

Figure 5.5 – Sample alignment: (Left) LabVIEW interface that allows the setting of the spot zero coordinates Zx and Zy and monitors the pixel difference with the current coordinates. (Centre) Sample's x axis alignment. (Right) Mechanical piece of the setup that allows the user to tilt the sample's y axis..... 47

Figure 5.6 – Alignment of the laser spot (x ; y) after the sample is placed in the sample holder by comparison with the spot zero coordinates (x_0 ;y_0)..... 48

Figure 5.7 – Second page of the front panel of the program in which the user can interact. The user needs to specify three parameters for the measurements, as well as the name of

the file that will be created. The spot position can always be monitored, and a progress bar and estimated time left can be viewed. 49

Figure 5.8 – Top: One cycle measurements of the refractive index versus the incident angle, of the calibrated N-BK7 sample. Bottom: Measurements used for the computation of the average n_{glass} value. 50

Figure 5.9 – Difference in the shape of the laser spot, captured by the camera, between HQ (left: N-BK7) and LQ (right: LSC Sn) samples. 51

Figure 5.10 – One cycle measurements of the refractive index versus the incident angle, of the LSC Sn sample. 51

Figure 5.11 – Data processing by the excel spreadsheet, developed to find the value of the refractive index (and associated uncertainty) of a glass sample. 52

Figure 5.12 – Schematic of the followed procedure to measure the refractive index of a calibrated sample. 53

Figure 6.1 – Refractive index data related to uncoated N-BK7 (left) and UVFS (right) precision windows [credit:Thorlabs]. 54

Figure 6.2 – Calibration samples used to validate system results, UVFS (left) and N-BK7 (right). 55

Figure 6.3 – Left: 10 measurements (orange dots) and associated individual uncertainty (black bars) of the refractive index of N-BK7and their comparison with the resulting average and uncertainty (blue solid line and blue dashed lines, respectively) and known expected value (red). Right: Comparison between the 10 value average (Measured) and the known value (Expected) for the refractive index of the N-BK7 precision window. 55

Figure 6.4 – Left: 10 measurements (orange dots) and associated individual uncertainty (black bars) of the refractive index of UVFS and their comparison with the resulting average and uncertainty (blue solid line and blue dashed lines, respectively) and known expected value (red). Right: Comparison between the 10 value average (Measured) and the known value (Expected) for the refractive index of the UVFS precision window. 56

Figure 7.1 – Unknown tested samples, later identified as B270 glass (a) and Fused Silica (b). Sample surface (left) and sample thickness (right). 58

Figure 7.2 – Tested surface area of samples (red dots representing the laser beam position) according to its shape and compatibility with the sample holder. 58

Figure 7.3 – Ten measurements of the samples Fused Silica (?) (left) and B270 (?) (right) refractive index (orange) with associated individual uncertainty (black bars). The resulting average and uncertainty (blue line solid and dashed, respectively) are compared to the known expected value for the RI (red line). 59

Figure 7.4 – Tested acrylic sample with unknown refractive index. Sample surface (left) and sample thickness (right) 60

Figure 7.5 – Ten measurements of acrylic refractive index of the acrylic sample (orange) with associated individual uncertainty (black bars). The resulting average and uncertainty are depicted by blue lines: solid and dashed, respectively. 60

Figure 7.6 – Total internal reflection of a beam. 61

Figure 7.7 – Basic principles of using LSC glass to produce solar energy. 62

Figure 7.8 – Untested LSC samples: LSC Eu (a) and LSC Cu (b), sample surface (left) and sample thickness (right)..... 63

Figure 7.9 – Tested LSC samples, LSC Vidro de Janela (a) and LSC Branco Vidro Float (b), with consistent value results of its refractive index. Sample surface (left) and sample thickness (right). 63

Figure 7.10 – Five measurements of the samples LSC Vidro de Janela (left) and LSC Branco Vidro Float (right) refractive index (orange) with associated individual uncertainty (black bars). The resulting average and uncertainty are depicted by blue lines: solid and dashed, respectively. 64

Figure 7.11 – Results comparison between LSC samples Vidro de Janela (red circles and red uncertainty bars) and Branco Vidro Float (blue squares and blue uncertainty bars). Both sample result averages are represented by solid lines and associated uncertainty intervals in dashed lines (with the same colours). 64

Figure 7.12 – Tested LSC samples, from top to bottom LSC Sn, LSC Sample51 Mn and LSC Sample40 Mn, with more inconsistent value results of its refractive index. Sample surface (left) and sample thickness (right). 65

Figure 7.13 – Five measurements of the sample LSC Sn refractive index (orange) with associated individual uncertainty (black bars). The resulting average and uncertainty are depicted by blue lines: solid and dashed, respectively. 66

Figure 7.14 – Ten measurements of the samples LSC Sample51 Mn (left) and LSC Sample40 Mn (right) refractive index (orange) with associated individual uncertainty (black bars). The resulting average and uncertainty are depicted by blue lines: solid and dashed, respectively..... 66

Figure 7.15 – Results comparison between LSC samples Sample51 Mn (red circles and red uncertainty bars) and Sample40 Mn (blue squares and blue uncertainty bars). Both sample result averages are represented by solid lines and associated uncertainty intervals in dashed lines (with the same colours). 67

Figure 10.1 – Block diagram of the sub .vi in LabVIEW for the Moving Average filter. 73

Figure 10.2 – Block diagram of the sub .vi in LabVIEW for the Threshold filter. 74

Figure 10.3 – LabVIEW code to calculate the centroid of an input 2D array. On the left corner in a box is the LabVIEW .vi that contains the code. 74

Figure 10.4 – Block diagram of the first case structure executed by the program. Both the camera and the stage are initialized and a while loop continuously displays the captured image (real time), allowing the user to change some parameters. 76

Figure 10.5 – Block diagram of the first frame of the second case structure executed by the program. The program allows the user to change some parameters, and accordingly updates others automatically. This loop ends when the user presses the button that initiates the automatic measuring procedure. 77

Figure 10.6 – Block diagram of the second frame of the second stacked case structure. Two for cycles are nested, the first sets the stage to the lower limit of the sweep and the second

(here depicted with the first frame of its case structure) moves the stage an implemented step forward, while also calculating the current progress and estimated time left. 78

Figure 10.7 – Block diagram of the third frame of the second stacked case structure. Two for cycles are nested, the first sets the stage to the lower limit of the sweep and the second (now showing the second frame of its case structure) captures an image, determines its centroid coordinates and creates a new data row in the data array later used to determine the values of d..... 79

Figure 10.8 – Excel spreadsheet where the user inserts the sample thickness and spot centre coordinate measurements. 80

Figure 10.9 – Excel spreadsheet that calculates the lateral displacement, refractive index and angle offset for one sweep. 81

Figure 10.10 – Excel spreadsheet that calculates average value and expanded uncertainty of the refractive index, for one sweep. 82

Figure 10.11 – Excel spreadsheet that displays the results of every sweep and calculates the average, uncertainty and error of the refractive index, of a 5 sweep test. 83

List of Tables

Table 2-1 – Summary of some of the researched methods and techniques relevant to the determination of the refractive index of a glass plate. Each technique is categorized according to: the method used, the obtained uncertainty in the refractive index n, its (qualitative) degree of overall complexity and its possibility of optimization. 7

Table 3-1 – Summary of the main advantages and disadvantages of each technique – Lateral Displacement and Interferometry. 23

Table 4-1 – Type A or Type B uncertainty evaluation, associated probability distributions and standard uncertainty formulas..... 26

Table 4-2 – Example of an uncertainty budget table used to estimate the weight of every parameter associated with the measurement of the refractive index of a 12.046 mm thick glass sample. 28

Table 4-3 – Sources of uncertainty, uncertainty evaluation process, value, type and weight in the uncertainty of RI measurements, linked to the lateral displacement d parameter. 34

Table 4-4 – Sources of uncertainty, uncertainty evaluation process, value, type and weight in the uncertainty of RI measurements, linked to the sample thickness t parameter. 35

Table 4-5 – Properties of the three sets associated to 1 cycle of measurements made by the rotation stage. Three different values of df are obtained, making it possible to create a plot in order to determine the angular offset. 39

Table 4-6 – Sources of uncertainty, uncertainty evaluation process, value, type and weight in the uncertainty of RI measurements, linked to the incident angle θ_i parameter. ... 42

Table 5-1 – Captions for Figure 5.3. The numbered red squares in the figure are linked to the Number column, and each represents a sub module briefly described in this table. 47

Table 5-2 – Captions for Figure 5.7. The numbered red squares in the figure are linked to the Number column, and each represents a sub module described in this table. 49

Table 6-1 – System results for the measurement of the refractive index of the two calibrated glass precision windows from Thorlabs, N-BK7 and UVFS, for a coverage level $k = 2$ and a confidence level of 95%. 56

Table 7-1 – System results for the measurement of the refractive index of the three unknown lab samples, Fused Silica, B270 and Acrylic, for a coverage level $k = 2$ and a confidence level of 95%. 60

Table 7-2 – System results for the measurement of the refractive index of the five viable LSC samples: LSC Vidro de Janela, LSC Branco Vidro Float, LSC Sn, LSC Sample40 Mn and LSC Sample51 Mn, for a coverage level $k = 2$ and a confidence level of 95%..... 67

List of Abbreviations, Acronyms and Symbols

Abbreviations / Acronyms

RI…… Refractive Index

LSC …… Luminescent Solar Concentrator

TIR …… Total Internal Reflection

OPD…… Optical path difference between the two interferometer arms

MI……... Michelson Interferometer

UVFS…….. UV Fused Silica

LQ……... Low quality

HQ……... High quality

Symbols

n…….Refractive index of a medium …… –

c…….Velocity of light in vacuum…….…… m/s

v…….Velocity of light in a medium…..…….…… m/s

θ_i……Incident angle between the laser beam and the glass surface …… º

θ_r……Refraction angle between the laser beam and the glass surface …… º

t ……....Thickness of the glass sample …… mm

d ……....Lateral displacement of the laser beam after crossing the glass sample … mm

n_{air}…....Refractive index of air …… –

n_{glass}.....Refractive index of the glass sample …….. –

δ …….Refraction angle of a prism……..… º

α …….Apex angle of a prism…….…… º

δL ……...Distance increment in the measuring arm of interferometer…….…. mm

λ …….Laser wavelength…….……... nm

N ……Number of fringes…….…….. –

θ_{offset}…Offset introduced in the incidence angle of the mathematical model……. º

t_{offset}….Offset introduced in the sample thickness of the mathematical model…. mm

d_{offset}…Offset introduced in the lateral displacement of the mathematical model.. mm

G…….(Statistics) Measurand……..... –

f…….(Statistics) Functional relationship……..... –

g…….(Statistics) Measure estimate……..... –

v_i……(Statistics) Estimate input value……..... –

u_{v_i}……..(Statistics) Standard uncertainty……..... –

k…….(Statistics) Coverage level……..... –

$s(\bar{v}_i)$…...(Statistics) Experimental standard deviation of the mean……..... –

$s(v_i)$…...(Statistics) Experimental standard deviation……..... –

j….....(Statistics) Number of observations……..... –

a….....(Statistics) Half-width of the input interval……..... –

U….....(Statistics) Expanded uncertainty……..... –

$u_c(g)$….(Statistics) Combined standard uncertainty……..... –

$u_c^2(g)$….(Statistics) Combined variance……..... –

c_i….(Statistics) Sensitivity coefficients……..... –

L….Distance between camera and laser……..... cm

$(x\,;y)$….2D sensor coordinates of the spot centre (with a sample)……..... pixel

$(x_0\,;y_0)$….2D sensor coordinates of the spot centre (without a sample)……. pixel

$(z_x\,;z_y)$….2D sensor coordinates of the spot centre in LabVIEW…….... pixel

$(x_{rel}\,;y_{rel})$….2D sensor coordinates of the spot centre relative to $(x_0\,;y_0)$…….... pixel

df….Difference between left/right average value of RI……... –

$\delta\theta$….Deviation factor for offset accuracy calculations……..... °

d_{pix}….Measured lateral displacement associated to θ_i……..... pixel

1. Motivation, Objectives and Approach

The measurement of the refractive index has many useful applications in various fields of expertise and it can provide invaluable knowledge about the properties of several materials of interest. The measurement of the refractive, particularly in the case of solid samples, has been around for many years. However with the continuous development of new types of materials and new possible applications, some techniques are no longer as viable or efficient.

Measuring the refractive index of solid samples can be very useful if, for example, the samples to be tested are custom made where a deviation from the reference value is more likely to occur. This slight difference can be critical in the efficiency performance of a glass optical component. It was noted that an apparent gap exists in the current situation regarding systems that perform this type of measurements, between simple systems with low measurement accuracy and complex systems with high accuracy. Existing techniques for determining the refractive index that produce results with a high accuracy, in the order of 10^{-5}, often resort to the construction of optical prisms with very tight manufacturing tolerances and are associated to very high manufacturing costs. In the case of optically simple, homogeneous and uncoated sample, such an accurate value of uncertainty in its Refractive Index (RI) is not necessary or possible due to a lack of specialised equipment in a common research laboratory.

The optics laboratory in the physics department of the Faculty of Sciences has demonstrated the need for such an intermediate system capable of filling the apparent technological gap between these two extremes. From this need and opportunity became the goal of the present master thesis, to create a system simple to implement, cost-effective and automated to allow a typical user to obtain the desired information on optically simple samples, titled "Optical metrology system for measuring refractive index of glass". The system can also have other useful, cost saving applications for the lab, such as the verification of witness sample or coatings properties and the determination of optical component properties (useful to determine a good replacement when information about the original is not available), for example.

Additional testing samples were provided by the VICARTE research centre (Vidro e Cerâmica para as Artes - https://vicarte.org/), that manifested an interest in knowing the refractive index of some LSC (Luminescent Solar Concentrators) glass samples with an uncertainty less than 1%. This request for a specific uncertainty also became a part of the main requirements for the developed system, a goal to achieve via optimization.

First, a study of the state of the art and some theoretical models were constructed, based on favourable techniques, in order to identify the main parameters associated to the determination of the refractive index of a glass plate. The theoretical models also provided insight on the acceptable interval for the uncertainty of each parameter in order to be possible to achieve an uncertainty in the measurements of the refractive index equal or below 1%.

The next step consisted on some practical individual testing of each relevant component of the optimized setup, to ensure that the system maintained an uncertainty below the acceptable limit, as projected by the theoretical models. Equipment response evaluations and calibrations were also performed to ensure that no undesirable side effects critically affected the measurements of the RI.

After acquiring a solid knowledge of the setup system, software was developed to automate measurements, capable of acquiring several measurements for a single sample and provide systematic statistically reliable results. To validate the system measurements, known samples were used and only after obtaining favourable results were the remaining unknown samples be measured.

This thesis proposes to address:

- A study of the different available techniques employed in the measurement of the refractive index of solid samples;
- A study of the different uncertainty components associated with the measuring of the refractive index and the construction of an uncertainty budget;
- The development and implementation of a simple system, capable of measuring the refractive index of optically simple glass plate samples;

This thesis does not intend to provide a deep theoretical study of all the available methods and techniques used to measure the refractive index, but instead aims to explore and develop the models of uncertainty to their maximum optimization, of the chosen technique.

The thesis is organized in 8 chapters:

- Chapter 1 – Presents the thesis motivation, the objectives and the approach.
- Chapter 2 – Introduces the concept of refractive index, and how it can be measured.
- Chapter 3 – Analyses in detail the two techniques adequate for implementation.
- Chapter 4 – Details the uncertainty budget and every component contribution.
- Chapter 5 – Details the design and implementation of the GOLD system.
- Chapter 6 – Presents GOLD tests and results with calibrated samples.
- Chapter 7 – Presents GOLD tests and results with unknown samples.
- Chapter 8 – Summarizes the results, presents conclusions and gives recommendations for future work.

2. Introduction

The goal of the present thesis is the development of a system capable of measuring the refractive index of glass samples – a subject well explored and already mature, with many methods and techniques applicable not just to solid, but for liquid or even gaseous samples [1]. The interest of this work therefore focuses in the optimization/refinement and improvement of a known concept, refining it for everyday use in a lab environment.

In the next subsections, a general overview on the refractive index of solid samples is given, along with an insight of the main methods used to measure it, and their applicability to the objectives of this thesis.

2.1 Glass and its refractive index

When it becomes necessary to understand the behaviour of a specific type of glass, two of the most important characteristics to know are its refractive index and its dispersion behaviour. The latter property ascertains the change in value of the refractive index related to the wavelength of the light through the Abbe number [2]. In the present work however, only one wavelength will be used (a HeNe laser with a beam wavelength of 632.8 nm) and so, the only property that can, consequently, be measured is the refractive index of glass samples.

The determination of the refractive index depends on simple concepts of optics [3] and there are several methods of optical measurement of the RI of solids based on the reflection or transmission of light from a surface, among them the deviation created by refraction, interferometry, reflectometry and ellipsometry [4]. Depending on the nature of the sample and the available means to conduct the required experiments, different techniques are employed, and always associated to each result is an uncertainty. Measured results are always a product of an experiment, therefore not absolute and so an uncertainty of measure associated to the measurement itself (when properly determined) helps ascertain the validity of the technique, as well as the results obtained by it.

Refractometry uses the refraction of waves on surfaces and interfaces to detect or characterize objects. There are many different forms of reflectometry that can be classified according to: the radiation used, the wave propagation geometry, the length scales involved, the measurement method and the application domain. Although refractometers are best known for measuring liquids, they are also used to measure gases and solids such as glass and gemstones.

Interferometry is a family of techniques in which electromagnetic waves overlap, causing interference that can be exploited to determine the differences between the interfering waves. In most amplitude-division interferometers, light from a single source is divided into two beams spanning different optical pathways, again being combined to produce an interference pattern. The resulting interference fringes provide information on the difference between the optical paths of the two arms of the interferometer.

Finally, ellipsometry is a family of techniques that measure physical properties of thin optical sample surfaces, by inducing a change in polarization state of an incident wave. The incident radiation (in a known state) interacts with the material structure of sample (reflected, absorbed, dispersed or transmitted) and the polarization change is compared. Considering that general optical samples have a thickness in the millimetres range and that some contamination of the surface can occur, since the goal was the determination of the sample refractive index (not just at the surface level), this family of techniques could not be used.

Figure 2.1 summarizes the three main techniques considered to measure the RI of glass samples.

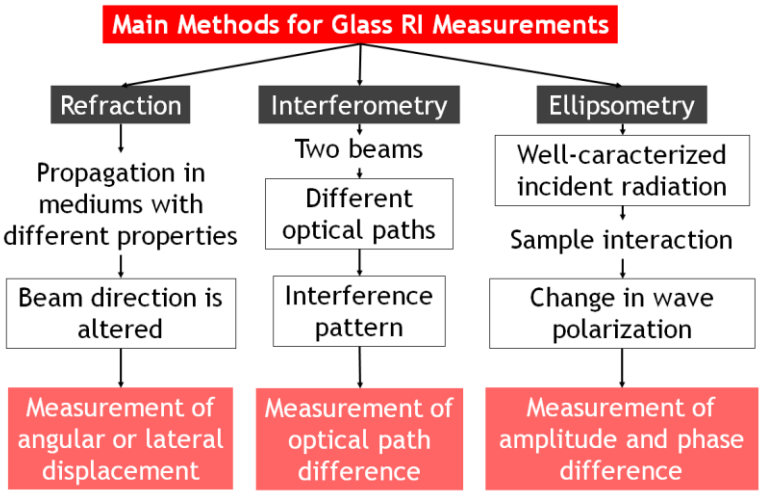

Figure 2.1 – Main techniques and the basic principles used in each to determine the refractive index of samples.

2.2 Refractive index measurement techniques

Currently, there are several methods and configurations available that allow the measurement of the refractive index of glass blocks, which can generally be measured through the deviation created by refraction, interferometric methods or ellipsometry methods – this last category was considered not adequate for this work. Depending on several factors – type of sample, available equipment, desirable results, and so on – the implemented techniques will drastically differ. It becomes therefore pertinent to conduct an analysis on the working principles of the general methods for the sake of determining the method that can be better adapted to fulfil the main objectives set by this work – a simple to implement, cost-effective and automated system capable of obtaining the refractive index of optically simple samples.

2.2.1 Refraction

When light enters a non-absorbing homogeneous material reflection and refraction occurs at the boundary surface. The refractive index n is given by the ratio of the velocity of light in vacuum c to that of the medium v. It is a measurement of the deflection occurring at the boundary surface due to the refraction of the light beam, which can be measured through Snell's law [3].

$$n_1 \sin\theta_1 = n_2 \sin\theta_2 \tag{2.1}$$

Through simple optical concepts it is possible to relate an incident light beam that crosses a transparent solid sample to the exiting beam. Two main methods can be used – the lateral displacement method and the prism method. Typically, the incidence angle is known, as well as the wavelength of the beam – as the beam enters a new medium, its direction, relative to the normal surface, is deflected according to Snell's law. In the case of a solid sample – a prism or a parallel plate – the beam's direction is deflected by a certain degree two times (one when entering the new medium, and the second when it exits into the original propagation medium). To determine the refractive index of the material, usually

the exit angle and/or beam displacement are recorded and through notions of geometry and algebra the refractive index of the material can be known.

Lateral Displacement Method

When a beam passes through a glass plate with flat surfaces parallel to each other, as illustrated in Figure 2.2, such as a window, the ray emerges parallel to its original direction, but laterally displaced by a certain distance *d*, which increases with the angle of incidence θ_i [5].

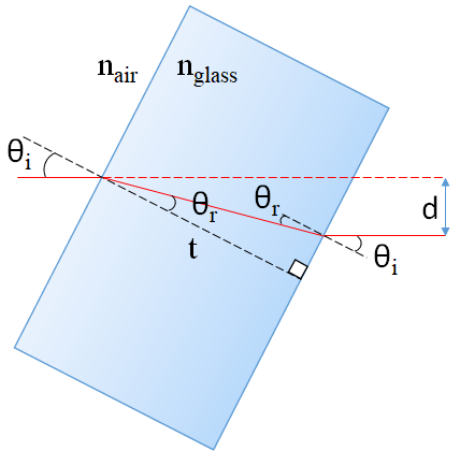

Figure 2.2 – Simple schematic drawing of the lateral displacement d *suffered by the beam (with incident angle θ_i) when it passes through a glass plate of thickness* t.

Knowing the values of thickness, incidence angle and the refractive index of air, n_{air}, and measuring the value of lateral deviation *d*, the RI of the glass, n_{glass}, is determined resorting to simple geometry rules.

The uncertainty that can be obtained using this technique has a wide variation in the order of magnitude, from 10^{-2} to 10^{-4}, accountable by the various configurations that are possible to use ([1], [5] and [6]).

Prism Method

In the prism method, a beam is directed to a face of a prism with an angle of incidence θ_i. The ray is refracted on the input face and deviated from the original direction by an angle δ, related to the apex angle, α, of the prism itself [4], as depicted in Figure 2.3.

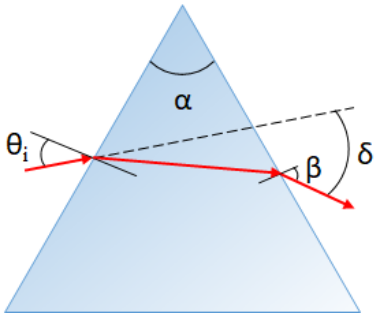

Figure 2.3 – Beam deflection, δ, by a prism with an apex angle α, with an incident angle θ_i *and output angle β.*

The accuracy of these refractive index measurements reaches values in the order of 10^{-5}, using goniometers with angle readings from 2° to 5°. Accuracy can be increased to 10^{-6}, although this requires special goniometers with angle readings on the order of 0.1°, with additional care to control environmental conditions (temperature, pressure and relative humidity) and imposing additional requirements on size and quality of the sample. It should be noted that the manufacturing tolerances of prisms are very small and result in highly accurate optical materials [7], built by companies such as SHOTT (one of the market leaders in the manufacture of optical glass), specifically for optical applications.

2.2.2 Interferometry

Many techniques of this family resort to the working principle of a Michelson interferometer [3] in order to measure the refractive index of a sample. This simple interferometer is composed by five main blocks: the light source, the beam splitter, the reference arm, the measurement arm and the sensor. In the specific case of solid samples, a Michelson interferometer can be employed to measure the difference in optical path length created by adding a glass plate to one of the arms as depicted in Figure 2.4. The primary wave (emitted from the light source) is divided into two secondary waves that maintain the same structure and properties. Secondary waves propagate through distinct trajectories (reference and measurement arms respectively) and are then recombined, creating an interference pattern that can be captured by a sensor.

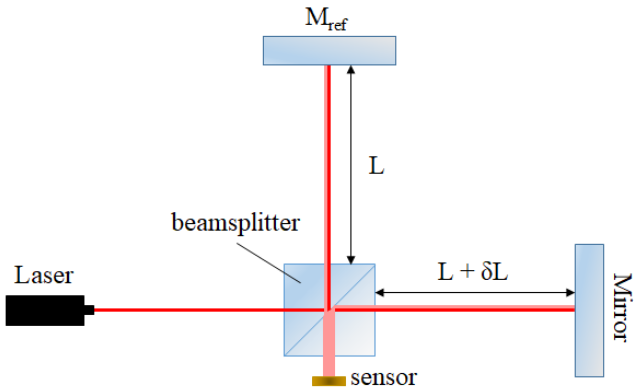

Figure 2.4 – Working principle of a Michelson interferometer. An interference pattern is created based on the splitted beam optical path difference by introducing an additional distance of δL to one of the interferometers' arms.

A more detailed description of the working principle can be found in Section 3.2 – for now, it suffices to say that this optical path difference (OPD), between the reference and measurement arms, is directly related to the number of fringes, *N*, picked up by the sensor by Equation (2.2), and then the RI can be determined [8].

$$OPD = \frac{N\lambda}{2} \tag{2.2}$$

From the interference pattern, the RI can be determined with an accuracy greater than 10^{-3}, if the thickness of the sample is known [4]. Determining the RI and the sample thickness across two sets of correlated fringes can increase accuracy up to 10^{-4} [9], but in doing so, restrictions will be imposed on either the sample or the procedure / equipment , which can make the technique much more complex.

2.2.3 Comparison of available techniques

Existing techniques for determining the refractive index produce results with an uncertainty that is typically in the interval from 10^{-2} to 10^{-5} [1]. Results with reduced uncertainty, in the order of 10^{-5} or below, usually involve the use of high precision equipment and/or samples. It became therefore necessary to conduct a preliminary research on existing techniques to determine which methods/configurations could be adapted to the proposed challenge – a simple, easy to use, cost effective and reliable setup capable of measuring the refractive index of glass samples.

The analysis of several existing techniques was conducted (Table 2-1) and some key comparisons were distinguished: the method and technique used, the uncertainty obtained in RI measurement, the complexity of the method (qualitative scale) and the possibility of optimization – that is, the possibility of altering and optimizing an already existing technique in order to fulfil this thesis objectives.

Table 2-1 – Summary of some of the researched methods and techniques relevant to the determination of the refractive index of a glass plate. Each technique is categorized according to: the method used, the obtained uncertainty in the refractive index n, its (qualitative) degree of overall complexity and its possibility of optimization.

Method	Uncertainty in n	Complexity	Possibility of Optimization	Reference
Lateral Displacement	10^{-2} to 10^{-3}	Low – High	Yes	[5]
Interferometry				
(simple)	10^{-2} to 10^{-3}	Low – Medium	Yes	[8], [10]
(with piezoelectric modulation)	10^{-3}	High	No	[9]
(with wavelength modulation)	10^{-4}	High	No	[11]
Prism	10^{-3} to 10^{-5}	High	No	[6], [12]

First, it is worth mentioning that all the techniques presented satisfy the requirement to obtain an uncertainty for the RI value smaller than 10^{-2} (or 1%), but some caution was exercised since the use of the terms “error” and “uncertainty” are sometimes confused. Additionally, some are not the most appropriate to implement, as is the case with techniques using the prism method ([6], [12]), which despite the high accuracy of the obtained results, resort to techniques that are considered too complex to implement. Due to their high degree of complexity, techniques [9] and [11], respectively, are not good

candidates for the objectives set for this thesis. The piezoelectric modulating interferometer uses an object or lens scanning method that provides two measured quantities: a movement distance of the stage between two light focusing states on the front and rear planes of an object and the corresponding optical path difference. The wavelength modulated interferometer method finely tunes a distributed-feedback diode laser light source to introduce a phase shift into the detected signal, while making the sample rotate to produce variable lateral shearing.

For the remaining techniques, [5] Lateral Displacement, [8] and [10] that resort to an interferometer, the uncertainty associated with the measurements lies in the range of 10^{-2} to 10^{-3} – however, the uncertainty indication in the majority of the articles is not concise and in some cases may have been incorrectly defined, so it is considered prudent not to place total confidence in the values obtained for uncertainty – considering them more as guidelines and not certainties.

Comparing the two techniques of interferometry ([8] (Deepak N.Iyer, 2006) and [10] (J.J. Fendley, 1982)), both use a Michelson interferometer, assuming however the knowledge in advance of some property of the plate that is used - either the material or its thickness. Two major differences between the two methods lie in reading the angle of incidence and observing the interference pattern: done manually by Fendley (with an uncertainty at the angle of ± 0.25 ° and manual counting of the number of fringes of the pattern of interference), and automatically by Deepak (with an uncertainty of ± 0,001 ° in the measured angle and the automatic acquisition of the interference pattern through a detector/oscilloscope). However, the uncertainty obtained for the RI is greater in the latter, perhaps associated to the degree of complexity of the whole process, which translates into an increase of sources of uncertainty that, if not properly minimized, limit the uncertainty of the results obtained.

Another possibility, as mentioned, of measuring the RI is through the lateral displacement method implemented by the technique described in [5] (V. Kolchinskiy et al., 2017). The uncertainty associated with the RI in this article is in the order of magnitude of 10^{-3} and the technique described presents an interesting possibility of measuring the RI of the sample through the capture of the beam by a 2D sensor (camera), having the disadvantage that it is necessary to know the thickness and geometry of the plate in study. The following figure illustrates, in a somewhat qualitative manner, the conclusions drawn from this preliminary research:

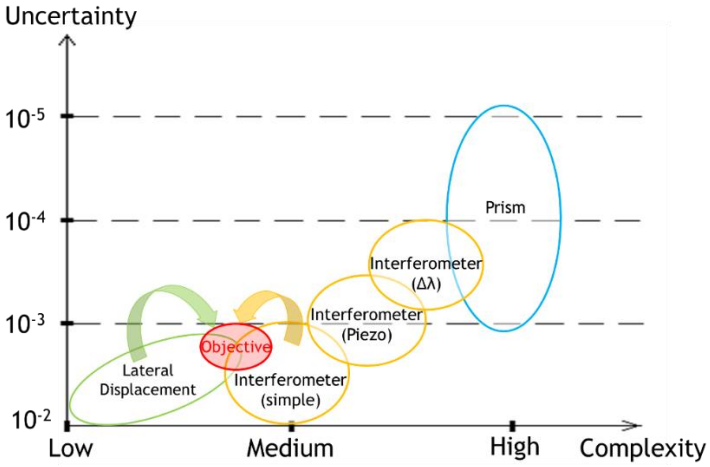

Figure 2.5 –Illustration of some techniques used to determine the refractive index of glass samples, in terms of their complexity and the associated uncertainties.

From this analysis it could be concluded that, even though many techniques for determining the refractive index exist, the current situation regarding systems that perform this type of measurements appears to be, understandably, that simple systems produce results with less accuracy. The objective of this thesis is to create a system:

- Simple to implement
- Cost-effective
- Automated
- Better than 10^{-2} accuracy in the results

Considering the above analysis, techniques that employ the lateral displacement method or interferometric methods seem to be the best suited options due to their adaptability to optimization through a detailed uncertainty model analysis. Additionally, the constant development of new types of sensors can have a critical beneficial impact in some parameter measurements, in terms of, for example, efficiency or resolution.

It is thus necessary to do a more thorough analysis, from the conceptual level to actual simulation of results in order to better understand the main advantages and disadvantages of each one.

3. Analysis of candidate techniques for refractive index measurement

It is known that interferometric methods have much better sensitivity to changes in the optical path when compared to simple lateral displacement methods however, since the system was designed to be automated, there were some concerns on the impact of vibrations, for example, of the rotating stage in the interferometric results. In order to produce reliable results, no matter the method used, it was concluded that several measurements made to a single sample would provide better results – by introducing the rotating stage in the sample it became possible to measure the RI of the sample according to the angle of incidence of the laser beam.

The following subsections analyse in greater detail the two possible methods employable in the determination of the refractive index of glass samples – a theoretical approach is made first, then both techniques are experimentally tested on a basic level, to better understand the interactions between components and how they can affect the results.

3.1 Lateral Displacement

A short description of the working principle of this method was given in section 2.2.1. In this case the variables are the incident angle (measured by the angular step rotating stage), the lateral displacement (known through the analysis of the images captured by the camera – through the processing of the collected images, it is possible to convert pixel coordinates into distance values), the thickness of the sample (mechanical measurement) and the refractive index of air, which throughout this work, was considered constant and equal to 1.00027 – for a wavelength in ambient air of 632.828 nm, with an air temperature of 20°C, an atmospheric pressure of 101.325 kPa and a relative air humidity of 50% – in accordance to the "*Engineering Metrology Toolbox*" provided by NIST [13].

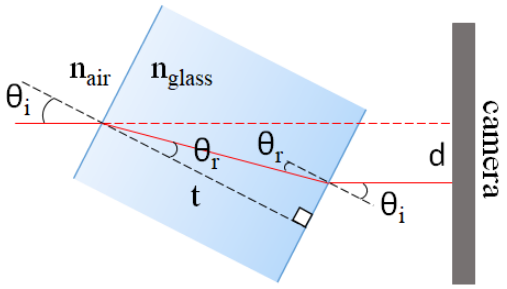

Figure 3.1 – Lateral displacement, d, in a 2D sensor (camera), of the beam with an incident angle θ_i, by a glass sample with a thickness t.

The refractive index of the glass sample, rearranging Equation (3.1, can be determined as follows:

$$d = t \sin\theta_i \left(1 - \frac{\cos\theta_i}{\sqrt{\left(\frac{n_{glass}}{n_{air}}\right)^2 - \sin^2\theta_i}} \right) \tag{3.1}$$

$$n_{glass} = \sqrt{\left(\frac{\cos\theta_i}{1 - \frac{d}{t\sin\theta_i}}\right)^2 + \sin^2\theta_i \,.\, n_{air}} \tag{3.2}$$

With Equation (3.2, it was possible to understand and visualise the output of ideal conditions if a sample was rotated. This study was especially important due to the fact a real setup will always have sources of error that deviate, in some degree, from the ideal results. If a detailed study on the ideal model is made, it helps to better determine the probable cause of deviation from the expected results during calibration and testing.

The first step was the visualization of the ideal results – first, the lateral displacement, *d*, captured by the camera and caused by the beam displacement on a 10mm thick glass plate, obtained with an incident angle that takes values in the range from -30° to 30°. According to Equation (3.1, the determination of the lateral displacement depends on the value of n_{glass} and vice-versa. It may seem that the results obtained by this method become a loophole, but in fact only in this ideal scenario is the lateral displacement computed in this manner (it is necessary to give an initial value to n_{glass} in order to calculate *d*, that is then used to calculate the end value of n_{glass}, according to Equation (3.2, since in the real setup it is independently obtained by the pictures captured by the camera.

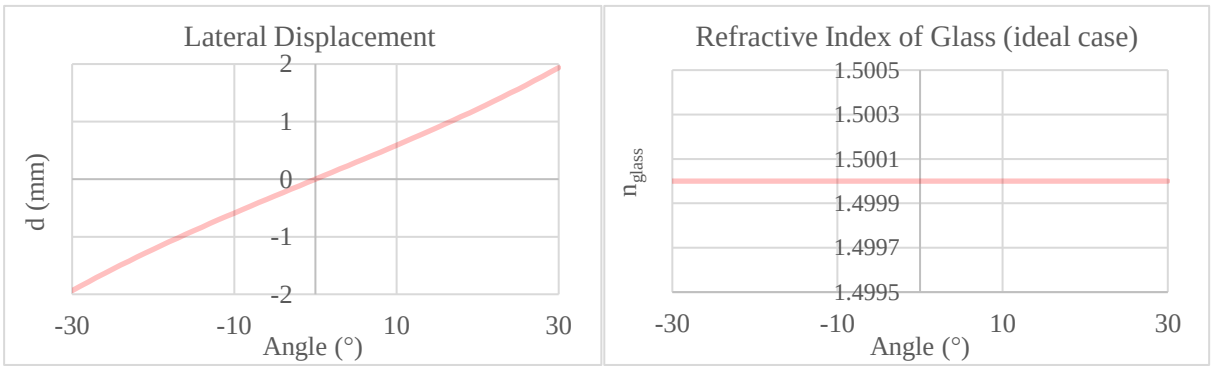

a) b)

Figure 3.2 – Simulation of the expected results of the lateral displacement of the beam (a) and associated refractive index of glass (b) in an ideal, error free, environment, considering a glass plate with 10mm thickness, $\theta_i = [-30; 30]°$ and an initial value for the RI of glass of 1.50.

As can be seen in Figure 3.2 (a), for an amplitude of $\pm 30°$, the maximum expected lateral displacement is $\pm 1.94\ mm$, as results for symmetrical angles are symmetrical in magnitude. It is also possible to conclude that the lateral displacement is almost linear, however an increase in the incident angle leads the trend slightly away from a linear behaviour. The values for the RI of glass, considering that this is the ideal case, are all equal to the initial guess, that is $n_{glass} = 1.50$, with no associated error as was expected. It is also important to note that, when $\theta_i = 0°$, the sample surface is perpendicular to the incident beam and there is no significant lateral displacement of the beam when it propagates in the air or inside the glass due to the small sample thickness.

Taking now into consideration the uncertainty associated with the variables, θ_i, *d* and *t*, graphs of both the lateral displacement and the refractive index of glass (Figure 3.3), still calculated with

Equation (3.2, were produced, comparing the ideal situation (pink line) described above with the results obtained if one of the variables had an associated error.

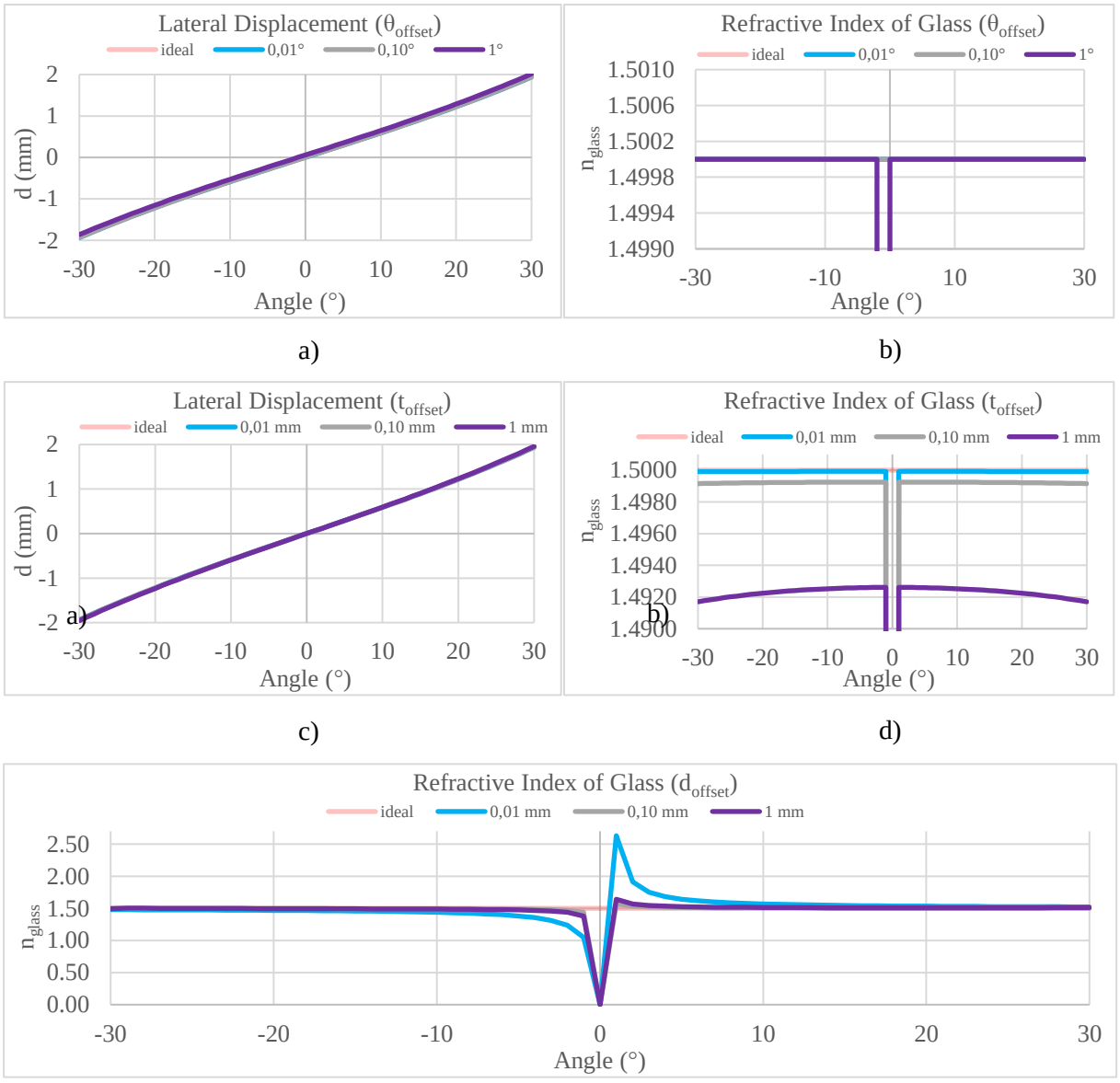

Figure 3.3 – Analysis of the impact of an offset in the three variables needed to know in order to determine the RI of glass. Top, introduction of an offset in the incident angle, θ_i. Middle, introduction of an offset in thickness of the sample, t. Bottom, introduction of an offset in the lateral displacement, d.

These were built by adding the offset to the variable when computing the ideal value, for example – if the incident angle was being analysed, an offset angle, θ_{offset}, was added making $\theta_i = \theta_i + \theta_{offset}$. The magnitude of each offset was determined according to the deviation that it produced in the results, namely, offsets that produced deviation in the order of 10^{-3}, 10^{-2} (required if the technique is to be employed) and a worst-case scenario of 10^{-1}. The objective of this study was to assess the individual influence of each variable in the outcome, as well as to better understand the degree of

uncertainty that needed to be associated with each variable in order to produce reliable results with an uncertainty below 10^{-2}.

Starting by the two top graphs in Figure 3.3 (a and b) that concern an offset in the incident angle of the beam, with respect to the normal of the glass sample surface, the effect of this offset in the lateral displacement is constant effect along the line as is a tilt in the results of the refractive index of glass, which however don't differ greatly from the ideal (around 0.1%) even with a 1% offset in the angle. A slight tilt at the extremities of each plot can be observed in the lateral displacement if the offset is introduced in the sample thickness (Figure 3.3, c and d), although it also does not appear to have any significant effect in the RI of glass (again, a difference of about 0.1%). Both an offset in the incident angle or thickness can cause a slight deviation from the ideal results but it is an offset in the measurement of the lateral displacement itself that can become quite disastrous as can be seen in Figure 3.3 (e). In fact, an offset of just 0.1% can cause an error of about 10% in the value of the RI of glass, making the lateral displacement the variable that most increases the uncertainty in results obtained by this method.

From this simple theoretical analysis, the effect of measurement error was studied, related to the three main uncertainty parameters and their influence in the value of the refractive index.

3.2 Michelson Interferometer

A Michelson interferometer (MI) is used to measure the difference in optical path length created by rotating the glass plate located in one of the arms. In the MI, the primary wave is divided into two secondary waves that have the same structure as the primary wave. Secondary waves propagate through distinct trajectories (usually referred to as reference arm and measuring arm) and subsequently are recombined to create an interference pattern.

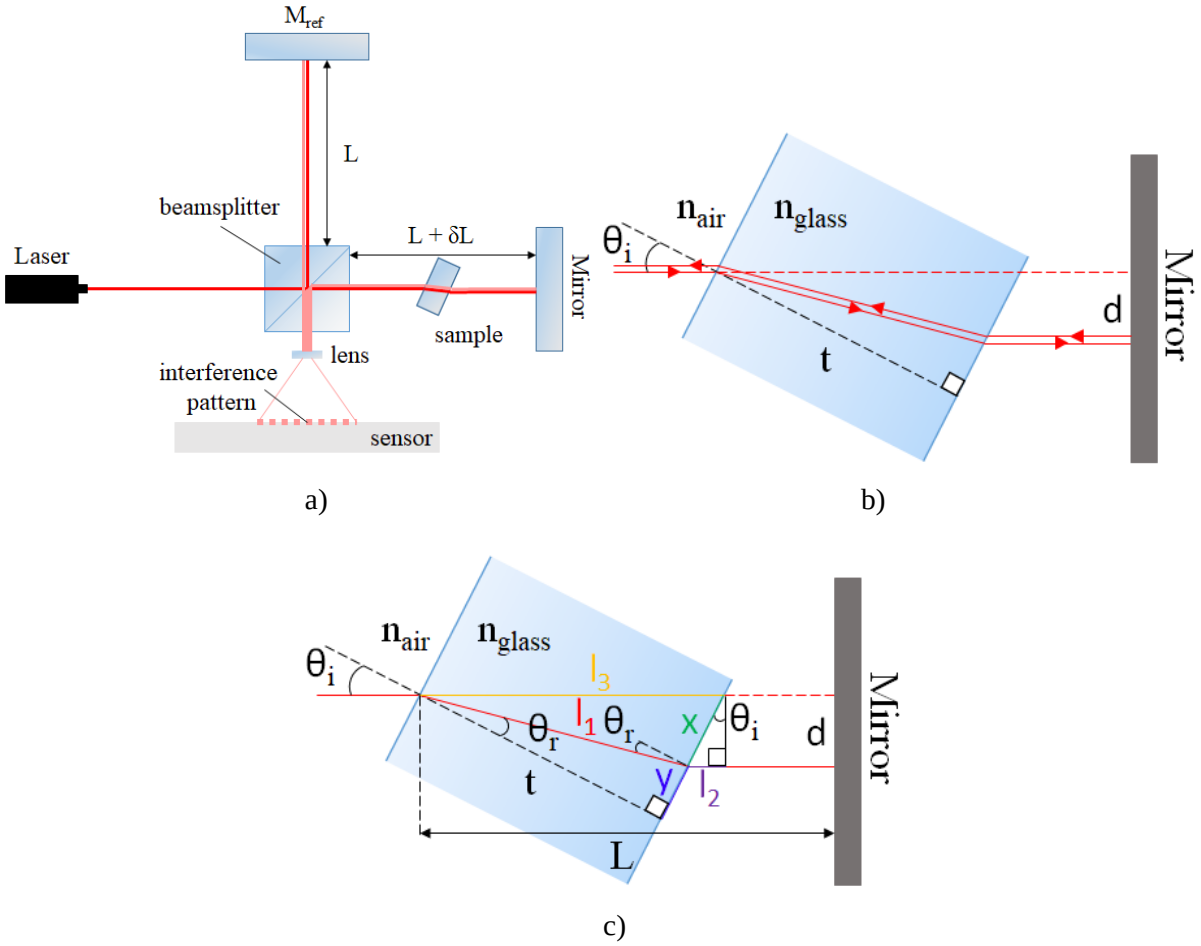

Figure 3.4 – Top: Schematic of a Michelson interferometer (a) and the OPD created by the glass sample (b). Bottom: Schematic of the beam path with an incident angle θ_i *in the glass sample (with refractive index* n_{glass}*) surface and chosen variables to associate the OPD with the RI.*

This pattern between the two linearly polarized and monochromatic waves has an intensity that depends on the optical path difference (OPD) introduced in the measuring arm (Figure 3.4) of the recombined beam which in turn can be measured by the number of fringes that are picked off by the detector, according to Equation (3.3.

$$I_{OPD(t)} = l_1 + l_2 + 2\sqrt{l_1 l_2}\cos\left(\frac{2\pi}{\lambda}OPD(t)\right) \tag{3.3}$$

Where l_1 and l_2 are the individual intensities of the two beams and λ the wavelength of the light emitted by the laser. According to Figure 2, the OPD is found by the path difference when $\theta_i = 0°$ and $\theta_i \neq 0°$. By measurement of the OPD, n_{glass} can be determined solving the following equation:

$$OPD = 2\left[\left(Ln_{air} - t(n_{air} - n_{glass})\right) - \left((L - l_3 + l_2)n_{air} + l_1 n_{glass}\right)\right] \quad (3.4)$$

Replacing l_1, l_2 and l_3 by their trigonometric relationships with the incident angle and with the refraction angle, θ_r (related to θ_i by Snell's Law), the following equation of the OPD, related to N fringes registered by the sensor (Equation (2.2)), that can be solved for n_{glass}:

$$OPD = 2t\left[\left(\frac{n_{glass}}{\cos\,\theta_r} + n_{air}\left[(\tan\theta_i - \tan\theta_r)\sin\theta_i + \frac{L}{t} - \frac{1}{\cos\,\theta_i}\right]\right) - \left(\frac{L}{t}n_{air} + (n_{glass} - n_{air})\right)\right] \quad (3.5)$$

$$n_{glass} = \left[\frac{OPD}{2t} - n_{air}\left[\sin\theta_i\,(\tan\theta_i - \tan\theta_r) - \frac{1}{\cos\theta_i} + 1\right]\right]\frac{\cos\theta_r}{1 - \cos\theta_r} \quad (3.6)$$

A similar analysis, as the one made in Section 3.1 regarding the output of ideal results, was also made to this interferometric method, with the same goals – that is, to assess the behaviour of the system in general, and the influence of an error in each variable. In this case, the refractive index of glass and the optical path difference are related, and so, just as it was done in the lateral displacement method, an initial value for the RI of glass was given. During measurement processes, a glass plate is placed in the measuring arm and continuously rotated, changing the optical path difference and thus producing a fringe pattern related to the angle of incidence and OPD.

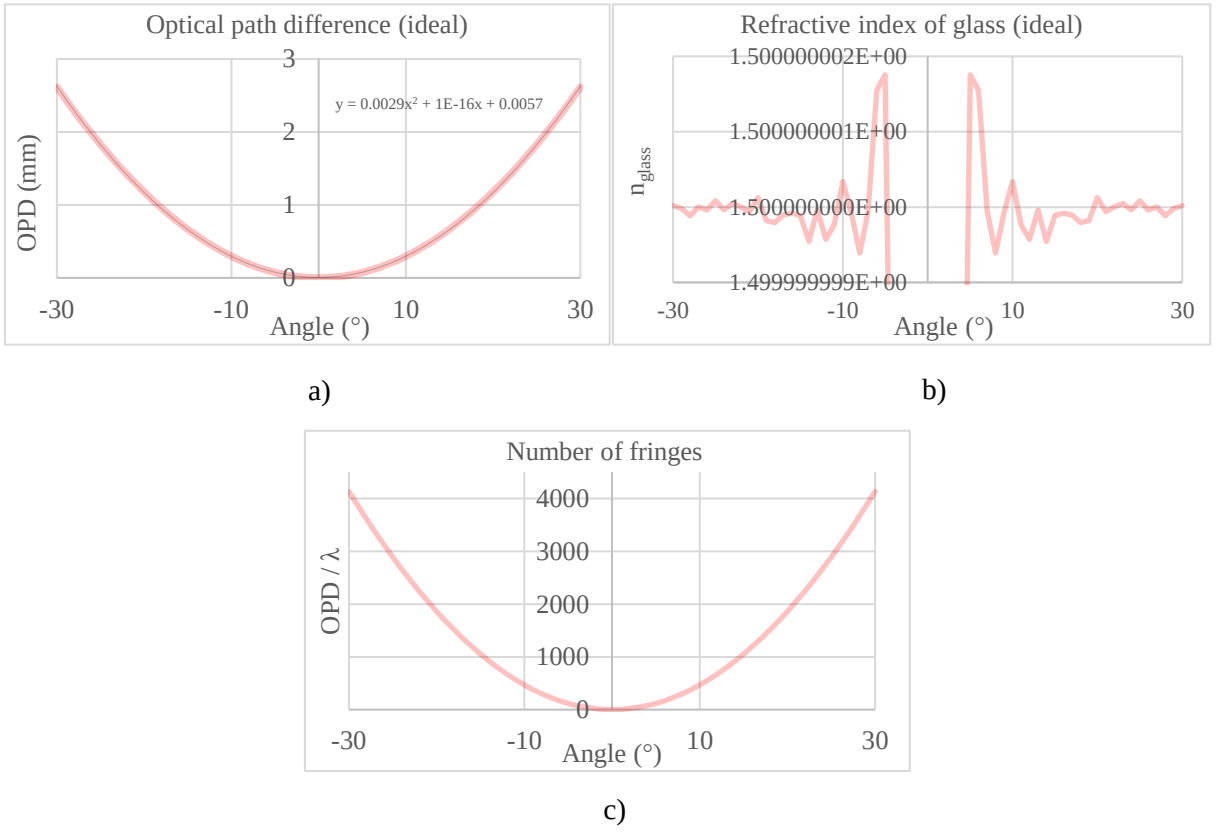

Figure 3.5 – Top: Simulation of the expected results of the OPD between the two arms of the interferometer (a) and associated refractive index of glass (b) in an ideal, error free, environment, considering a glass plate with 10 mm thickness, $\theta_i = [-30; 30]°$ with 1° steps, an initial value for the RI of glass of 1.50 and L *= 10 cm (distance between the first glass surface and the mirror)). Bottom: Number of fringes produced with respect to the angle of incidence in the glass sample.*

Looking at Figure 3.5 (a), for an amplitude of $\pm$ 30°, the maximum expected optical path difference was $\pm$ 2.62 mm, as results for symmetrical angles are symmetrical in magnitude. The OPD can clearly be interpreted as 2nd order polynomial with respect to the incident angle. A not so orderly representation is depicted in the results obtained in Figure 3.5 (b), with increasing oscillations as the incident angle approaches $\theta_i = 0°$. Indeed, when the beam is perfectly perpendicular to the glass surface, there is almost no path difference between the reference and measuring arms of the interferometer ($OPD = 0$), and so it becomes impossible to obtain a value for the refractive index. Despite the apparent instability, when comparing them with Figure 3.2 (b), results obtained by this method can provide values of the RI with an uncertainty, in theory, of around ~10^{-9} as opposed to the ~10^{-3} provided by the lateral displacement. In Figure 3.5, bottom, the number of fringes associated to an optical path deviation can be known by dividing the value of the OPD by the wavelength of the laser beam. Considering the number of fringes produced in a 60° amplitude (-30° to 30°) the interferometer sensitivity to small increments in the OPD is shown, being able to detect small differences up to the nanometre level (wavelength of the laser beam).

Before further comparisons can be made between the two methods, a similar analysis concerning the uncertainty associated with the variables, θ_i, t and OPD, and their effects on the optical path difference and the refractive index of glass was conducted. In Figure 3.6 the ideal situation (pink line) described above can be compared with the results obtained if one of the variables had an associated offset.

Evaluating the first two top graphs in Figure 3.6, that display the results with the addition of an offset in the incident angle, it is possible to discern a slight tilt in the values for the optical path difference. Indeed, an introduction of an offset of 0.01°, 0.1° and 1° produces results with deviations of approximately 0.07%, 0.7% and 7%, respectively. However, in this range of offsets, the error in the value of the RI of glass for this range of offsets was always below 0.001%. This indicates that an offset in the incident angle should have virtually no effect in the results and as such, should be considered negligible. Similar conclusions can be made about the introduction of an offset in the thickness of the sample (Figure 3.6, middle): offsets ranging from 0.001 mm to 0.1 mm in the value of t only produce an error in the RI of glass also always below 0.001%.

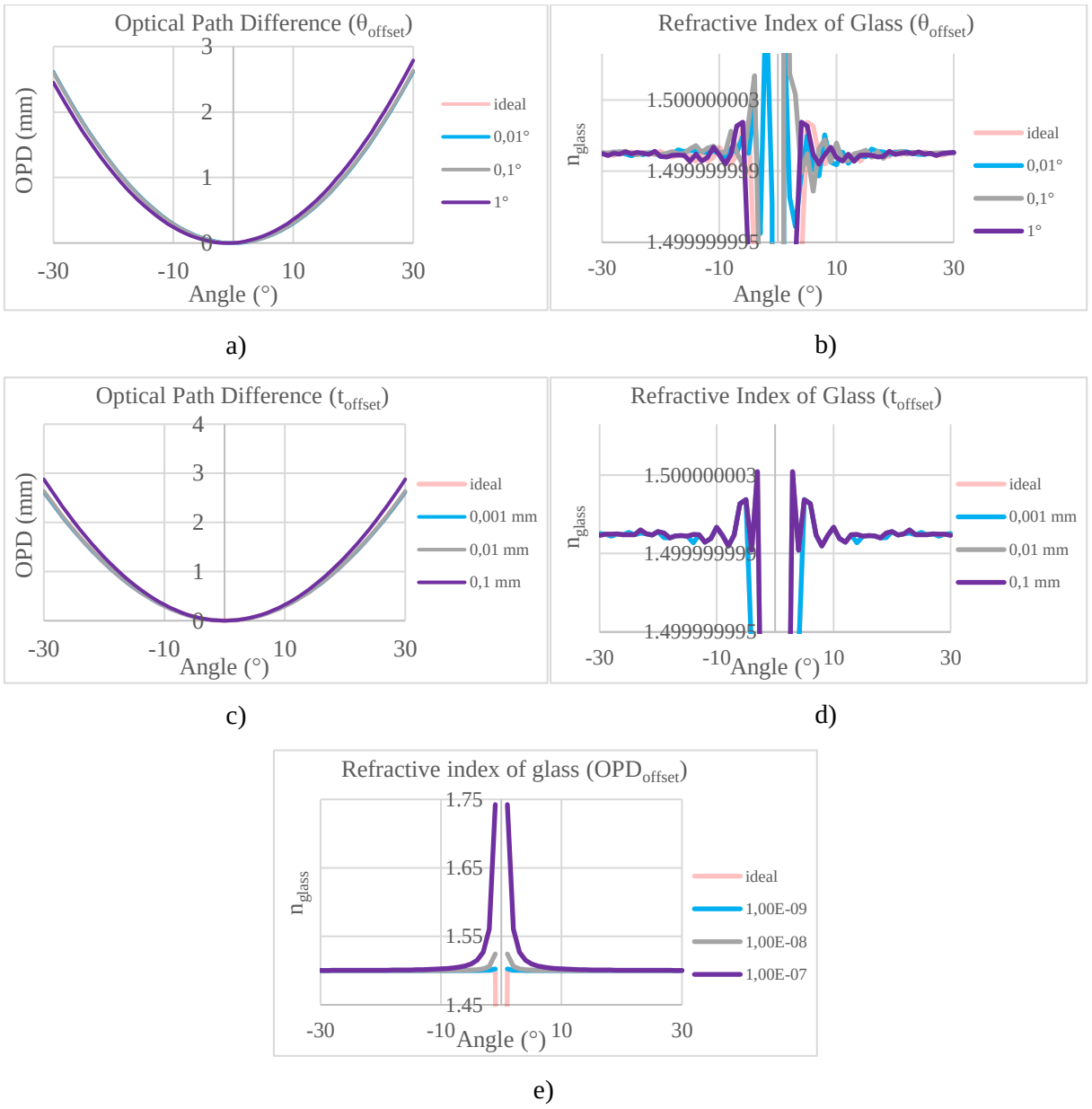

Figure 3.6 – Analysis of the impact of an offset in the three variables needed to know in order to determine the RI of glass. Top, introduction of an offset in the incident angle, θ_i. Middle, introduction of an offset in thickness of the sample, t. Bottom, introduction of an offset in the optical path difference, OPD.

Finally, regarding an offset in the optical path difference, Figure 3.6, (e), it is evident that it is this variable that gives the larger contribution to the uncertainty of the value for the refractive index of glass. A mere offset of 0.001 nm to 0.1 nm to the OPD produces deviations in the RI of about 0.01% and 1%, respectively, consequently a greater care in the correct readings for this variable should be taken into consideration if this method is employed.

3.3 Experimental Implementation

To test the effectiveness of two different approaches, that in theory could provide the required accuracy to determine the refractive index of a glass plate ($\leq 10^{-2}$), an experimental setup was drafted that could accommodate both methods in the same breadboard (Figure 3.7). The main goal was to have two independent subsystems that could be tested in similar conditions in their ability to produce reliable results, and to enable the experimental characterization of the different parameters involved.

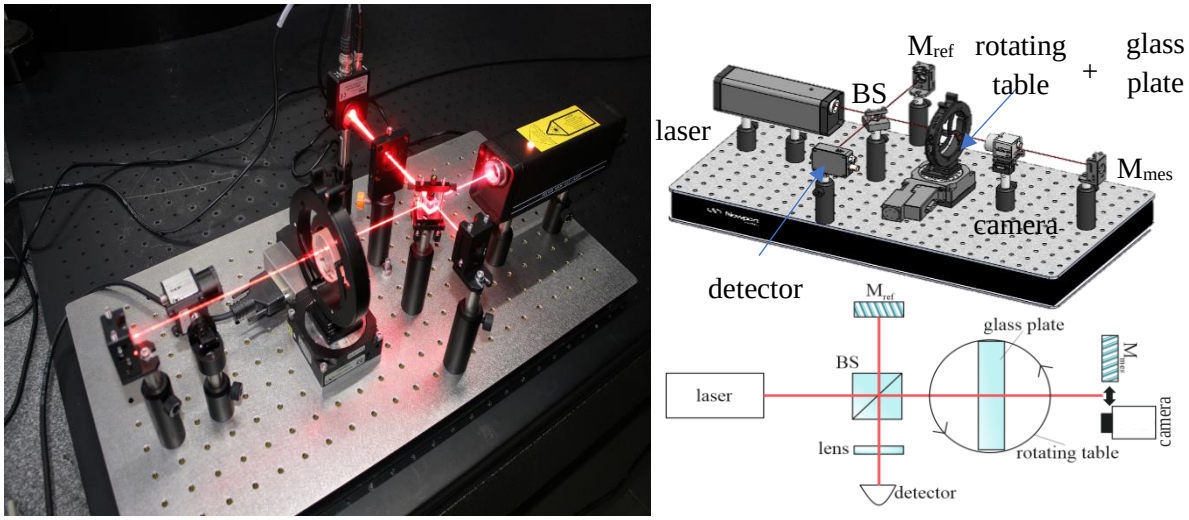

a) b)

Figure 3.7 – Experimental setup (a) of the system. It is composed by a laser, beam splitter, two mirrors, rotating stage and glass sample, a camera, a lens and a detector (b, bottom). The 2D sensor can be deviated from the beam path, adding or removing it from the setup as necessary (b, top).

A HeNe laser with a wavelength of 632.8 nm [14] was used along with a 2D sensor [15] or a Si detector [16], depending on the method, for the determination of the refractive index of glass samples – the sample was placed at the centre of an automated rotating stage [17]. Additionally, in the interferometric method, a beam splitter [18], two mirrors (one for each arm of the interferometer) and a lens were used. The purpose of the latter was simply to magnify the interference pattern in order to guarantee that a single fringe was detected. At this point, an uncharacterized silica glass plate was used with the sole purpose of simulating a glass sample. It proved useful because it allowed the study of its interactions with the system (described in more detail in the following subsections) in an earlier state which allowed the discovery of its major sources of error. Once those were well characterized, known glass samples could be used for calibration and testing purposes of the system.

Considering the fact that the chosen setup incorporates two independent sub setups, if the lateral displacement method is in analysis, the 2D sensor camera is used and placed as can be seen in Figure 3.7 (b), top – for the interferometry method, the camera is moved to the side (as shown in Figure 3.7, (a)). Before acquiring any type of data, the setup required some alignment adjustments that had to be made in steps, in order to ensure an overall good alignment, starting by the alignment of the beam that exits the laser with the beam splitter cube.

A neutral filter had to be applied before the camera aperture to prevent excessive saturation of the camera because of the intensity of the laser beam – if it was not applied, the laser spot became much harder to track, especially in small shifts due to over-saturation.

3.3.1 Lateral Displacement

Despite all the careful alignments made, that ultimately contribute to better value readings, internal reflections in the components still occurred. This interferometric pattern, created mainly due to the modulation of the beam after passing through the beam splitter and the protective glass in the camera (and due to reflective interference), had a negative impact in the accuracy. As seen in Figure 3.8 the captured spot displays a fringe pattern that can cause a non-negligible effect in the determination of the coordinates of the centre of the spot.

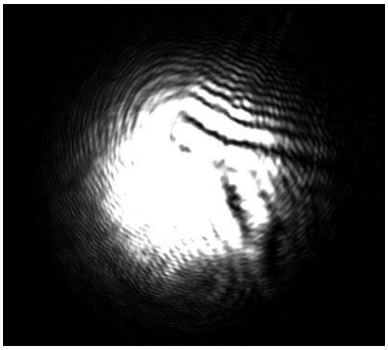

Figure 3.8 – Left: Spot image captured by the 2D CMOS sensor with the setup as shown in Figure 3.7. Interference can be seen due, mainly, to internal reflections in components along the beam path.

To determine the refractive index of the glass sample, this setup needs to capture the laser beam spot that crosses the sample and then determine the displacement that occurred by finding the geometrical difference between the spot centre when the sample is perpendicular and when it is rotated. Considering these preliminary inspections of the interactions between the subsystem components it was foreseeable that great care in the alignments would have to be taken into account to minimize the interference patterns in the captured spot. Nevertheless, interference had a particularly negative impact when the beam was perpendicular to the sample (that is $\theta_i \approx 0°$) – reflections from other components or other reflections within the sample had a bigger impact in small angle measurements of the spot in the 2D sensor.

Considering the analysis made in the previous section, it was observed that the measurement of the lateral displacement was the most influential in the results for the RI of glass. It also became apparent that results with higher accuracy were associated to measurements for greater incident angles and so, if this technique were to be implemented, further studies of the reliability of the captured images, as well as the relationship between incident angle and measurement accuracy, were required.

3.3.2 Michelson Interferometer

The setup of an interferometer requires the correct alignment between all its components in order to ensure good results. Specifically, it is vital that the alignments of the laser beam between the mirrors and the beam splitter are as optimized as possible, in order to decrease unwanted reflections (that could not be mitigated) and increase the interference pattern quality captured by the sensor. Both mirrors could be manipulated to allow small adjustments to their axis, which was critical in the alignment of the reference and measure beams.

However, as was the case in the camera setup, the glass sample produces internal reflections that combined with the reflections produced by the interferometer components originated parasitic reflections that had a negative impact in the signal captured by the sensor (noise). To reduce this type of contributions, more pronounced when the sample is perpendicular to the beam ($\theta_i \approx 0°$), the interferometer components were slightly misaligned on purpose, so that most of the unwanted reflections were not captured by the sensor, as can be seen in Figure 3.9 (a), $\theta_i \neq 0°$, and (b), $\theta_i \approx 0°$, – the sensor (green circle) was partially covered with paper to make it easier to see parasitic interference patterns (yellow circle).

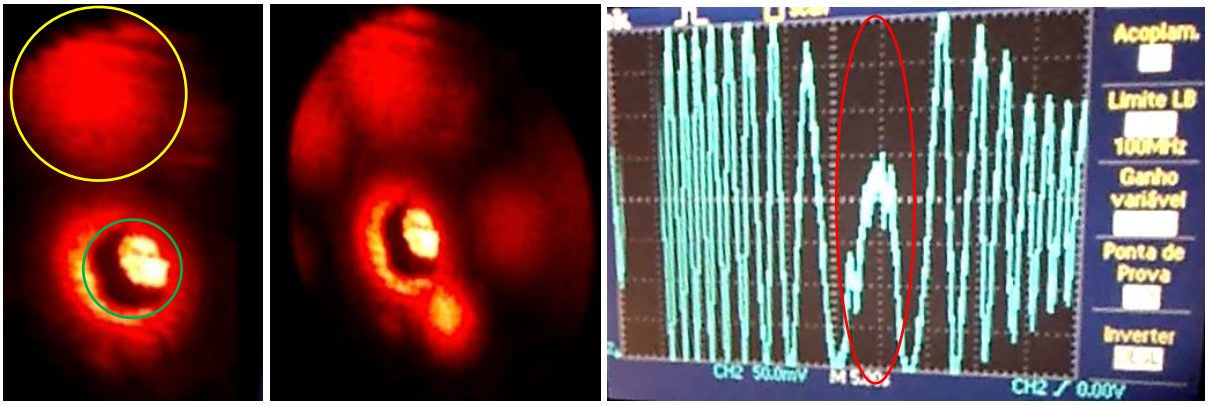

a) b) c)

Figure 3.9 – Captured signal when the sample is rotated from $\theta_i = -\alpha$ to $\theta_i = \alpha$, with $\alpha \lesssim 5°$(a, $\theta_i \neq 0°$, b, $\theta_i \approx 0°$) – on the right (c) is the registered signal in the oscilloscope for this rotation.

Through the analysis of the captured signal in the oscilloscope (c), it is interesting to note the symmetry of the signal with respect to the perpendicular position (roughly marked by the red circle). Indeed, as was foreseen by the equations and the analytical study, when θ_i nears 0° it becomes increasingly difficult to detect an OPD between the reference and measure arms, and so the fringe pattern is affected. Since unwanted interference can be reduced, but not entirely mitigated, this could critically affect the performance of the technique which resorts to measurements of fringes relative to the perpendicular position to measure the optical path variation that occurs when the sample is rotated – if that information is lost due to noise contributions, the measurements cannot be used to determine the value of the sample's RI.

Another interesting effect, that also had a negative impact in the readings, was the interference created by small vibrations (Figure 3.10). Although the setup was placed in a breadboard, if strong enough vibrations affected the setup, these were picked up by the sensor, since the table was not stabilized – even something as insignificant as walking around the table or lightly pressing/tapping the table with a hand. This can easily be corrected by using a stabilized optical table – however, this increases the complexity of the system, which goes against one of the main objectives set by this thesis.

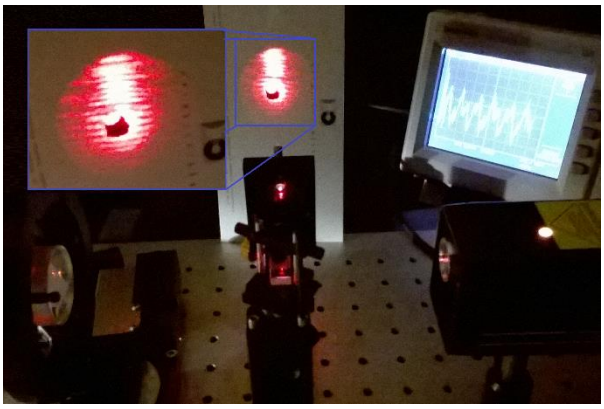

Figure 3.10 – Signal captured when light taps are made on the breadboard.

In theory, the interferometer provides much better results when compared to the lateral displacement technique, but considering its sensitivity, if this technique is to be employed, it is necessary to better understand how the uncertainty can be affected, and how is its general performance when compared to the lateral displacement technique in order to assess the viability of both.

3.4 Trade-off analysis

In sections 3.1 and 3.2 mathematical models of both techniques were developed in order to better understand the contribution of each parameter (incident angle, θ_i, thickness of the plate, t, and lateral displacement, d or optical path difference, OPD) to the determination of n_{glass}. Estimates of obtained results when each variable had an associated offset, from 0.01% to 1%, that deviated the results from the ideal situation where constructed in order to analyse their impact in the measurements of the RI, specifically in the uncertainty of n_{glass} (the objective, below 10^{-2} (green line), and a goal, 10^{-3} (orange line)). In this section, and considering that the components that are used in the setup have fixed uncertainties, *u.*, (according to the instrument, and guaranteed by the manufacturers), the analysis of the permitted uncertainty for each variable was evaluated in a more direct approach. Figure 3.11 and Figure 3.12 show the theoretical requirements (blue line) in the uncertainty of each individual parameter to obtain the desired overall uncertainty in the RI of glass. The relation uncertainty in parameter / uncertainty in n_{glass} is linear in all cases.

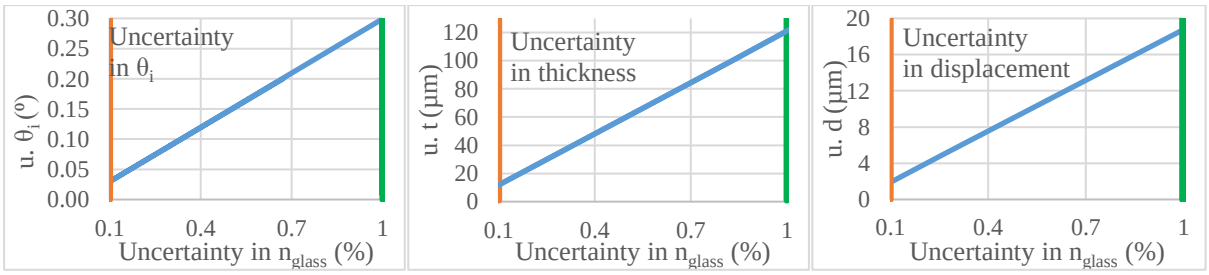

a) b) c)

Figure 3.11 – Evaluation of the uncertainty (u.), with the lateral displacement technique, of the measurements of θ_i, t *and* d, *respectively, required to keep the uncertainty of* n_{glass} *equal or below 1%.*

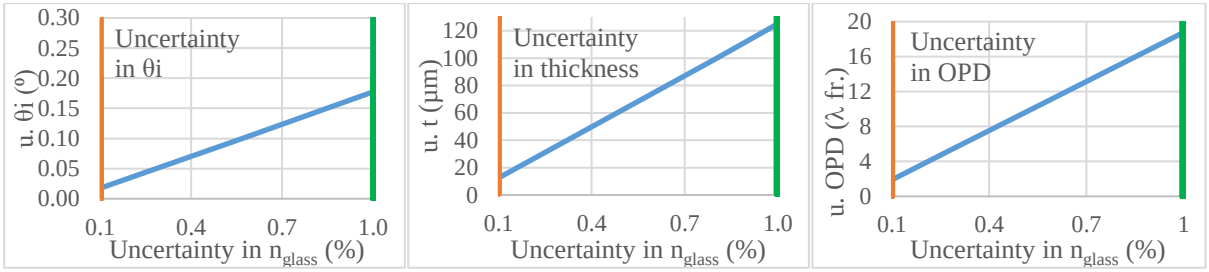

a) b) c)

Figure 3.12 – Evaluation of the uncertainty (u.), with the interferometer technique, of the measurements of θ_i, t *and* OPD, *respectively, required to keep the uncertainty of* n_{glass} *equal or below 1%.*

The incident angle and plate thickness uncertainties are common to both techniques and very similar in values, for uncertainties below 1% and 0.1% – all theoretical values are greater or equal to the ones imposed by the components, therefore the contributions for the uncertainty of the RI of glass, by these two variables, are always within acceptable values.

In the case of the lateral displacement, it consists of a very simple and straightforward setup capable of providing absolute measurements – even if interference renders the measurements closer to the perpendicular position invalid, greater angle measurements are still valid and independent. Several types of light sources can be used (and aren't required to be coherent) – although a study should be made before using any light source to validate the results obtained with it. The greatest disadvantage of this method resides in the resolution of the camera pixel. Refractive index results with an associated uncertainty of 1% require that the uncertainty associated to the measurements of d about $\pm$ 19 μm (or about 3 pixels), and of $\pm$ 2 μm for an uncertainty of 0.1%, which is less than half a pixel and close to a technological limit.

Although the interferometry technique is in theory better (it is possible to distinguish path differences up to an half fringe ($\lambda/2 \approx 316$ nm or 0.316 μm), due to its higher sensitivity some critical aspects should be taken into account. The setup is comparatively more complex, the zero position (no deviation) is harder to establish (relative measurement) and interference noise (due to reflection interference) can affect the fringe measurements especially around the glass perpendicular position to the beam. Due to the relative nature of the measurements, if the symmetric positions around the perpendicular position are not correctly measured, the "zero position" is lost and further measurements become invalid.

Experimental observations confirmed that the greatest problem in measurements, the noise introduced by the multiple reflections, can be safely ignored in the lateral displacement method (as it is an absolute measurement) but may have a critical negative impact in measurements made with the interferometric method (due to its relative nature). For the reasons just described, and summarized in Table 3-1, the method chosen to implement the measurements of the refractive index of glass plates was the lateral displacement.

Table 3-1 – Summary of the main advantages and disadvantages of each technique – Lateral Displacement and Interferometry.

	Lateral Displacement	Interferometry
Advantages	• **Absolute measurements (low impact of internal reflections)** • Insensitive to vibrations • Lower complexity • Can be used with different light sources	• Higher sensitivity • Higher accuracy
Disadvantages	• Limited resolution	• **Relative measurements (high impact of internal reflections)** • Higher complexity • Interference due to reflections • Requires coherent light source

4. Refractive Index of Glass by Optimized Lateral Displacement

The measurement of the refractive index of glass samples relies on the measurement of the optical path difference when the sample is deviated from a perpendicular position, with respect to the incident beam. Depending on this deviation, an incident angle value is associated to a specific optical path within the glass, which in turn is associated to a lateral displacement (or shift or deviation) that can be tracked using a CMOS camera Figure 4.1 (right).

It is therefore intuitive to devise a system that can keep track of the main parameters (Equation (3.2 – the incident angle θ_i, the sample thickness *t*, the lateral displacement *d* and the refractive index of air n_{air}. As stated before, for all experiment purposes, the latter variable, the RI of air, was considered constant, needing no further analysis on its impact in the results of RI measurements. From the setup designed and described in Section 3,*"Analysis of candidate techniques for refractive index measurement"*, only three main components were used in this setup – the laser source, the rotation stage and the camera. The new system setup can be seen in Figure 4.1 – for convenience, it can be abbreviated and referred as GOLD (Glass Optimized Lateral Displacement) system.

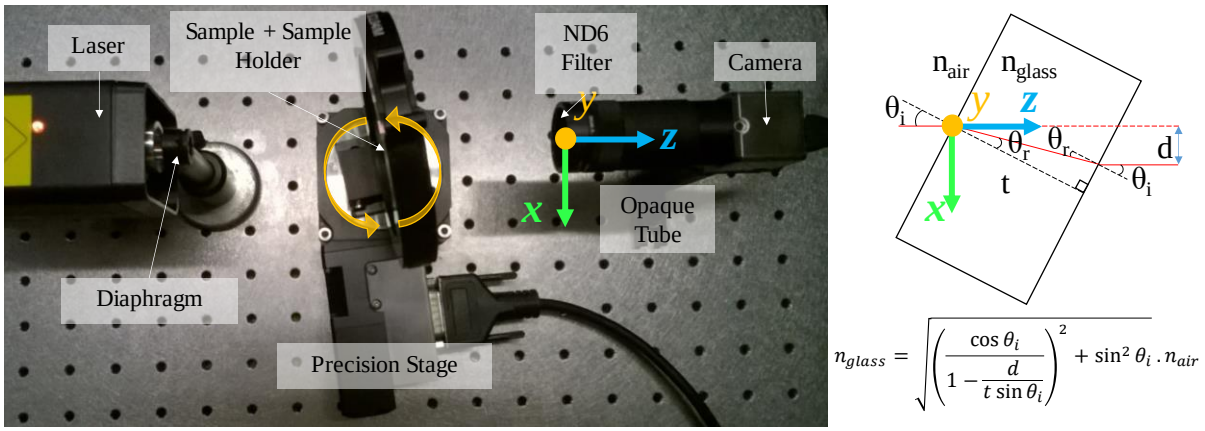

Figure 4.1 – Optimized Lateral Displacement system setup (left) and operating principle (right).

In general, building a system begins with the hardware, the system is assembled and only then is the uncertainty budget constructed, to validate the measurements. In this case however, the main objective was to design a system that capable of producing results with an associated uncertainty below a specified value. Therefore, the building of the system began with the preliminary theoretical studies and experimental implementations, which required the use of some hardware parts and/or reference values, most of the hardware had already been pre-selected to implement in the system and only some improvements/adaptations were added afterward (discussed in the next subsections). The hardware needed to be constructed to verify the uncertainty budget before any measurements are attempted. Measurements will be discussed in Chapters 6 and 7.

Light Source

The same HeNe laser [14] (with wavelength 632.8 nm) was used as the system light source – due to the properties of the laser, a coherent small focus point of intense power is produced. The main advantage of using a laser light source is precisely the small round and uniform spot that is projected on the 2D sensor (as the spot diameter increases more pixels compose the shape of the captured image). A

non-coherent light source could also be used however, the larger, less circular, spot diameter could decrease the overall accuracy of the measurements – a smaller laser spot centre position does not vary as much over time and so the position uncertainty is expectedly smaller.

2D Sensor Camera

Depending on the light source, the spot to be analysed can have different properties which need to be distinguished by the light sensitive sensor. A camera's surface is composed by individual light sensitive elements, pixels (usually square) with an area that ranges, approximately, from 5 to 200 μm^2 (depending also on the type of camera), which allow the detection of very small changes in the position of a light spot [19]. If the sensor is able to detect changes in the range of the micrometre, with the help of a controller software such as LabVIEW it becomes possible to create a system that faithfully detects position changes in an *xy* graphic that corresponds to the sensor surface.

The same USB monochrome CMOS camera [15] used in Section 3 was selected, with a sensitive area of 1280 x 1024 (6.784 mm x 5.427 mm) square pixels with a length of 5.3 μm.

Sample Holder and Rotation Stage

The detection of a beam position shift with a camera must be traceable. In this setup, by rotating the glass plate, an optical path difference is created, which is directly related to the incident angle. A very simple way of ensuring that the measurements are accurate is by using a rotation stage, capable of performing small step increments. The stage chosen for this task, URS50BCC [17], is capable of performing steps with an accuracy of ± 0.01º by connecting it to a SMC100CC controller [20].

Since a characteristic shift in the camera is associated to a specific incident angle, many measurements of these two closely related properties generate results that mitigate measuring errors – no matter the change in the optical path, the material of which the glass is made remains unaltered, as does the associated refractive index. Using the SCM100CC controller, it was possible to generate fast and smooth sample sweeps around the centre position ($\theta_i \sim 0°$, when the incident beam is perpendicular to the sample surface).

With the objective of building a reliable system with an accuracy for RI measurements below 10^{-2}, a more detailed analysis is made to each parameter in the following subchapters. It is critical to characterize in detail the individual achievable uncertainties in order to have a good understanding of the overall system – hardware problems, performance and individual contributions for the system uncertainty – as well as its viability.

4.1 Uncertainty Budget

A useful approach of this analysis is the construction of an uncertainty budget that considers every parameter capable of affecting the uncertainty of the refractive index of glass. Each parameter can have more than one source of uncertainty associated to it, and each source often has a different weight in the final uncertainty of each parameter. As was stated before, θ_i, t and d, the incident angle, the sample thickness and the lateral displacement respectively, are the three main parameters to take into consideration for the uncertainty of glass refractive index measurements. In the following paragraphs, a more thorough analysis is made into each parameter and every relevant sources of uncertainty associated to it.

First however, a brief explanation on how the individual uncertainties are processed is considered useful – the process is applied in the same manner for every parameter under this study. All methods used follow the procedures set by GUM ("*Guide to the expression of uncertainty in measurement*" [21]) and EA-4/02 of the "*European co-operation for Accreditation*" [22]. The nomenclature follows the guidelines described in VIM ("*International Vocabulary of Metrology"* [23]).

The measurand (*G*), in this case, represents the value of the refractive index of glass and its estimate to be measured, g, is determined by N other estimated quantities (v_i), related through a functional relationship f, such that $g = f(v_1, v_2 \dots v_N)$. Each estimated input value v_i has a probability distribution for its values, and its associated standard uncertainty u_{v_i} can be evaluated as a Type A (based on frequency distributions) or Type B (based on *a priori* distributions) [21]. The uncertainty of every input value needs to be standardized to the same units and coverage level (k) before they can be combined, and the standardization process depends on the type of evaluation:

Table 4-1 – Type A or Type B uncertainty evaluation, associated probability distributions and standard uncertainty formulas.

Uncertainty Evaluation	**Probability Distribution**		**Standard Uncertainty $u(x_i)$**
Type A	**Statistics**		$s(\overline{v_i}) = \frac{s(v)}{\sqrt{j}}$
Type B	**Rectangular**		$\frac{a}{\sqrt{3}}$
	Normal	Measurements	$s(\overline{v_i})$
		Calibration certificate	$\frac{U}{k}$
		Manufacturer specifications	$\frac{Tolerance\ limit}{k}$

In Table 4-1, the standardization of the uncertainty is summarized according to the type of evaluation. In Type A evaluations, the standard uncertainty corresponds to the experimental standard deviation of the mean $s(\overline{v_i})$ which is equal to the experimental standard deviation $s(v_i)$ divided by the square root of the number of observations j. In Type B evaluations, and depending on the distribution process, the standard uncertainty can be determined by: the half-width of the input interval denoted by $a = (a_+ - a_-)/2$, the expanded uncertainty U and coverage level k or the *Tolerance limit*.

After every uncertainty from every input variable is standardized, they can all be combined (Type A and Type B) to form the combined standard uncertainty $u_c(g)$ (the positive root of the combined variance $u_c^2(g)$, or the quadratic component), if they are independent and not correlated [21].

$$u_c^2(g) = \sum_{i=1}^{N} \left(\frac{\partial f}{\partial v_i}\right)^2 u^2(v_i) = \sum_{i=1}^{N} c_i^2 u^2(v_i) = \sum_{i=1}^{N} u_i^2(g) \tag{4.1}$$

The uncertainty budget of this subsection is based on the mathematical model for the lateral displacement of a laser beam by a glass parallel plate, as described in Section 3.1. The sensitivity

coefficients c_i, corresponding to the partial derivatives of Equation (3.2 are displayed from Equation (4.2 to Equation (4.4 below.

$$\frac{\partial \mathrm{n}_{glass}}{\partial \mathrm{d}} = -\frac{n_{air}\cos^2\theta_i}{t^2\sin\theta_i\left(\frac{d}{t\sin\theta_i}-1\right)^3\sqrt{\frac{\cos^2\theta_i}{\left(\frac{d}{t\sin\theta_i}-1\right)^2}+\sin^2\theta_i}} \tag{4.2}$$

$$\frac{\partial \mathrm{n}_{glass}}{\partial \mathrm{t}} = \frac{d\cos^2\theta_i}{t^2\sin\theta_i\left(\frac{d}{t\sin\theta_i}-1\right)^3\sqrt{\frac{\cos^2\theta_i}{\left(\frac{d}{t\sin\theta_i}-1\right)^2}+\sin^2\theta_i}} \tag{4.3}$$

$$\frac{\partial \mathrm{n}_{glass}}{\partial \theta_i} = \frac{n_{air}\left[2\cos\theta_i\sin\theta_i - \frac{2\cos\theta_i\sin\theta_i}{\left(\frac{d}{t\sin\theta_i}-1\right)^2} + \frac{2d\cos^3\theta_i}{t\sin^2\theta_i\left(\frac{d}{t\sin\theta_i}-1\right)^3}\right]}{2\sqrt{\frac{\cos^2\theta_i}{\left(\frac{d}{t\sin\theta_i}-1\right)^2}+\sin^2\theta_i}} \tag{4.4}$$

The output uncertainty needs to meet a certain confidence level, so, by multiplying it by the coverage factor *k*, the expanded uncertainty U is obtained: $U = ku_c(g)$. With this expanded uncertainty, the result of the measurement can be expressed as $G = g \pm U$, expected to encompass a large fraction of the distribution of values that could be attributed to G – that is, RI measurements are expected in the form: $n_{glass} \pm U$.

In the next page, an example of a complete uncertainty budget is displayed, that determines the expanded uncertainty for a N-BK7 calibration sample (used to test the system latter on), for the following conditions: $t = 12\ mm$, $\theta = 36°$ corresponding to $d = 2.917\ mm$.

Table 4-2 – Example of an uncertainty budget table used to estimate the weight of every parameter associated with the measurement of the refractive index of a 12.046 mm thick glass sample.

Uncertainty components

Refractive Index of Glass, n_{glass}

Variable	Value	Un.	Symbol	Source of uncertainty	Evaluation process	Value of comp.	Un.	Type of evaluation	Divider	Standard uncertainty $[u(x_i)]$	Un.	Sensitivity coef. $c(x_i)$	Quadratic comp. $[u(x_i).\ c(x_i)]^2$	Un.	% of the comp.
Incident angle	36	°	θ_i	Accuracy	Manufacturer specs (no backlash)	0.01	°	B / normal	2.00	8.73E-05	rad	1.65E+00	2.06E-08		10%
				Resolution	Division	0.0005	°	B / rectangular	1.73	5.04E-06	rad	1.65E+00	6.88E-11		0%
				Offset accuracy	Optimisation with left-righ side	0.001	°	B / rectangular	1.73	1.01E-05	rad	1.65E+00	2.75E-10		0%
Sample thickness	12	mm	t	Permissible error	Certificate of Inspection	0.002	mm	B / rectangular	1.73	1.15E-03	mm	-6.46E-02	5.57E-09		3%
				Measurement uncertainty	Certificate of Inspection	0.0011	mm	B / normal	2.00	5.50E-04	mm	-6.46E-02	1.26E-09		1%
				Uncertainty of measurement	Study	0.003	mm	A / normal	2.00	1.50E-03	mm	-6.46E-02	9.39E-09		4%
				Resolution	Division	0.0005	mm	B / rectangular	1.73	2.89E-04	mm	-6.46E-02	3.48E-10		0%
Lateral shift	2.917	mm	d	Accuracy	Camera Centroid Study	0.0029813	mm	B / normal	2.00	1.49E-03	mm	-2.79E-01	1.74E-07		80%
				5 Cycle average	Stdev for 5 cycles from study	0.00025	mm	B / normal	1.00	2.50E-04	mm	-2.79E-01	4.88E-09		2%
Refractive index of air	1.00027		n_{air}	Calibration Certificate	Study	0.00002		B / rectangular	1.73	1.15E-05		1.46E+00	2.83E-10		0%
n_{glass}	1.5000											**Σ**	**2.16E-07**		
±	0.0009											**Combined standard uncertainty, u_c**	**0.00046507**		
	0.06%											**Coverage level, k**	**2.00**		
												Expanded uncertainty (95% confindence level) U	**0.00093015**		
												Expanded uncertainty (95% confindence level) U	**0.0620%**		

Table 4-2 confirms once again that the biggest source of uncertainty for the measurements of the refractive index is associated to the value of the lateral displacement. To better visualize the weight of each source of uncertainty, Figure 4.2 was created:

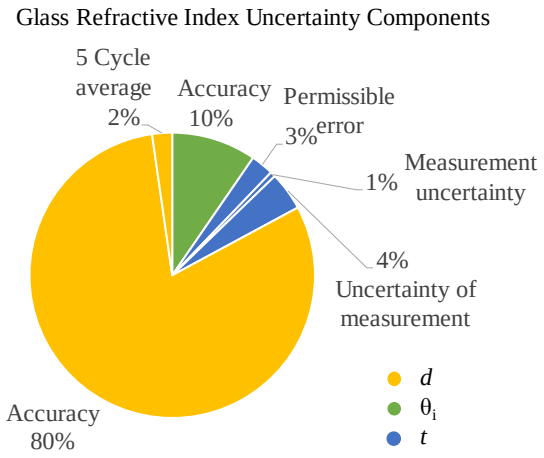

Figure 4.2 – Main component sources and their weight (in percentage), that contribute to the uncertainty in the measurements of the RI, associated to each parameter. The achievable magnitude of uncertainty, for every component, is indicated between brackets.

With this uncertainty budget, although simple, the importance of each parameter was determined and a value for the expanded uncertainty can be obtained. In practice however, some problems were observed that will be described in more detail in the following subsections which are already accounted for in the uncertainty budget displayed in Table 4-2.

4.2 Lateral displacement uncertainty components

It was concluded (Section 3.1) that the measurement of the lateral shift (or displacement), out of all the variables involved, had the greatest influence and contribution in the uncertainty in the final calculated values of the refractive index of glass. Therefore, it was necessary to evaluate the effects and interactions with the component that provides the values of d – the CMOS camera.

Neutral Filter

The camera is the sensor of the setup and naturally it is very sensitive; since the light source is a laser beam (of about 1 mW) a neutral filter, which transmits 0.0001% of the incident light (optical neutral density ND6) was placed in the aperture of the camera. Two possible positions for the filter were available: right after the laser source and just before the camera; since this setup relies on the sample alignment with the laser source and because the spot after the filter is difficult to visually track, the neutral filter had to be placed just before the camera. To further decrease contributions from external light sources (such as ceiling lamps) an opaque tube was also fitted between the camera aperture and the filter.

In this setup, the protective glass of the camera aperture was not removed to protect the sensor, and as such, unavoidable interference patterns similar to the one displayed in Figure 4.3 were present all across the sensor area – the protective glass acts as a parallel plate and when the coherent light source crosses it, an interference pattern is created. These patterns, already detected in the initial setup, were observed to be unaltered when there was no stage movement, as opposed the visible fringe shift when a movement of the camera was executed.

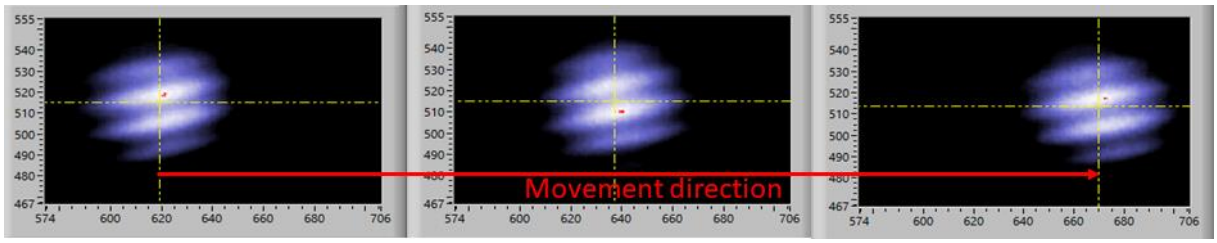

Figure 4.3 - Motion induced pattern shift in the captured spot image using the glass neutral density optic filter.

Since the interference pattern was always present, two options for the neutral filter were available: glass or film. By using a film filter, the pattern disappeared as illustrated in Figure 4.4 (c) – this pattern could be reduced if the distance between the filter and the camera increased, but by placing it closer to the laser source, the spot could no longer be detected by the observer, which made alignment operations unnecessarily difficult, as previously stated. Additionally, the visible speckle was observed to change over time in the same position, negatively impacting stationary measurements, but the main problem concerning the use of a film filter was related to the nature of the laser itself – the beam (of about 0.8 mW) could cause irreversible damage (deformities) to the filter over long periods of exposure.

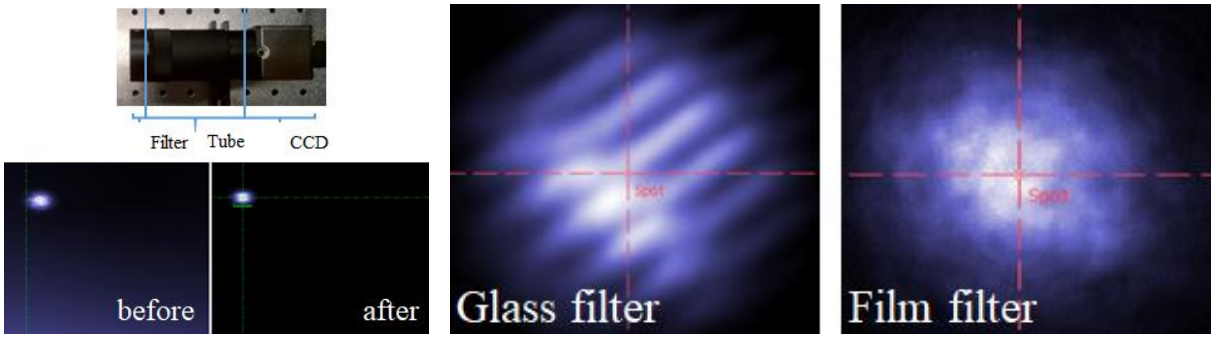

a) b) c)

Figure 4.4 – (a) Top: Camera setup with a ND6 filter adapted at the end of a 80mm opaque tube; Bottom: image before and after the application of the tube). Captured images using an optical neutral glass filter (b) and an optical neutral film filter (c).

For these reasons, the glass filter was used, despite the interference pattern which was essentially the same as the one caused by the protective window and that ultimately could be partially or completely masked by image filters.

Spot centre *xy* coordinates

The value of the lateral displacement is registered by determining the geometrical difference between the *xy* coordinates of the laser spot centre when the sample is perpendicular to the beam path ($\theta_i \sim 0°$) and when it is rotated ($\theta_i \neq 0°$), as demonstrated by Figure 2.2. A preliminary study was made to characterize the behaviour of the above mentioned interference pattern over the camera area as well as to analyse the accuracy of lateral displacement measurements, using two different methods for *xy* coordinate determination, Centroid and Gaussian, by using the setup illustrated in Figure 4.5, left.

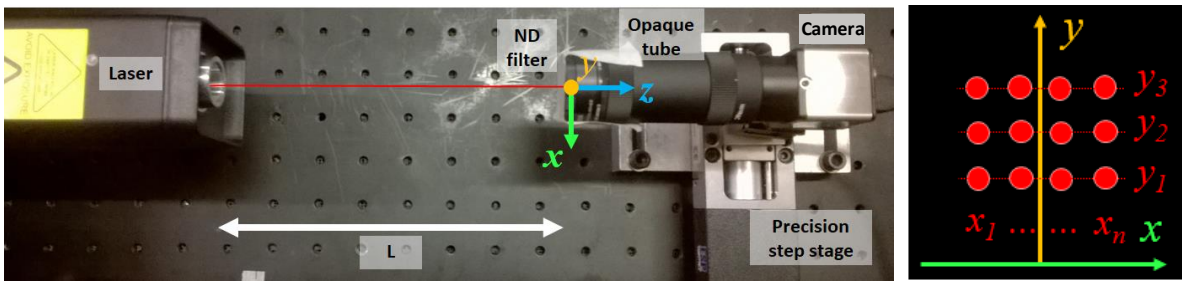

Figure 4.5 – Experimental setup (left) to verify the accuracy of spot measurements by two different methods (Centroid and Gaussian fit) over the camera area (right), where blue dots illustrate the measuring sweep along the x axis, for three different vertical positions.

With this setup, spot centre coordinates were collected for two different distances between the laser and the camera, $L = 25\ cm$ and $L = 50\ cm$ and three different sweeps were made along the camera *x* axis by using a one axis translation precision stage (MFA-CC [24]) in steps of 0.1 mm (illustrated in Figure 4, right). After every sweep, the laser vertical position was altered by approximately 0.15 mm increments, making it possible to test three different areas in the *y* axis.

A precision stage was used to ensure the traceability and accuracy of the measurements, capable of performing small step increments and compare them with the steps registered by the camera. For every movement of the stage (using existent MFA-CC controller software) the spot *xy* coordinates, determined by the two methods (Centroid and Gaussian), were recorded by a LabVIEW program and saved to a file for data analysis.

Taking into account all the measured points, and knowing that every step difference was known due to the precision stage, the average standard deviation shift, for every horizontal sweep, for three vertical positions, for two different laser/camera distances (L) can be summarized in Figure 4.6.

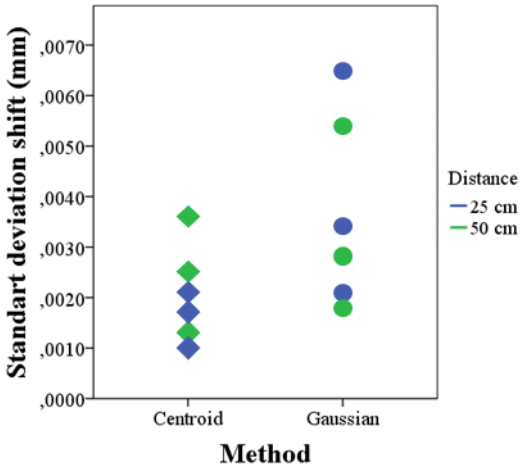

Figure 4.6 - Summary of the standard deviation shift (in mm) in each data set obtained in the study to determine the best method to find the centre coordinates of the laser spot. Purple markers represent results obtained for three different vertical positions with a distance between laser source and camera of 25 cm and green markers represent 50 cm.

Based on the results, it became clear that the Centroid method had a smaller position deviation shift, compared to the Gaussian method, which led to its selection to determine the *xy* coordinates of the captured images. Having selected the method, another analysis needed to be made, considering that a difference could be seen between the groups of measurements made at different distances. Comparing the results of the Centroid method for $L = 25\ cm$ and $L = 50\ cm$ helped determine if the influence of the distance between the laser and the camera had a significant effect in the centre position determination – the results can be viewed in Figure 4.7.

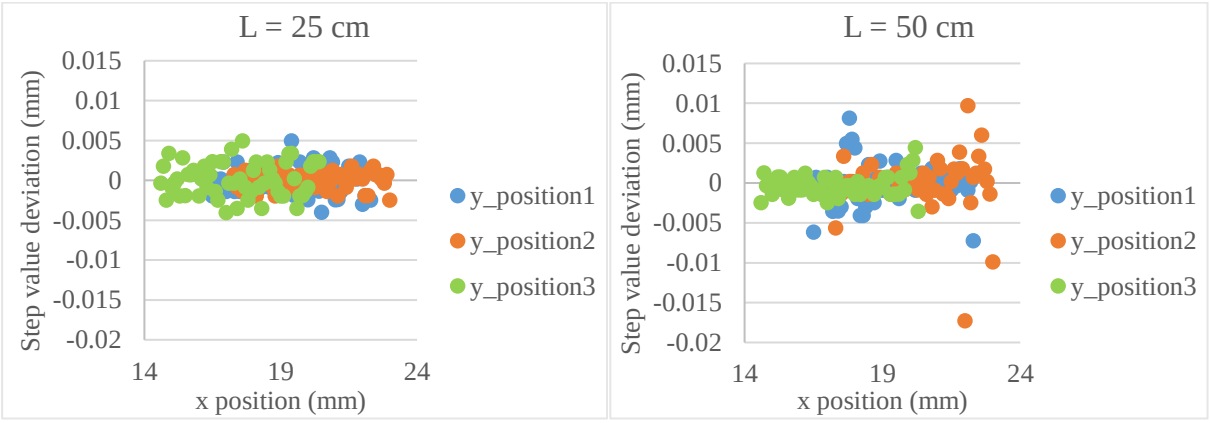

Figure 4.7 – Step deviation value for three horizontal sweeps in three different vertical positions (blue, red and green dots) for two values of L.

As confirmed by Figure 4.7, for a smaller distance ($L = 25\ cm$) between the laser and the camera, the step value is more stable, with a standard deviation of 1.7 µm. However, the uncertainty associated to different distances was not constant (Figure 4.8). To ensure that any measurement made by the camera had a defined uncertainty, the graph in Figure 4.8 was built. The straight red line is used to model the uncertainty, guaranteeing that for any measured distance a proportional uncertainty above the observed

value is associated – this way, the assigned uncertainty in the uncertainty budget is always guaranteed to be adequate.

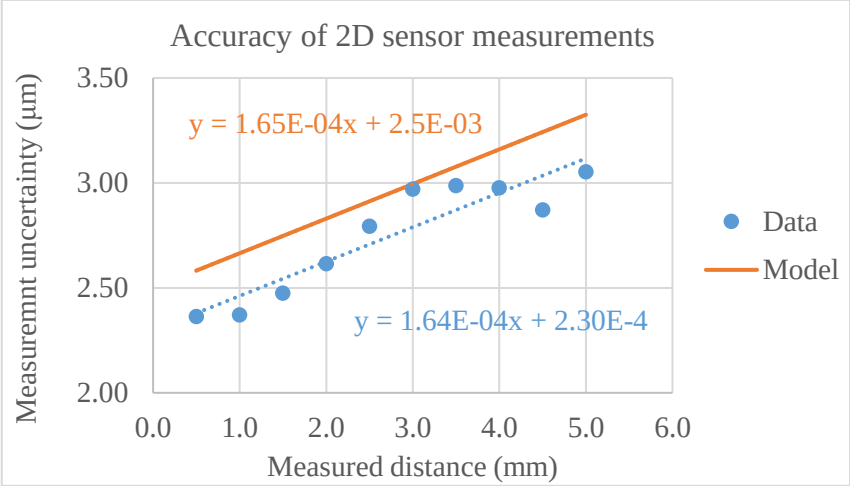

Figure 4.8 – Fitted model and associated equation (red) used to define the uncertainty in the accuracy of measurements made by the camera (blue).

While this managed the accuracy of measurements made by the camera, as it will be described in Section 4.4, if the sample to be analysed doesn't fit properly in the sample holder, small tilts could happen during measurements that slightly shift the position of the sample, making small changes to the OPD and causing slight variations in the measured values of d.

To analyse this possible source of uncertainty, five sweeps were made with a sample that perfectly adjusted to the sample holder. If any movement occurred, they could be considered negligible, making it possible to compare five values for the same angle and the resulting deviation associated as the uncertainty added by the rotating stage for every measurement, the repeatability of the system.

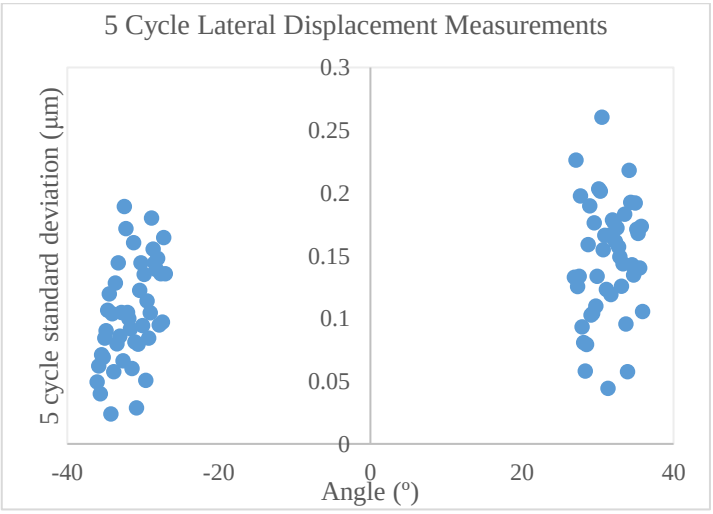

Figure 4.9 – Standard deviation of the lateral displacement, for five sweeps and wide angles, without tampering with the sample.

Analysing the dispersion in Figure 4.9, it was concluded that the standard deviation, for five sweeps and wide angles, was always below 0.25 µm and so this value was chosen for the repeatability component due to the stage movement. Only measurements for wide angles were analysed since the refractive index value has a decreased error to the average value (of all measurements) as the incident angle increases (discussed in Section 5.2).

This uncertainty will be the same for any sample – any uncertainty added by accidental tilts during sweeps by a sample that doesn't properly adjust to the sample holder will not be considered.

Uncertainty Budget

The lateral displacement is measured by the camera and its *Accuracy* needed to be studied, since this detailed information could not be obtained in the camera user manual (in this case, what was needed was the accuracy of the image, specifically associated to the used method for centre spot determination). The *Repeatability* of the results serves to consider any vibration made by the rotation stage that results in a sample misalignment.

The summary, related to the example illustrated in Figure 4.2, of the statistically significant contributions associated to the lateral displacement can be viewed in Table 4-3.

Table 4-3 – Sources of uncertainty, uncertainty evaluation process, value, type and weight in the uncertainty of RI measurements, linked to the lateral displacement d parameter.

Source of uncertainty	Evaluation process	Value	Type of evaluation	Weight
2D sensor Accuracy	Camera centroid study	Formula	B / Normal	80 %
Repeatability	5 cycle average	0.25 µm	B / Normal	2 %

4.3 Glass plate thickness uncertainty components

An earlier idea for this setup envisioned the determination of both the RI and the thickness *t* of the sample. However, since the values of n_{glass} and *t* are interrelated through Equation (3.2, it is not possible, through this technique, to determine one without having no knowledge of the other.

The thickness of every sample can be measured with good accuracy by using a micrometer screw gauge instead. To decrease the influence of user error, about ten measurements should be performed in the same area. The accuracy of the resulting average was maximized by considering double of its value stated in the calibration certificate.

Uncertainty Budget

The uncertainty sources for this parameter are all linked to the accuracy of the micrometer – through its *Certification of Calibration* and its *Resolution*.

The contributions of the plate thickness to the uncertainty in the measurements of the RI of glass, related to the example illustrated in Figure 4.2, are summarized in Table 4-4.

Table 4-4 – Sources of uncertainty, uncertainty evaluation process, value, type and weight in the uncertainty of RI measurements, linked to the sample thickness t parameter.

Source of uncertainty	Evaluation process	Value	Type of evaluation	Weight
Permissible error	Cert. of inspection	2 µm	B / Rectangular	3 %
Measurement uncertainty	Cert. of inspection	1.1 µm	B / Rectangular	1%
Uncertainty of measurement	Study	~ 3 µm	A / Normal	4%
Resolution	Division	0.5 µm	B / Rectangular	~ 0%

4.4 Angle of incidence uncertainty components

The accurate measurement of the incident angle is critical to the correct determination of the refractive index of any glass sample. According to what was explained in Section 3.1, to each value of lateral displacement, captured by the camera, is associated a distinctive value for the incidence angle – for the same sample, it is always expected that a certain value of θ_i always causes a certain fixed deviation of d.

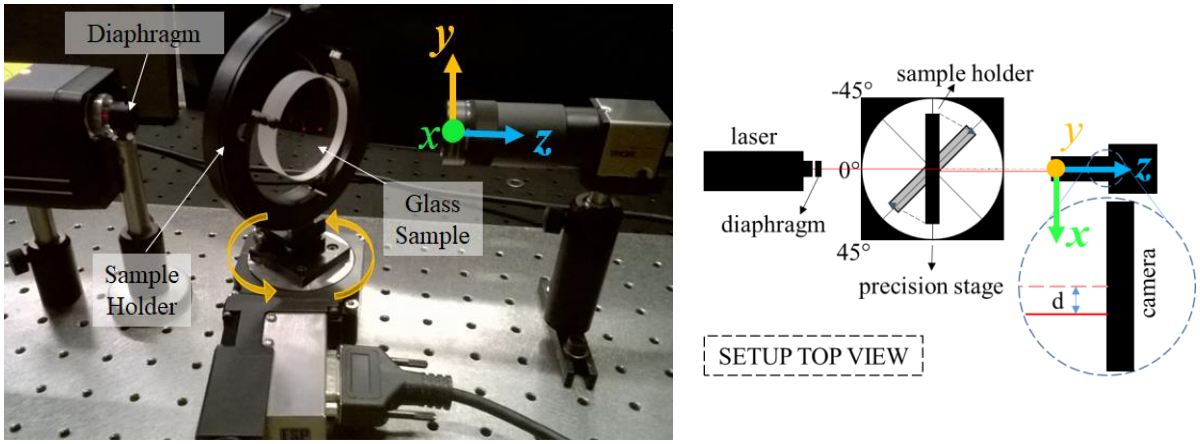

Figure 4.10 – Left: Rotation of the glass sample creates an optical path difference (only visible in the left image at the entry and exit laser points). Right: Top view schematic of the GOLD setup.

Although the value of the incident angle is measured automatically by a rotation stage, preliminary studies were made in order to better understand how a misalignment can occur, and how much it can contribute to an offset in the measurements of the *xy* coordinates of the spot on the camera.

Zemax Simulations

Preliminary simulations in Zemax of sample misalignments or tilts help to evaluate their impact when small changes are being made in the setup. An offset or tilt is added to the simulation, and the results are compared with the ideal setup.

Misplacement of the sample in the sample holder will lead to a tilt in one or both axes (*x* and *y*). The setup was designed to perform rotations about the sample holder *y* axis, which is concentric with the glass sample, and it was expected that the sample remained secured throughout any motion executed by the rotation stage. In Figure 4.11 simulated data from two different situations can be seen:

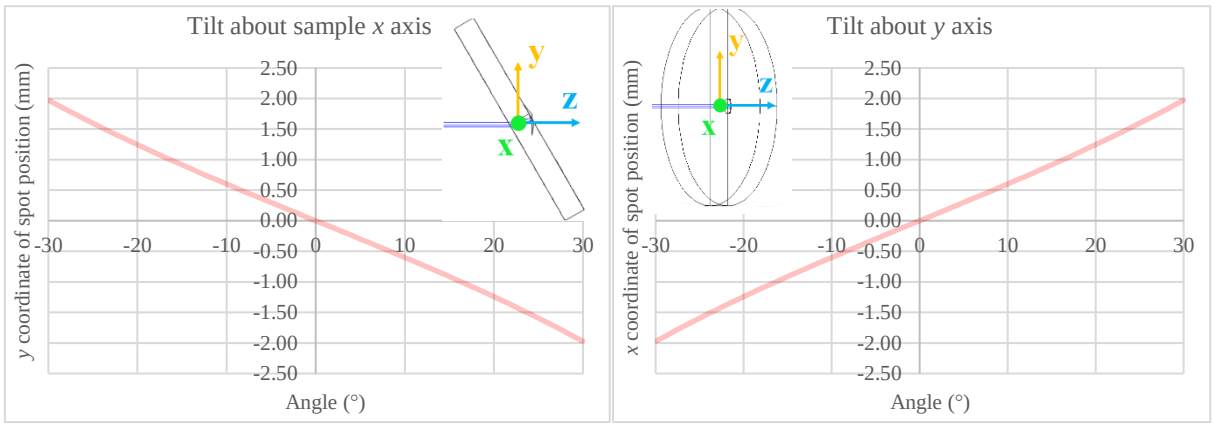

Figure 4.11 – Study of the spot position shift in the y coordinate (left) or x coordinate (right) by rotating a 10mm thick sample x or y axis, respectively, from -30º to 30º.

On the right graphic, the simulation shows the ideal situation already presented in Section 3.1 (displacement of the *x* coordinate, the *y* coordinate is not affected), while on the left graphic the sample is made to turn about the *x* axis, which causes a shift in the *y* coordinate of the laser spot (the *x* coordinate is not affected).

The exaggerated representations shown in Figure 4.12 serve to better illustrate the effect of a tilt on each axis, but in practice and after some alignment, the deviations are not as significant - although they continue to have a negative impact on the results for the RI.

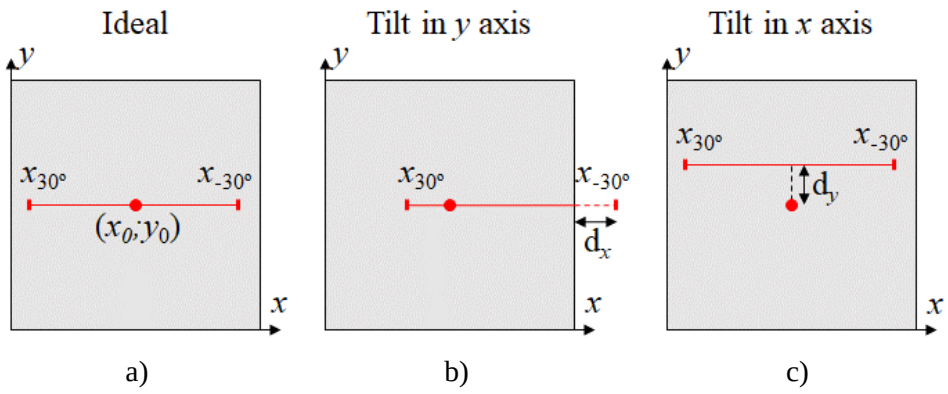

Figure 4.12 – Acquired data (red line) over the camera area in ideal conditions (a) and the influence of a tilt in the y axis (b) and x axis (c).

A tilt in the *y* axis has higher consequences, since it could mean that some of the laser spots are located outside of the sensitive area of the camera and therefore not considered as measurements. In the case of a tilt in the *x* axis, a vertical deviation is introduced to the data – these results can, in most cases, still be used to compute the value of the RI of the sample, by adjusting the data with reference to the centre position (x_0 ; y_0 coordinates).

The chosen sample holder aimed to secure the sample so that no matter the amount of performed sweeps the path crossed by the laser beam would be the same – eliminating any problems caused in case of inhomogeneity (associated to the manufacturing of the glass).

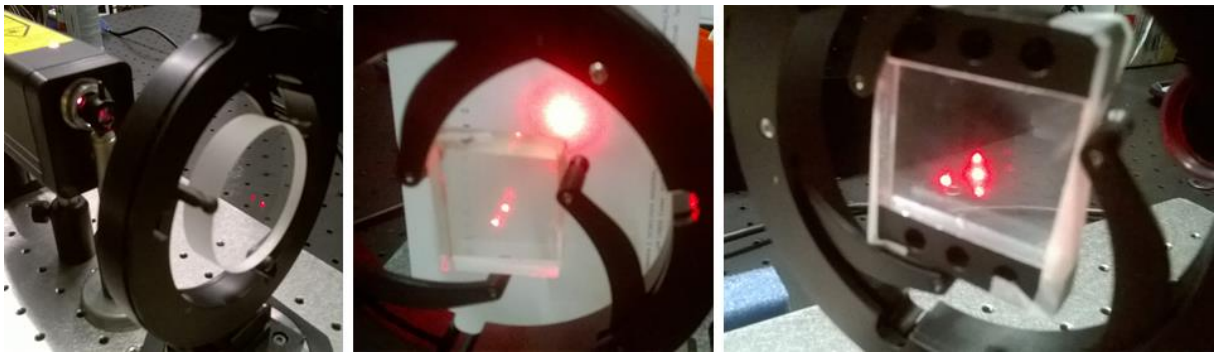

a) b) c)

Figure 4.13 – Sample suitability to the sample holder. (a) round calibration samples and no detected problems. (b) square LSC sample, difficult to secure in sample holder. (c) small square LSC sample adapted with parts to stay in place.

In practice however, only round samples proved to remain securely firm in the chosen sample holder. As can be seen in Figure 4.13, samples with a squared shape were comparatively much harder to stabilize in the sample holder, and in some cases, if the sample was square and relatively small, spare parts had to be fixated (Figure 4.13, c) to manage a good grip by the sample holder. This lack of stability resulted in the measurement of the lateral displacement in different locations of the sample, testing these sample's homogeneity simultaneously (if the sample is homogeneous, the value of the RI is not affected by the tested area).

Before any measurements took place, it was then necessary to explore the impact of any further unforeseen properties that could alter the alignment of the sample.

Sample Alignment

The rotating stage was placed on the setup and aligned has shown in Figure 4.10 left – its measurements have an accuracy of $\pm 0.01°$ and a ± 0.005 resolution, according to the manufacturer. Accurate measurements require a good alignment between the laser beam and sample surface as shown in Figure 4.10 right, by the position of the opaque black sample holder.

The alignment of the sample is made in two steps, first visually, then by using the camera and LabVIEW program. A pre-visual alignment, although less accurate, decreases both time spent on alignment processes and the value of the offset in both axis to be used later – it can be regarded as an

"initial guess" made by the user. Before anything else, it is necessary to capture the position of the spot in the camera (the (x_0 ; y_0) position), without a sample in the sample holder.

Introducing a diaphragm right after the laser source helps the manual alignment procedure. To ensure that the diaphragm was correctly aligned with the laser, the laser spot target seen in Figure 4.14 was set at approximately 2 meters distance from the laser and glass sample. By doing this, the interference pattern where visible to the naked eye, which made the alignment process easier. In Figure 4.14, (b) and (c), the displayed interference patterns correspond, respectively, to a situation where the alignment changes from poor to adequate.

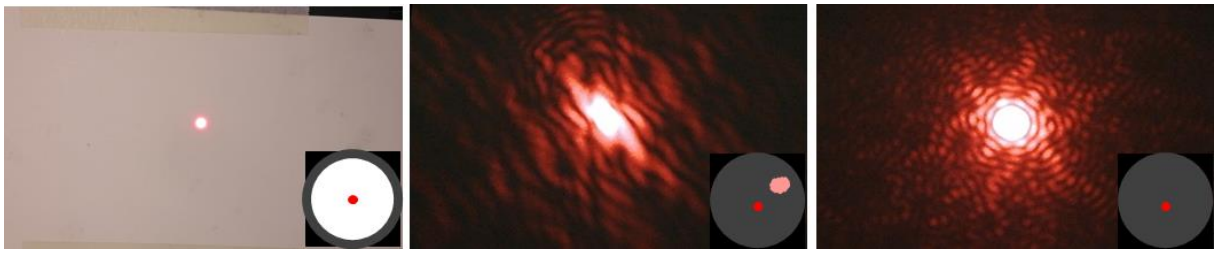

a) b) c)

Figure 4.14 – Alignment of the beam with the help of the diaphragm and transmitted image. (a) the diaphragm is completely open; (b) the diaphragm is closed and a reflection by the glass surface can be seen (pink spot); (c) the diaphragm is closed, and the sample is correctly aligned.

After ensuring the correct alignment with the laser aperture, closing the diaphragm to its minimum doesn't have any effect on the transmitted beam intensity but makes it easier to visually detect the reflection made by the glass surface back in the diaphragm (Figure 4.14, (b), small picture bottom right) and adjust it accordingly so that its diffraction pattern (pink) is concentric with the diaphragm hole (Figure 4.14, (c), small picture bottom right).

When the reflection spot is adjusted so that it coincides with the laser spot, a good visual alignment is achieved, that is, the laser beam is perpendicular, or very close to it, to the sample surface and the next alignment step can be made.

For the final alignments, the initial position of the beam (the previously captured (x_0 ; y_0) now (z_x ; z_y) in LabVIEW) can be used as a reference in the final adjustments to the sample, via LabVIEW, effectively setting the zero of the camera *xy* coordinate system.

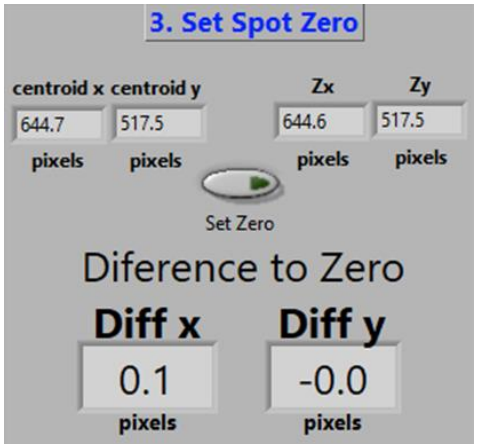

Figure 4.15 – Section of the LabVIEW user interface that helps the user set the laser spot zero (x_0 ; y_0) in real time, with an accuracy up to 0.1 pixel.

By following this procedure, a good alignment of the sample was achieved almost always, however, considering that some samples where not a good fit in the sample holder, and extra step was made to ensure the correction of an offset in the sample.

Alignment Offset

It was discovered that a less precise alignment produced an asymmetry in the results, that although not critical, became more accentuated in greater angles of incidence (a greater incident angle causes a greater OPD, which is easier to track in the camera). The principle behind this is related to the fact that if a sample is homogeneous and if the incident beam is perfectly perpendicular to the sample surface, then a rotation of equal amplitude (to both sides) about this point should produce RI values symmetrical about the computed average value for all incident (as seen in the theoretical model). To correct this offset, an optimization is made using the acquired data.

Considering the values obtained for grater angles of incidence, the difference between these two averages in an ideal situation would be equal to 0.

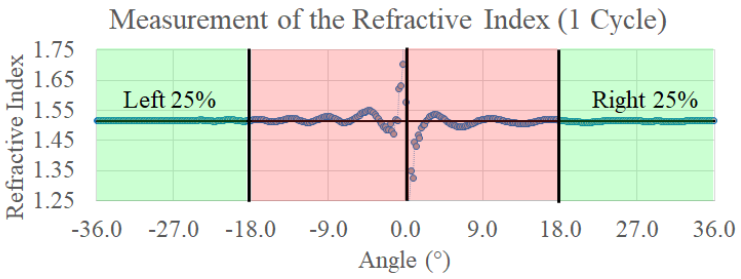

Figure 4.16 – Plotted data of the measured values for the RI of the sample. The middle 50% of the measurements not used for the calculation of the difference between left and right averages of the RI.

However, that is never the case in practice so taking the recorded data for a cycle made by the rotation stage, a small offset is added and subtracted to the measured angle, creating two new sets of results. Each set has a different value for the difference (*df*), in percentage, between the left and right averages of the measured RI. These results have the same properties as the original but are deviated by a factor of $\delta\theta$.

$$df = \frac{\overline{RI}_{left} - \overline{RI}_{right}}{\overline{RI}} \tag{4.5}$$

Table 4-5 – Properties of the three sets associated to 1 cycle of measurements made by the rotation stage. Three different values of df are obtained, making it possible to create a plot in order to determine the angular offset.

$\theta = \theta - \delta\theta$	Original data	$\theta = \theta + \delta\theta$
$\theta - \delta\theta;\ d_{-\delta\theta}\ ;\ RI_{-\delta\theta}$	$\theta\ ;\ d\ ;\ RI$	$\theta + \delta\theta;\ d_{+\delta\theta}\ ;\ RI_{+\delta\theta}$
$df_{-\delta\theta}$	df	$df_{+\delta\theta}$

Each set provides a value of the difference between the left and right averages of the measured RI, and when these three values are plotted, the value of the angle offset can be found (red dot in Figure 4.17).

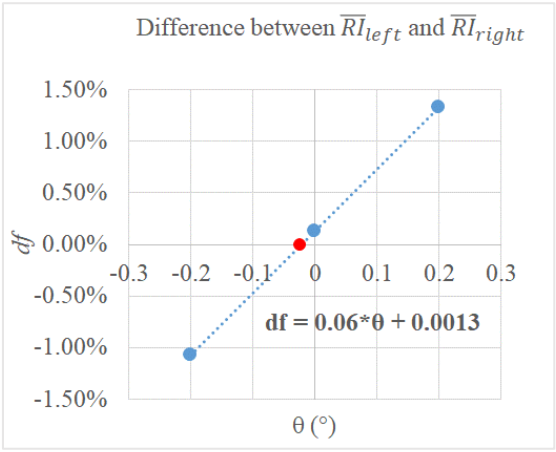

Figure 4.17 – Three point plot of the value of df from three sets of results. The angle offset corresponds to $df = 0$ *(red dot).*

This angle offset works on the assumption that the sample is parallel plated and has an accuracy of $\pm 0.001°$. Glass used in optical applications undergoes rigorous manufacturing processes. But what would be the impact in the accuracy of the lateral displacement, if the glass sample displayed a wedge?

4.4.1 Glass plate wedge effect uncertainty component

Refractive index results are greatly influenced by the shape of the sample itself – critically so when it comes to its thickness, just has it has been shown in a previous subsection. However, it is expected that not every sample to be analysed has passed through rigorous manufacturing procedures regarding its shape. Especially if the application purpose, as is the case with the glass designed for LSC windows, does not require as much precision as an optical application, the glass parallel surfaces that delimit the optical path inside the sample may not be perfectly parallel. As such, a wedge effect should be considered on the exit surface – the entry surface is aligned with the incident beam, and is effectively perpendicular to it, any wedge effect related to this surface can be accounted for in the exit surface.

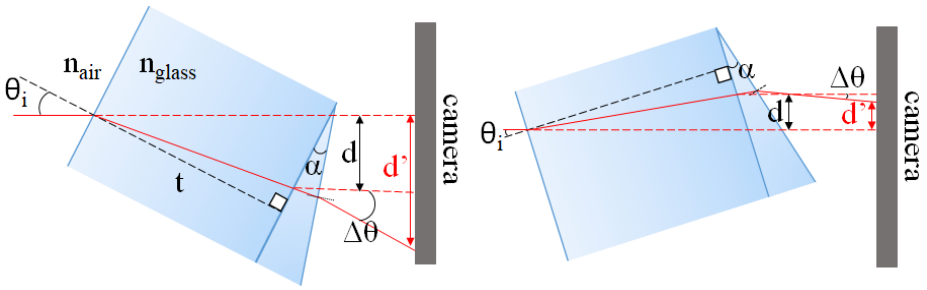

Figure 4.18 – Beam path crossing a sample with a wedge (proportional to α) (left) and its influence in the measurement of the lateral displacement (right).

It is known that a wedge in a sample affects the path of the beam [25], however, it became necessary to assert its behaviour and influence and how it related to the wedge axis – a sample can have a wedge that is orthogonal to *x* or *y*. To study this phenomenon, simulations in Zemax were created, based on a 10 mm BK7 glass plate (with known RI) and using the wavelength of a HeNe laser (632.8 nm). The spot position after it crossed the sample was registered between -30º and 30º in 1º steps. Simulation results of the displacement in the *y* coordinate of the spot, for wedges in the *x*, *y*, or *xy* axis can be viewed in Figure 4.19.

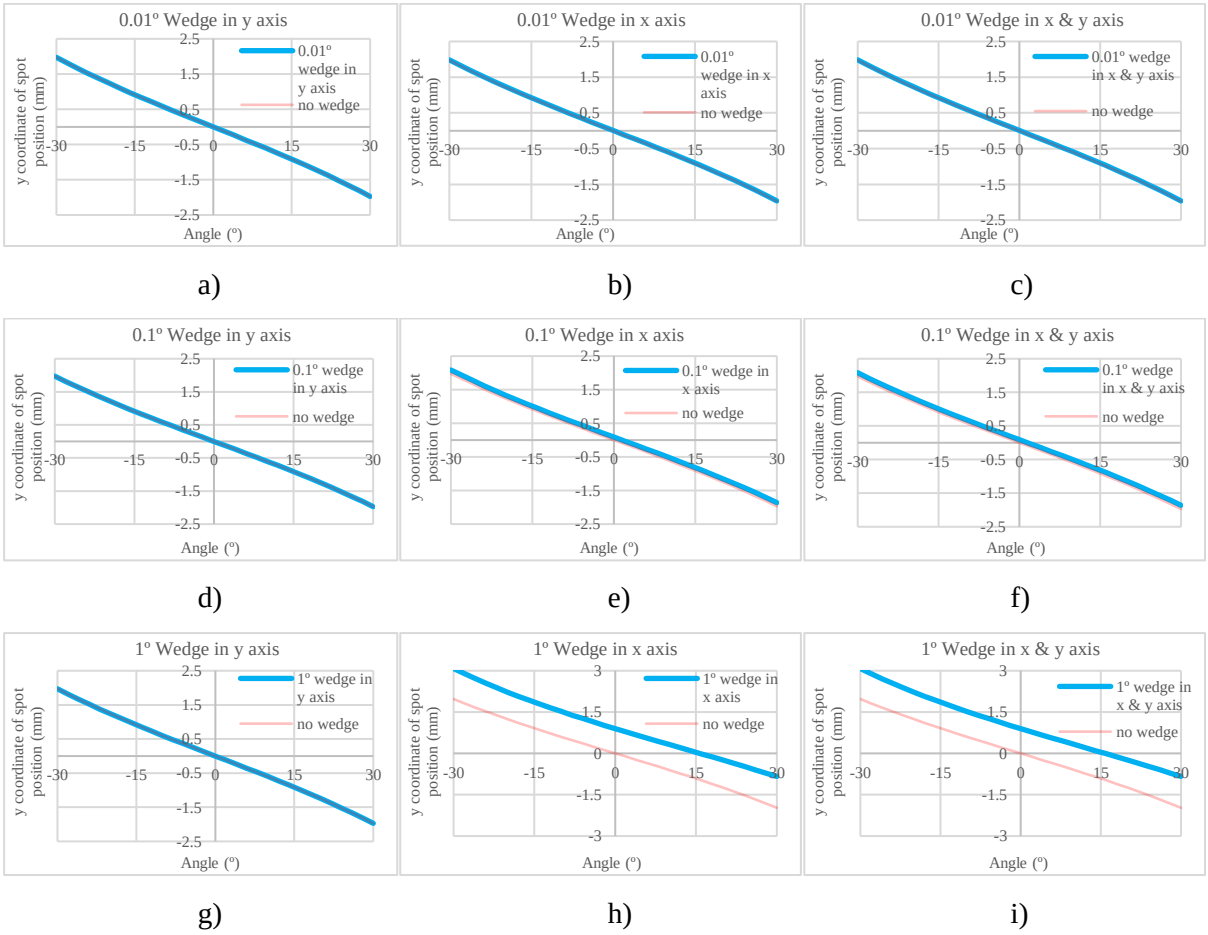

Figure 4.19 – Study of the spot position shift in the y coordinate due to the introduction of a wedge in the sample of, respectively, +0.01º (top), +0.1º (middle) and +1º (bottom).

By looking at the bottom three graphs (g, h and i) and comparing the value of the shift in the *y* spot coordinate that depends on the value of the wedge it can be concluded that a wedge in the *x* axis of the sample represents the main contribution to the uncertainty in the value of the displacement. In this worst-case scenario, comparing the resulting refractive index and the BK7 sample known value wields an error of about 10^{-3}, which does not significantly change when a *xy* wedge scenario is considered. Considering a very small wedge instead (0.01º, a, b and c), the error value does not exceed 10^{-7} (10^{-5} if $\alpha = 0.1°$, d, e and f).

It can now be said that a wedge around 1º or higher is associated to a low quality (LQ) sample (worst case scenario) and it is expected that any sample to be analysed by this method does not have a wedge

value as high. So, for the purposes of this application, the value of the wedge was considered negligible, and therefore not considered to contribute to the uncertainty in the measurements.

Uncertainty Budget

The incident angle is always determined automatically by the rotation stage briefly described in the previous section (URS50BCC), so it is straightforward to conclude that two sources of uncertainty associated to this parameter are the *Resolution* of the stage and its *Accuracy* in the measurements themselves. The third source was added after observation of preliminary results (covered in Section 4.4) where a slight variation in the results was detected, associated to the alignment of the beam with the sample, the *Offset accuracy*. As discussed in Section 4.4.1, a wedge in the sample was considered to have no effect in the uncertainty of the results.

The contributions of the incident angle to the uncertainty in the measurements of the RI of glass, related to the example illustrated in Figure 4.2, are summarized in Table 4-6.

Table 4-6 – Sources of uncertainty, uncertainty evaluation process, value, type and weight in the uncertainty of RI measurements, linked to the incident angle θ_i parameter.

Source of uncertainty	Evaluation process	Value	Type of evaluation	Weight
Accuracy	Manufacturer specs	0.01°	B / Normal	10 %
Resolution	Division	0.0005°	B / Rectangular	~ 0 %
Offset accuracy	Left-right optimization	0.001°	B / Rectangular	~ 0 %

All the main parameters that contributed to the uncertainty of measurements of the refractive index of glass samples have been described individually. All the gathered information was used for the construction of the general uncertainty budget for the RI in subsection 4.1.

5. GOLD Control System, Data Acquisition and Processing

At this stage, the setup design concept has already been described in the previous chapter. It was critical to first determine how the system performance would be affected by the uncertainty of the physical interactions with the sample and the setup hardware, before taking any measurements and analysing results. After the uncertainty budget was developed, it became easier to understand what would be required of the LabVIEW code and how to implement it taking the setup interactions into consideration. To find the value of the refractive index of parallel glass plates, part of the process needed to be automated by a LabVIEW code.

This thesis proposes the creation of a simple user interface capable of acquiring the values necessary for the determination of the refractive index of optically simple, parallel, glass plate samples. The process a user needs to follow in order to obtain the RI of a sample is as follows:

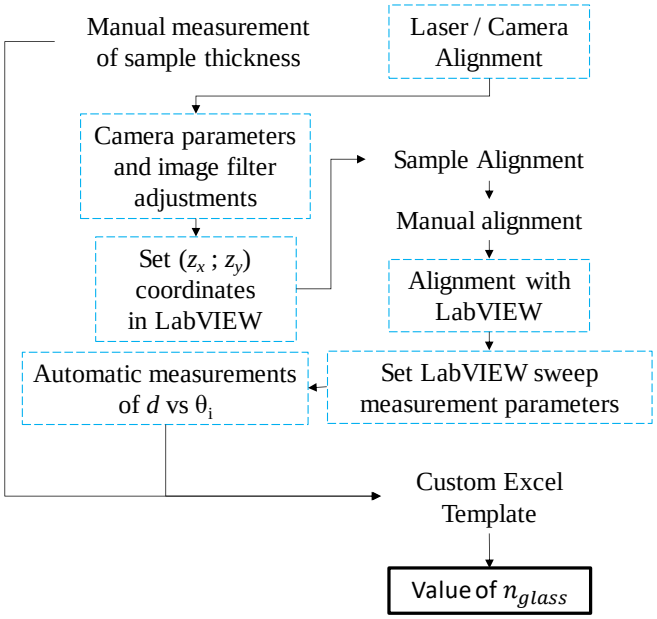

Figure 5.1 – Process diagram of the steps that need to be performed to obtain the value of the RI of a glass sample. The blue dashed squares indicate steps assisted by the LabVIEW user interface.

Most of the processes depend on LabVIEW as indicated by Figure 5.1 (blue dashed squares), specifically the alignment of the sample and the measurement of the lateral displacement (in the form of coordinates of the spot centre) with respect to the incident angle. Once these measurements are made, the data is ready to be used to find the refractive index of the tested sample.

The determination of the refractive index was implemented on a custom Excel spreadsheet because at the time it was easier to view and troubleshoot the processing of the data by steps – in future upgrades, the value and uncertainty should also be calculated by LabVIEW. The following subchapters describe in detail how both the LabVIEW .vi and the custom Excel template work to achieve measurements of the RI.

5.1 GOLD Control System and Data Acquisition

Based on the setup presented on Chapter 4, control of the camera and rotation stage was developed in a LabVIEW code. There are two main phases in the process of acquiring measurements of the centroid *xy* coordinates – first, the setup and adjustment of both equipment and associated parameters "*Camera Configuration & Sample Alignment*" and second, the acquisition of values "*Lateral Displacement Position Acquisition*".

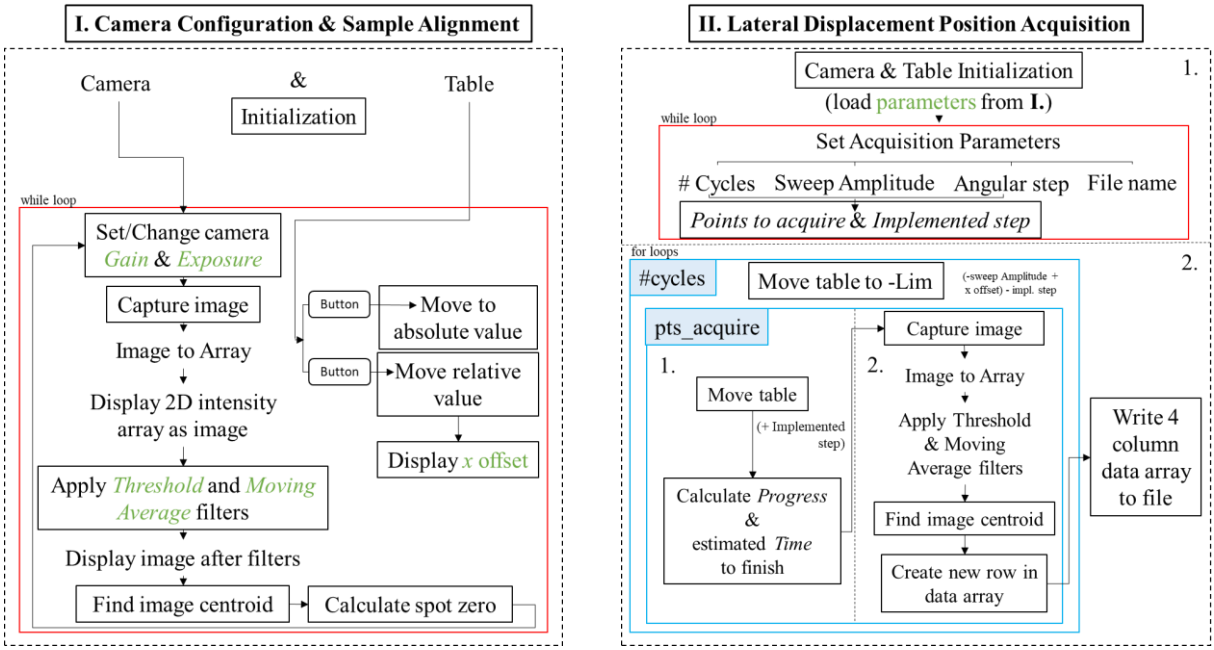

Figure 5.2 – Simplified block diagram of the LabVIEW program behaviour to carry out measurements of the xy coordinates (centroid) of the spot.

Although the developed code automates the measurement of the lateral deviation, it can't independently determine if the image has high quality – it simply executes movements and records values. A great amount of interaction by the user is necessary for the adjustment of parameters and initiation of sub processes – it is the user that defines if the image spot is ideal and if the sample is correctly aligned before the code can proceed to phase two in which measurements also only begin when the user is satisfied with the specified measuring parameters.

5.1.1 Phase I: Camera Configuration & Sample Alignment

The user has access to the first page of the LabVIEW user interface depicted in Figure 5.3 (the block diagram can be viewed in Annex 10.1,), a simple code accepts a 2D data array and proceeds to compute the weighted average of the intensity peak (because this particular camera is monochrome) in *x* and *y*, therefore outputting the *x* and *y* coordinates of the centroid $C_{[x,\,y]}$, identified in Figure 10.3 as *p0* and *p1* respectively. This method presents a disadvantage if used to calculate the centroid of an irregular shape. For instance, if an image has an irregular spot (Figure 5.9) and can interact with it according to the list in Table 5-1. The left graph is used to show the entire area of the camera (1024x1280) and the spot position in it, while in the right graph, the chart area is fitted to the centre area of the camera showing the zoomed in image of the captured spot. The objective in the first phase of the code is to adjust the

camera *Exposure* and *Gain* parameters, apply *Threshold* and *Moving Average* image filters to a setup without a sample and once these parameters are set, the user can place the sample in the sample holder and perform any necessary alignments (centroid coordinates are displayed as a yellow dashed cursor).

According to Figure 5.2, after initializing the equipment, LabVIEW enters a while loop performing the necessary steps to refresh the captured image in real time. As illustrated in Figure 5.4, bottom, some adjustments need to be made to the image (left), before it can be used for lateral displacement measurements (right).

The camera parameters must be adjusted so that the captured laser spot image achieves around 90% – 100% of the *Dynamic Range*. The dynamic range serves as an indicator to prevent over saturation of the captured image – values above the established maximum pixel intensity value (255) in one pixel can still occur, however. In this case, a *Saturated* indicator appears near the graphic area, and it serves as a warning to the user – if measurements are taken with the current settings, a negative influence from the saturated pixel to its neighbours can result in a decrease of accuracy.

Next, to eliminate possible contributions of the surrounding environment, the *Threshold* and *FilterN* should be adjusted in a way that, respectively, diminishes the spot diameter and decreases the contribution of the interference pattern. A more thorough explanation on how the image filters work is given in subchapter 10.1 of the Annex.

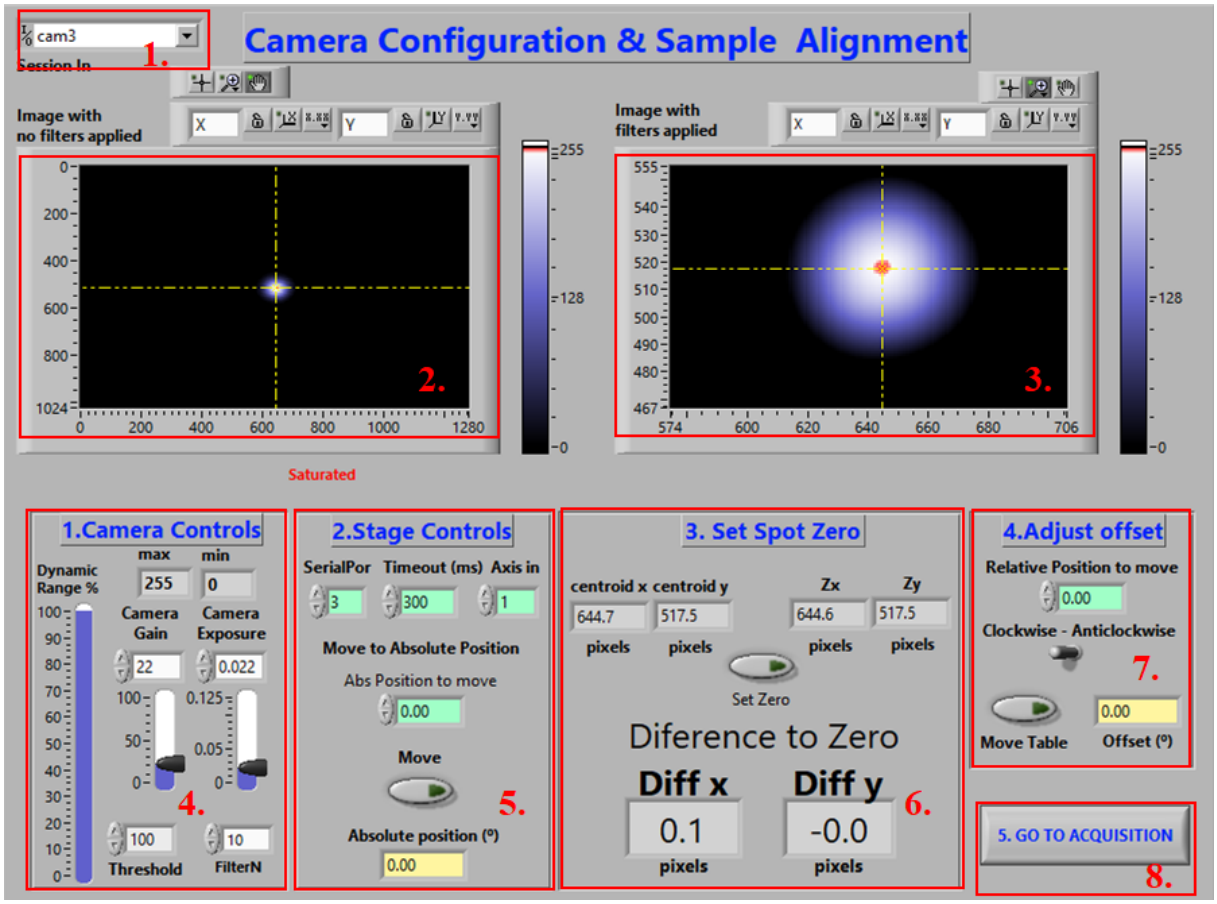

Figure 5.3 – First page of the front panel of the program in which the user can interact. The user made configurations of the camera and sample in this first phase influence the measurements made in the second phase of the code.

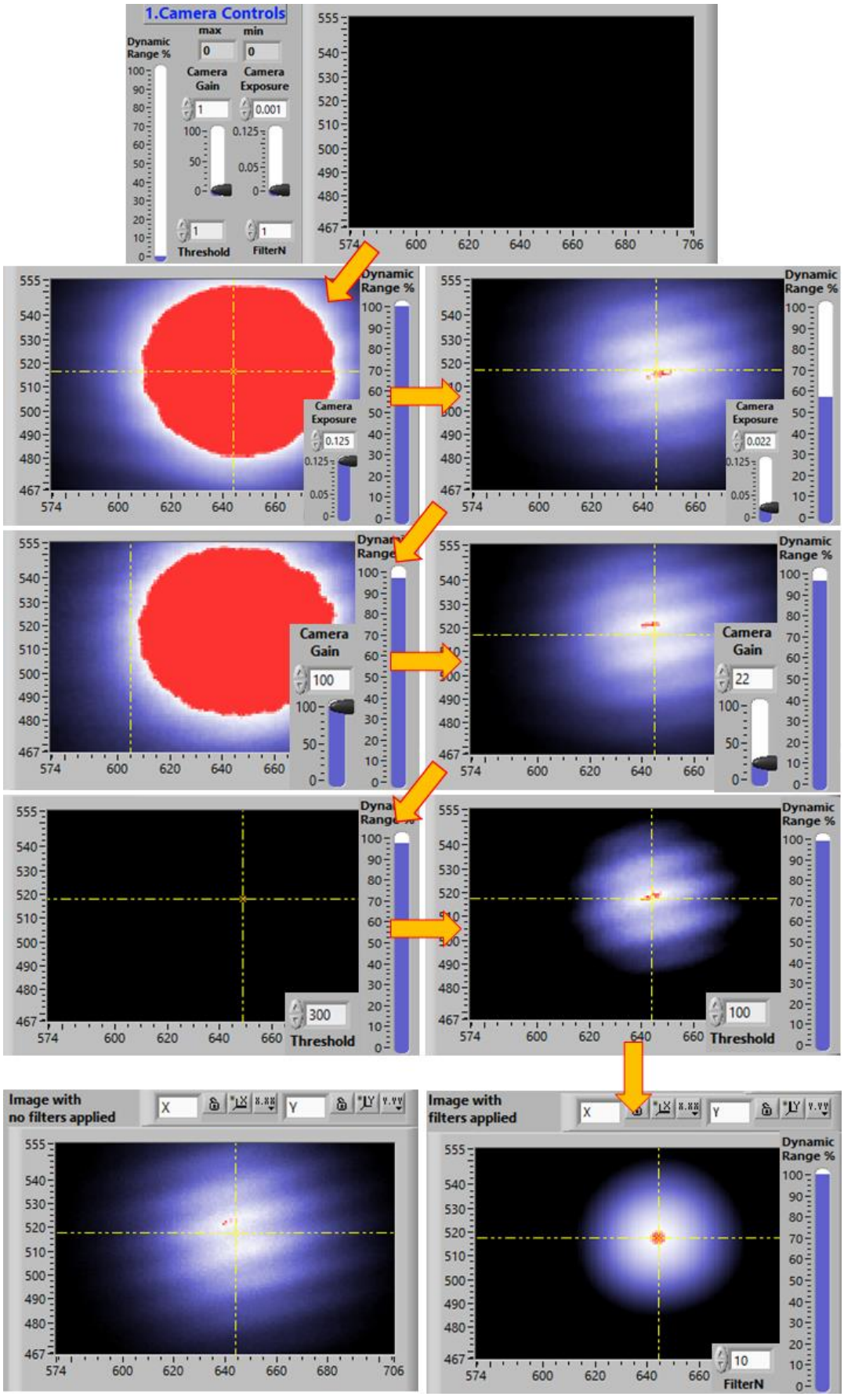

Figure 5.4 – Steps to perform (yellow arrows) , and influence of the parameters, to achieve an adequate image spot for lateral displacement measurements

Table 5-1 – Captions for Figure 5.3. The numbered red squares in the figure are linked to the Number column, and each represents a sub module briefly described in this table.

Number	*Name*	*Description*
1	**Session In**	Selects the camera to be used by the program
2	**Image before**	Captured image before filters are applied, and its position in the camera
3	**Image after**	Zoom of the laser spot, after filters are applied
4	**Camera Controls**	Displays the Dynamic Range of the image, and allows the user to change the values of the camera *Gain* and *Exposure*, as well as the values of the filters *Threshold* and *FilterN* displayed in **Image after**
5	**Stage Controls**	Allows the user to select the Serial Port, Timeout and Axis In as well as freely move the stage to an absolute position
6	**Set Spot Zero**	Without the glass sample, the captured laser spot is the reference to zero. Setting this reference helps with sample alignment
7	**Adjust Offset**	After setting the zero of the laser spot, the sample can be aligned in the *x* axis by moving the stage a relative step in both directions
8	**Go to Acquisition**	Allows the user to proceed to the next phase in the program

An adequate image result (after parameter adjustments) is displayed on the right graph in Figure 5.3.

With a well-defined image spot, and after setting the spot zero coordinates (x_0 ; y_0), the user can now insert the sample into the sample holder and adjust its *xy* alignment. This is necessary in order to achieve better alignments – the diaphragm is useful to adjust the general position to set a perpendicular position with respect to the incident laser beam, but the final adjustments can only be made resorting to the pixel differences to the spot in the zero position – since the adjustments are in the order of 2~3 pixels (two small for the human eye to distinguish).

Based on the spot zero coordinates, LabVIEW continuously displays the difference between the zero and the current spot coordinates (Figure 5.5, left).

Figure 5.5 – Sample alignment: (Left) LabVIEW interface that allows the setting of the spot zero coordinates Zx and Zy and monitors the pixel difference with the current coordinates. (Centre) Sample's x axis alignment. (Right) Mechanical piece of the setup that allows the user to tilt the sample's y axis.

Final adjustments to the *x* coordinate can be made by rotating the stage "*Adjust Offset*" (Figure 5.5, centre) or to the *y* coordinate by manually tilting the sample holder (Figure 5.5, right). To check if the sample has a good vertical alignment, the user can rotate it by 180º (in "*Stage Controls*") and verify the pixel difference – if it is not similar (with a difference a few pixels) to the one for 0º, the sample is tilted in its rotation axis and must be readjusted. When the indicated difference between the centroids (zero and current) is the lowest possible the sample is ready to begin measurements.

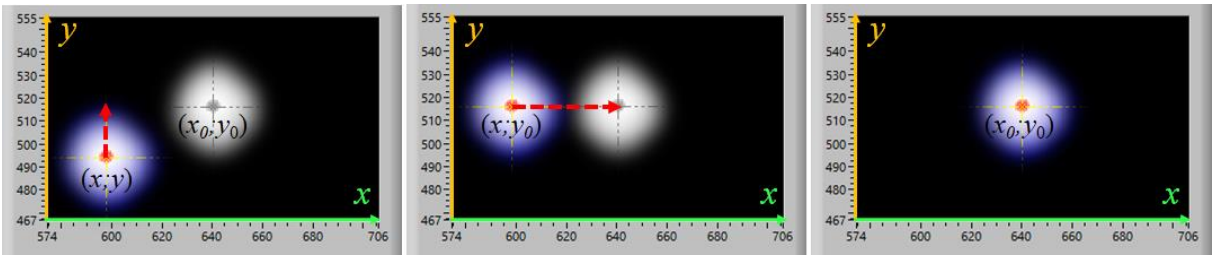

Figure 5.6 – Alignment of the laser spot (x ; y) after the sample is placed in the sample holder by comparison with the spot zero coordinates (x_0 ;y_0).

When the user is satisfied with the image and alignment, by pressing *Go to Acquisition* (Figure 5.3, number 8) the second phase of the code (Figure 5.2, right) "*Lateral Displacement Position Acquisition*" begins and LabVIEW switches to the second interface page.

5.1.2 Phase II: Lateral Displacement Position Acquisition

The position acquisition of the lateral displacement is executed in two steps. First, the user indicates the number of desired cycles (or sweeps) as well as the angular amplitude]0°; 90°] that computes the range of the sweep (e.g. if 36° is entered, the cycles will be executed from -36° to 36°) and the desired angular step. The program then automatically calculates the number of points to acquire in the range of the sweep and adjusts the steps if necessary (*Implemented step*) – this forces a measurement when $\theta_i = 0°$ to allow post-optimization of the angular offset. The user also defines the file name (*FileName*) that will be created when the program finishes its execution – in the file, each pair of centroid *xy* coordinates is associated to its respective incident angle, which is in turn associated to a particular cycle, forming a total of 4 columns of data to be registered.

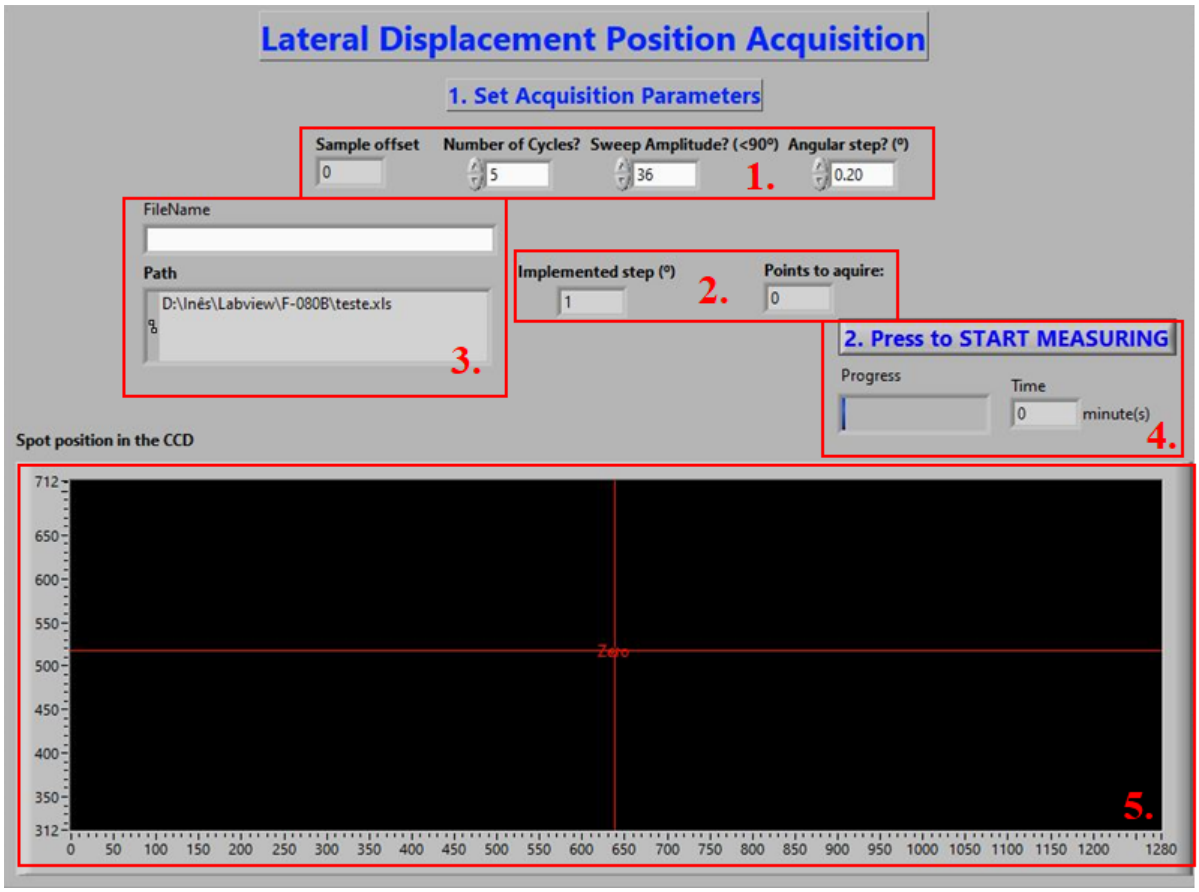

Figure 5.7 – Second page of the front panel of the program in which the user can interact. The user needs to specify three parameters for the measurements, as well as the name of the file that will be created. The spot position can always be monitored, and a progress bar and estimated time left can be viewed.

Table 5-2 – Captions for Figure 5.7. The numbered red squares in the figure are linked to the Number column, and each represents a sub module described in this table.

Number	***Name***	***Description***
1	**Acquisition Parameters**	The user can make changes to the *Number of Cycles*, *Sweep Amplitude* and *Angular Step*. The value of *Sample Offset* is linked to the set alignment offset for the *x* coordinate
2	**Acquisition review**	Based on the information entered in #1, the values of *Implemented Step* and *Points to Acquire* are automatically updated
3	**File**	In *FileName*, the user defines the name of the output file with all the measurements. The path to this file can be viewed in *Path*
4	**Position Acquisition**	By pressing the button to *START MEASURING*, the program begins the automated process to measure the lateral displacement for each angle. A *Progress* bar and estimated *Time* until completion are displayed right below
5	**Spot Position**	Real time tracking of the spot position in the camera

Having set all the parameters, pressing the button (Figure 5.7, number 4) the automated process of lateral displacement measurements. After all the measurements of the *xy* centroid coordinates are made,

the values of lateral displacement with respect to the incident angle are transferred into an excel file and the LabVIEW program automatically stops.

An excel worksheet was developed and implemented in collaboration with the thesis supervisor that made the process of refractive index determination simple and semi-automated. All that is required of the user is to insert the data sheet created by the LabVIEW code and specify the sample's thickness and the worksheet proceeds to calculate the RI value and associated uncertainty. The next subsection describes in greater detail the multiple step process.

5.2 GOLD Data Processing

The processing of the data acquired by the LabVIEW program consists of 5 sweeps (default value) of the glass sample, where for every step the value of the incident angle and spot *xy* pixel coordinates are measured and registered to an output file. As explained in the previous subsection, the user can specify the sweep amplitude and the precision table step – with a small step, more points will be measured (more time will be necessary until completion). Considering that the value of the RI becomes unstable as the incident beam nears the perpendicular position to the sample surface (Figure 5.8, top) more measurements statistically improve the average of the results. For wider angles, the RI measurements are more stable – a greater beam deviation in the sample causes a spot deviation with a decreased standard deviation between the 5 sweeps – so in order to improve the average RI result, only the 25% left/right results were considered (Figure 5.8, bottom).

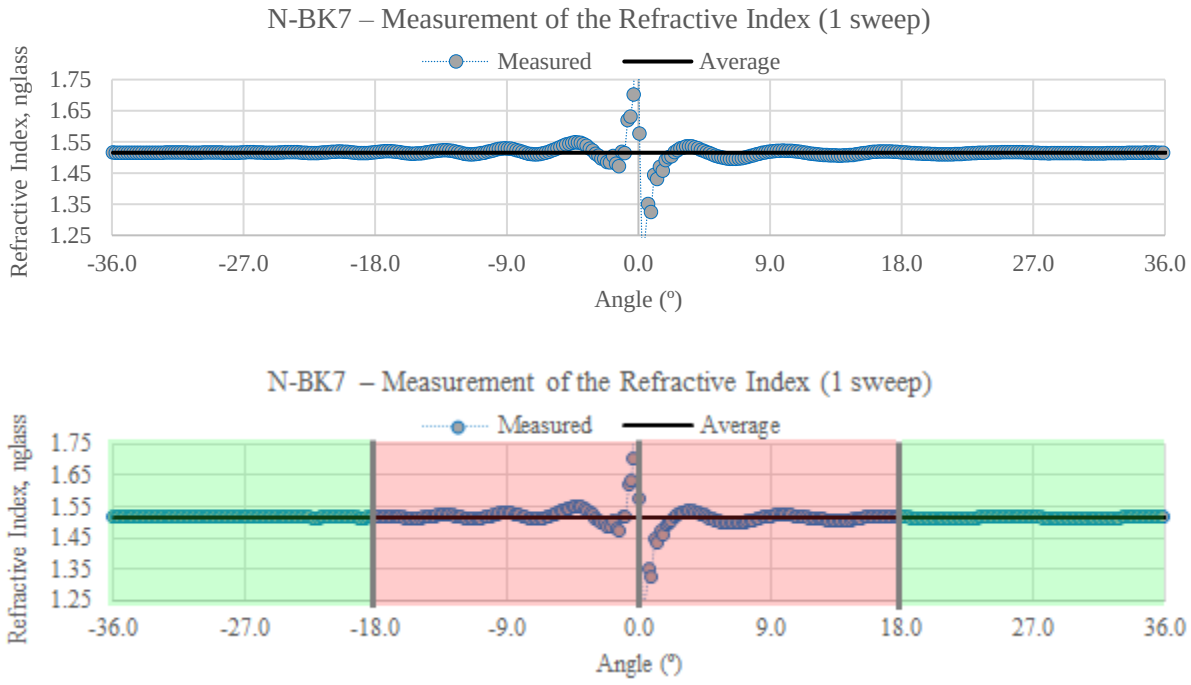

Figure 5.8 – Top: One cycle measurements of the refractive index versus the incident angle, of the calibrated N-BK7 sample. Bottom: Measurements used for the computation of the average n_{glass} value.

A great amount of sample measurements are also especially important if the sample is not of the best quality, which means that the laser spot captured by the camera can be deformed – a good example between high and low quality samples is illustrated in Figure 5.9.

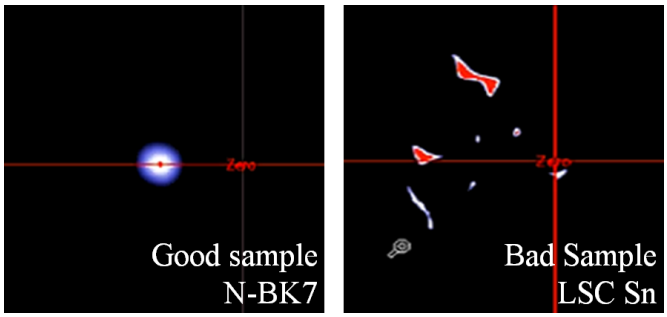

Figure 5.9 – Difference in the shape of the laser spot, captured by the camera, between HQ (left: N-BK7) and LQ (right: LSC Sn) samples.

This type of irregular pattern will also change with the rotation of the sample making the measurements of the lateral displacement erratic, which in turn have disastrous consequences in the results for the refractive index (even for wider angles) – see Figure 5.10.

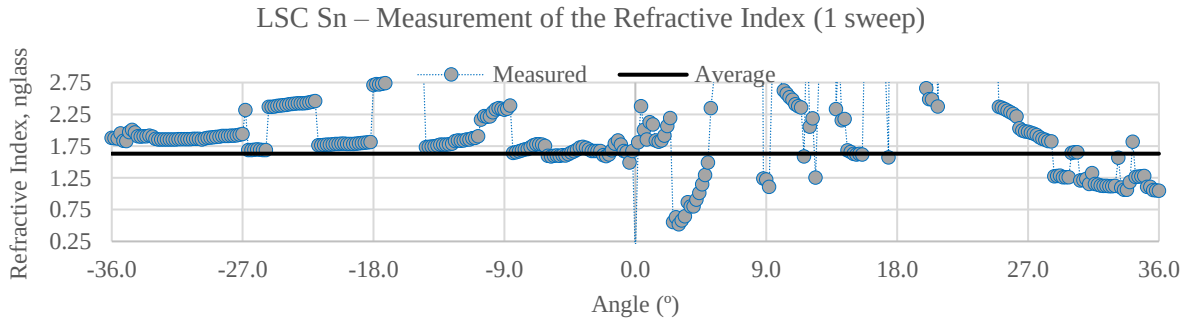

Figure 5.10 – One cycle measurements of the refractive index versus the incident angle, of the LSC Sn sample.

Considering the variability of the results, it becomes advisable to perform an increased number of sweeps and tests to the same sample to minimize similar effect as much as possible. As a general rule ten tests were performed to each sample in Sections 6 and 7 – the user can however define the amount that best suits his/her requirements.

As mentioned before, the measurements obtained from the LabVIEW code are inserted in an excel spreadsheet that performs the necessary operations to obtain the value of the samples refractive index and associated uncertainty value. A simplification of the process can be viewed in Figure 5.11 – in Annex 10.2 more detailed images of the several subsections of the spreadsheet can be seen.

In the first step, the *xy* spot coordinates are transformed to reflect the difference to the position where $\theta_i = 0°$, (x_0 ; y_0) – any deviation is now relative to the position where the beam is perpendicular to the sample surface (x_{rel} ; y_{rel}).

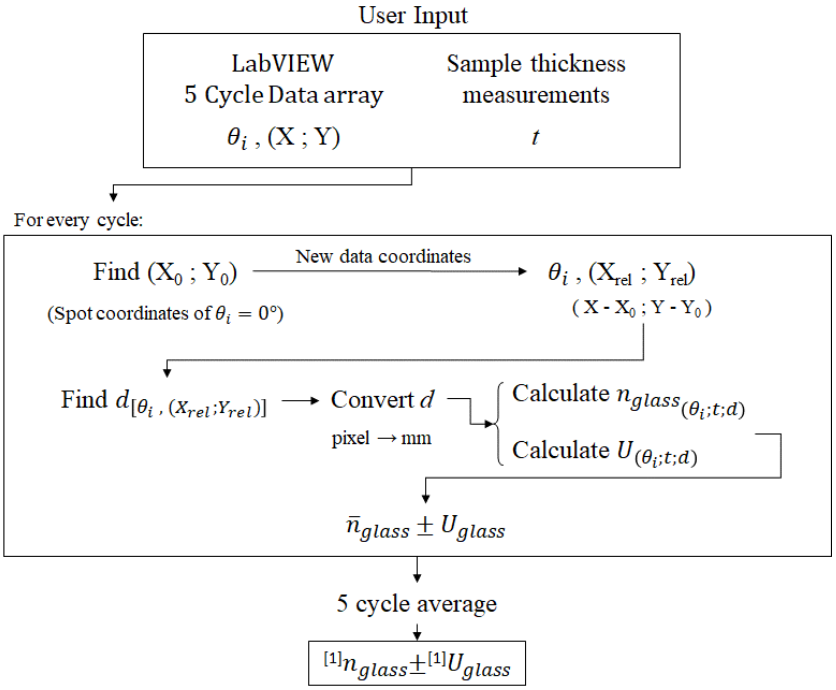

Figure 5.11 – Data processing by the excel spreadsheet, developed to find the value of the refractive index (and associated uncertainty) of a glass sample.

Next, for every angle and pair of spot coordinates, the value of the lateral displacement from the origin (x_0 ; y_0) is calculated geometrically by Equation (5.1. The units of this measurement are converted from pixel to mm, by multiplying the value with the pixel size of the camera (5.3 μm).

$$d_{pix} = \sqrt{{x_{rel}}^2 + {y_{rel}}^2} \tag{5.1}$$

The values of the refractive index according to the incident angle are calculated – as previously stated, although not all are used to find the measurement average, it is still useful to calculate the value for the entire measuring range as it visually helps determine if the sample is adequate and/or if the measurements were performed without incidents (Figure 5.10 – measurements of a LQ sample).

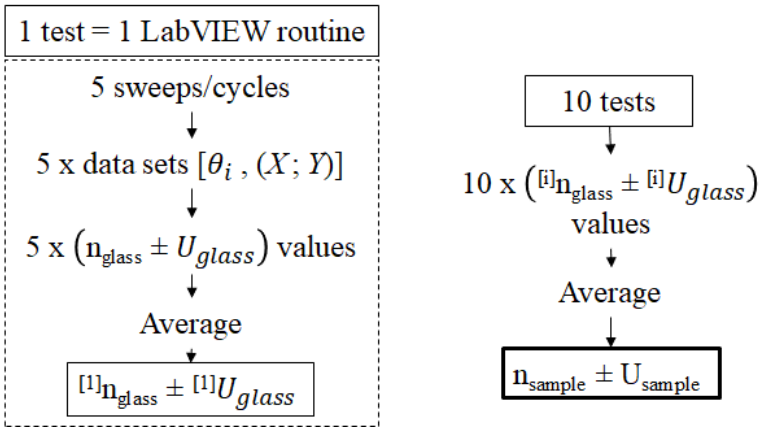

Figure 5.12 – Schematic of the followed procedure to measure the refractive index of a calibrated sample.

Finally, the average value for the refractive index, for this cycle/sweep, is calculated along with the expanded uncertainty – every contribution is accounted for and equality contributes to the final value of the sample's refractive index.

The next chapter discusses the calibration and validation of the system results, by using known glass samples, with well documented properties, as a reference.

6. GOLD System Calibration

The method to determine the refractive index of glass samples was now complete. The next phase aimed to test the quality of the produced results as well as the system's reproducibility and repeatability. To this end, two known samples were used – uncoated, homogeneous and round precision windows from Thorlabs – N-BK7 [26] and UV fused silica (UVFS) [27] whose specifications are well documented.

Borosilicate crown glass (N-BK7) is common in high quality (HQ) optical components, with good transmission (> 90%) in the visible and near infrared regions and a refractive index of (1.5151 ± 0.00005) at a wavelength of 632.8 nm (HeNe) (Sellmeier Equation, provided by Thorlabs, Figure 6.1). The acquired sample thickness is (12.0 ± 0.3) mm, with a surface flatness, on both sides, of λ/10 over the clear aperture.

The second sample, UV Grade Fused Silica, also with a thickness of (12.0 ± 0.3) mm, useful for use in applications in the UV range that goes beyond the transmission of N-BK7, with a refractive index of (1.4570 ± 0.00005) at a wavelength of 632.8 nm (HeNe) (Sellmeier Equation, also provided by Thorlabs) and a flatness, on both sides, of λ/10 over the clear aperture.

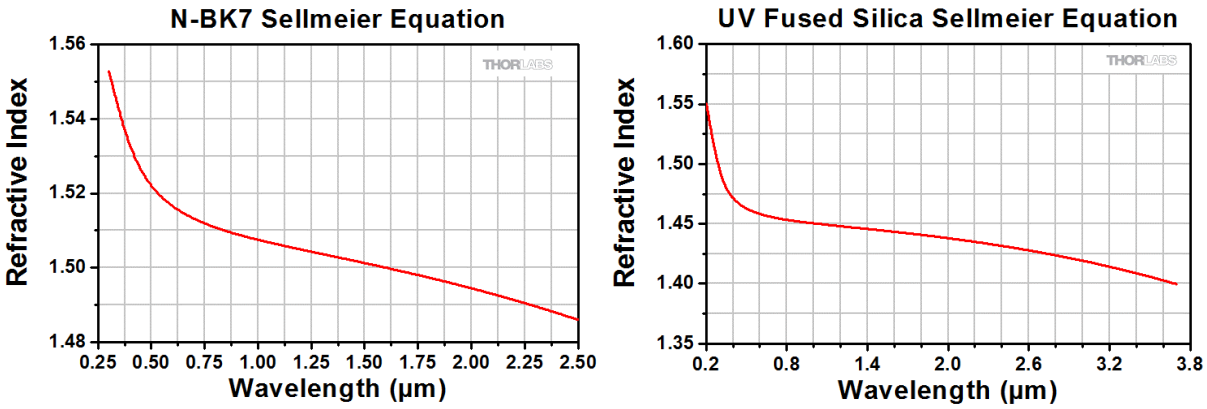

Figure 6.1 – Refractive index data related to uncoated N-BK7 (left) and UVFS (right) precision windows [credit:Thorlabs].

The refractive index of a sample is known to vary with the temperature, however, in both cases, the variation in the index value is in the order of 10^{-6}/ºC, for temperatures between 20 ºC to 40 ºC (according to Thorlabs optical substrate information, available in their website). Temperature fluctuations and how they could affect the system were not considered, and so the N-BK7 and UVFS refractive indexes were constant and at a temperature of 20ºC.

Figure 6.2 – Calibration samples used to validate system results, UVFS (left) and N-BK7 (right).

Both samples had a round shape and were fitted securely by the hook lock of the sample holder in every performed test; all the measurements made to the samples were therefore in the same area. Each test performed by LabVIEW, measuring the lateral displacement associated to each incident angle, was standardized to execute five consecutive sweeps, from -36º to 36º and in steps of 0.2º. To test the repeatability, for every concluded set of sweeps, the sample was removed, reintroduced in the sample holder and realigned – although, as explained, because the samples fit perfectly into the sample holder, the alignment adjustments didn't differ much from each other.

Each five-sweep test had the duration of about one hour and a total of ten tests were made to each sample, which translates to 50 different data sets. Every test results in one independent value of the refractive index (five sweeps are performed under the same conditions), ten values for the sample RI are obtained from ten tests and the resulting average corresponds to the systems measured value of the sample's refractive index.

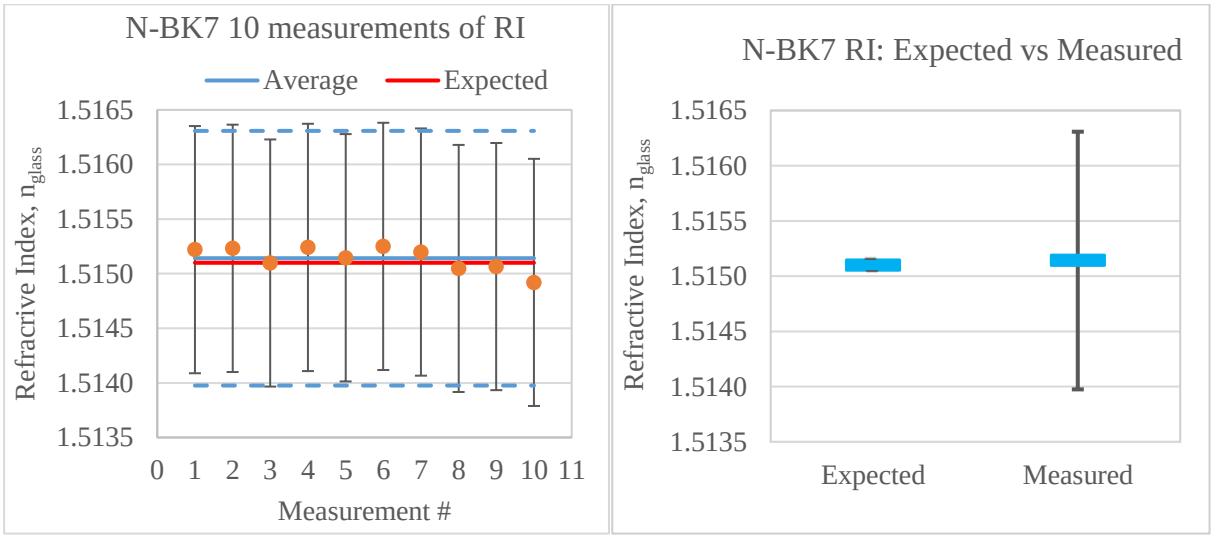

Figure 6.3 – Left: 10 measurements (orange dots) and associated individual uncertainty (black bars) of the refractive index of N-BK7and their comparison with the resulting average and uncertainty (blue solid line and blue dashed lines, respectively) and known expected value (red). Right: Comparison between the 10 value average (Measured) and the known value (Expected) for the refractive index of the N-BK7 precision window.

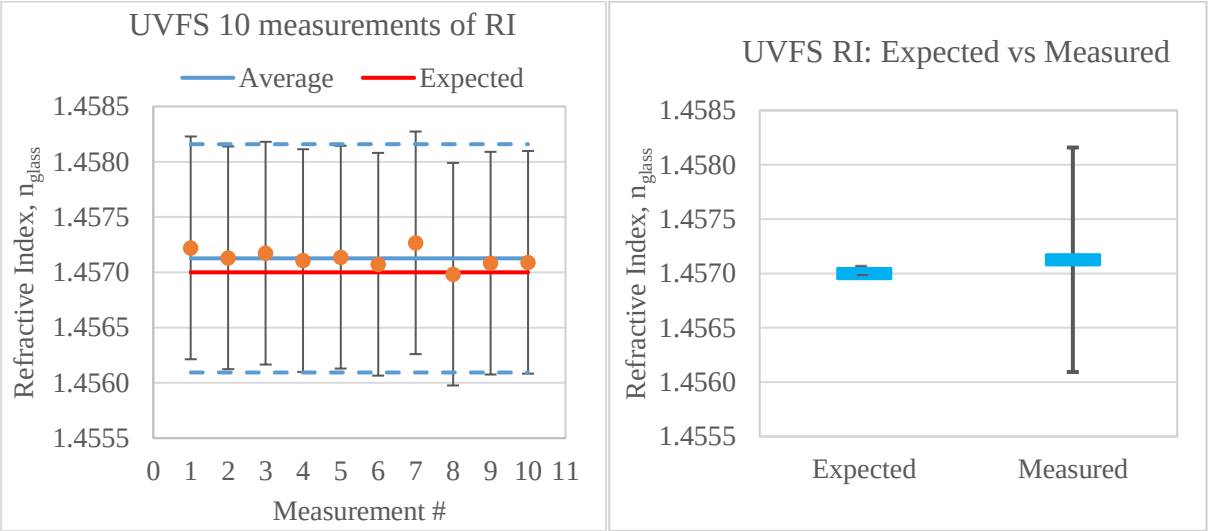

Figure 6.4 – Left: 10 measurements (orange dots) and associated individual uncertainty (black bars) of the refractive index of UVFS and their comparison with the resulting average and uncertainty (blue solid line and blue dashed lines, respectively) and known expected value (red). Right: Comparison between the 10 value average (Measured) and the known value (Expected) for the refractive index of the UVFS precision window.

Table 6-1 – System results for the measurement of the refractive index of the two calibrated glass precision windows from Thorlabs, N-BK7 and UVFS, for a coverage level $k = 2$ and a confidence level of 95%.

Sample	Expected RI	± U	Measured RI	± U	U (%)	| Error | (%)
N-BK7	1.5151	± 0.00005	1.5151	± 0.0012	0.08	< 0.01
UVFS	1.4570	± 0.00005	1.4571	± 0.0010	0.07	0.01

From Table 6-1, it can now be concluded that the system can achieve the objectives set by this thesis, that is, the achievement of results with an uncertainty below 10^{-2} (or 1%), 10^{-4} (or 0.01%) for these calibrating samples. But not all samples are expected to be of such high quality, in fact, due to the experimental nature in the manufacturing process of Luminescent Solar Concentrators, different luminescent substrates can be used, which can influence the quality of the sample and its efficiency as a concentrator [28].

The next section is dedicated to the analysis of the samples provided by VICARTE as well as three additional samples provided by the optics lab – the value of the refractive index for the latter three was withheld and only revealed at the end of the measurement and analysis procedures.

7. Measurement of unknown samples

With the good results obtained with the calibrating samples, it was now time to test samples without any prior knowledge of their properties and value of the refractive index, to ensure that the system and data processing were adequate for any optically simple glass sample.

First, three samples available in the lab were used – one sample, believed to be also Fused Silica glass (very similar to the UVFS sample), another later revealed as a B270 glass sample and a piece of a common transparent acrylic block. Subjecting these samples to analysis was important in the consolidation of the system/method to be applicable to the LSC samples – it provided, above all else, further reassurance of its good results and suitability. As will be shown in the LSC subsection, not all samples were adequate because of its shape and/or internal atypical morphology (associated with the manufacturing processes of the glass itself).

7.1 Unknown Lab Samples

The first samples to be analysed, due to their better overall condition as optical samples were the Fused Silica and the B270 samples in Figure 7.1. Although the fused silica sample presented some deterioration/chipping in its edges, since it was also circular, when placed in the sample holder the measurements were always in the same area (identical to the calibration samples) – the sample damage had no effect in the results.

The sample later identified as B270 has many useful applications in the consumer and optics industry due to its high transmission across a wide spectrum and homogeneous value of the refractive index, for example. This sample presented a challenge however – due to its square shape and approximately 5 mm thickness it was difficult to secure it in the sample holder (similar problem already described in Figure 4.13, Section 4.4).

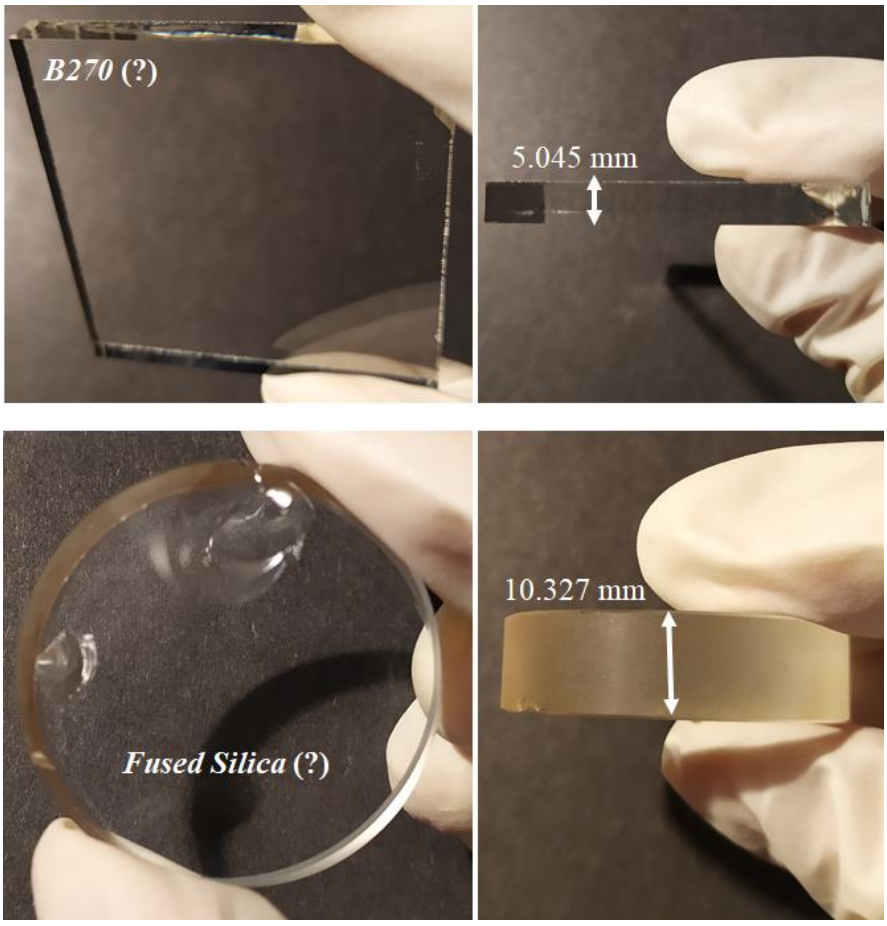

Figure 7.1 – Unknown tested samples, later identified as B270 glass (a) and Fused Silica (b). Sample surface (left) and sample thickness (right).

Additionally, because of its squared shape, every test was performed on a slightly different area of the sample surface (see Figure 7.2, b); in these specific cases however, through visual inspection and considering that the samples were provided by the optics laboratory, the homogeneity of the samples was discarded as a source of uncertainty (that was not the case with every LSC sample, as will be discussed further on).

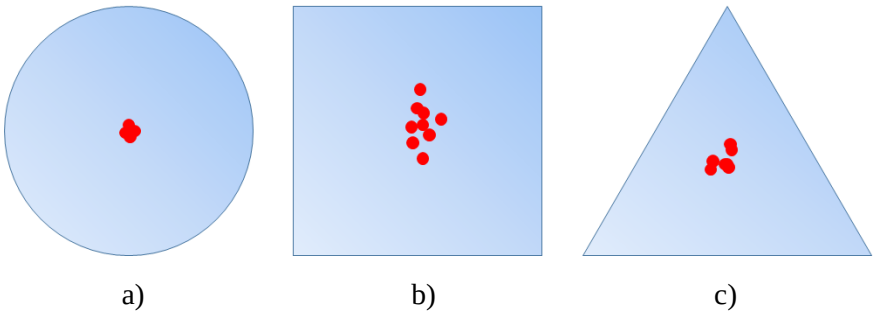

Figure 7.2 – Tested surface area of samples (red dots representing the laser beam position) according to its shape and compatibility with the sample holder.

Ten tests were made to each sample, following the same procedure described at the end of Section 6, which comprised of five sweeps each, measuring the lateral displacement associated to each incident angle from -36º to 36º and in steps of 0.2º – after every test, the sample was removed, reintroduced in the sample holder and realigned. The results are displayed in Figure 7.3.

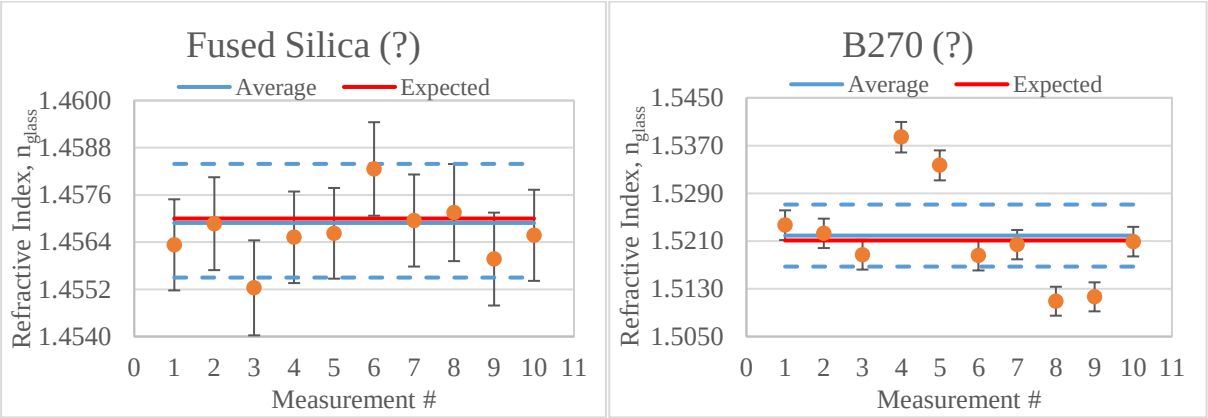

Figure 7.3 – Ten measurements of the samples Fused Silica (?) (left) and B270 (?) (right) refractive index (orange) with associated individual uncertainty (black bars). The resulting average and uncertainty (blue line solid and dashed, respectively) are compared to the known expected value for the RI (red line).

As expected, the results in both samples became more disperse (when compared with the ones obtained with the calibrating samples). The Fused Silica sample has no outliers and an error of 0.01% to the expected value, (1.4570 @ 632.8 nm wavelenght), was obtained with a measurement accuracy of 10^{-3} (or 0.10%) as displayed in Table 7-1. The B270 sample presents a greater dispersion in the values – measurements 4,5,8 and 9 could be considered outliers when comparing their value to the global average; this discrepancy can be strongly associated to the bad compatibility of the sample with the sample holder and/or bad alignment. However, by performing ten tests, the average of the results comes very close to the expected value (1.5211 @ 632.8 nm wavelenght [29]), with an error of 0.05% and measurement accuracy also in the range of 10^{-3} (0.34%) (see Table 7-1).

The same procedure was applied to the triangular acrylic block depicted in Figure 7.4 and although not visible in the image, the sample surface was covered with small scratches – this sample was not intended for precision optics. It was nevertheless interesting to study the performance of the system; no information was known about this sample, and the best guess of its composition was as a type of acrylic named PMMA Poly(methyl methacrylate) – also known as Plexiglas, Perspex, Lucite, among others – a common thermoplastic polymer material with many applications [30].

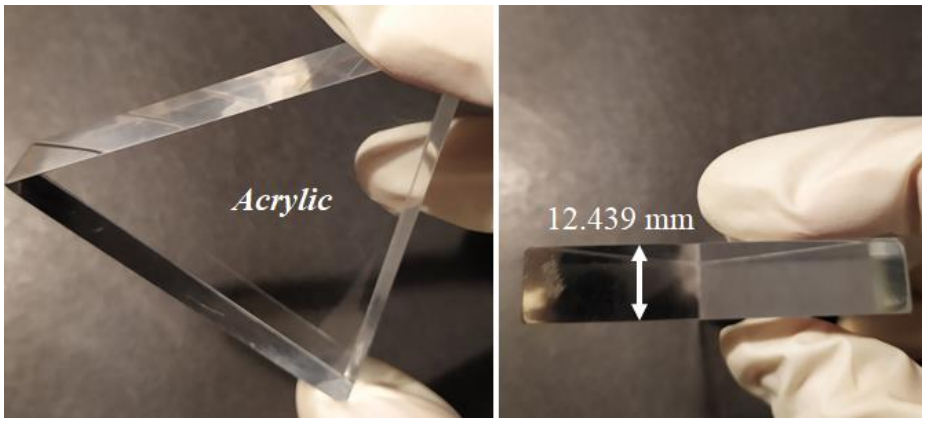

Figure 7.4 – Tested acrylic sample with unknown refractive index. Sample surface (left) and sample thickness (right).

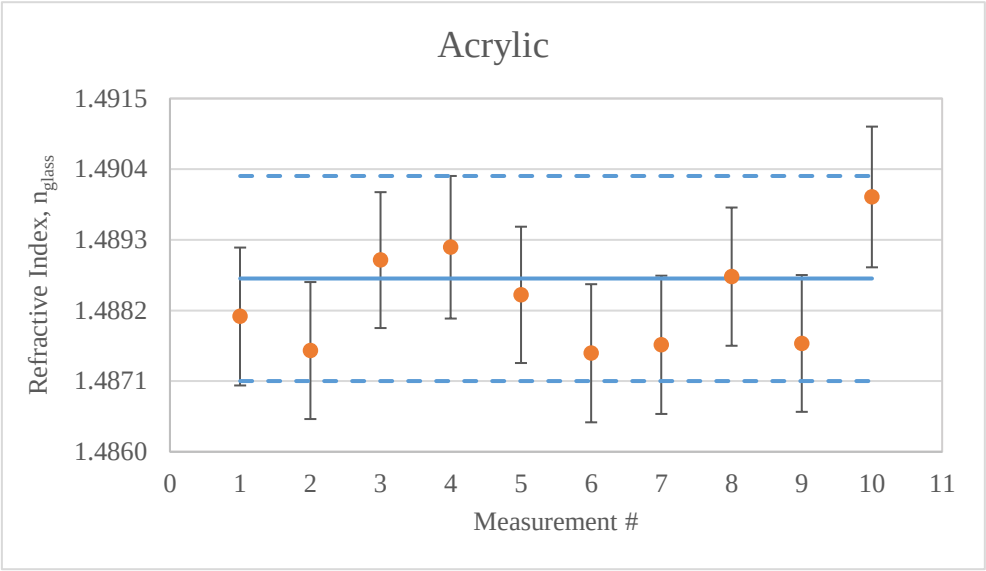

Figure 7.5 – Ten measurements of acrylic refractive index of the acrylic sample (orange) with associated individual uncertainty (black bars). The resulting average and uncertainty are depicted by blue lines: solid and dashed, respectively.

Similar to the fused silica sample, some dispersion in the results was verified but the average of the results is identical to the expected value (1.489 @ 632.8 nm [31]), with an error of 0.02% and measurement accuracy in the range of 10^{-3} (0.11%).

Table 7-1 – System results for the measurement of the refractive index of the three unknown lab samples, Fused Silica, B270 and Acrylic, for a coverage level $k = 2$ and a confidence level of 95%.

Sample	Expected RI	Measured RI	± U	U (%)	| Error | (%)
Fused Silica	1.4570	1.4569	± 0.0015	0.10	0.01
B270	1.5211	1.5219	± 0.0052	0.34	0.05
Acrylic	1.4890	1.4887	± 0.0016	0.11	0.02

The summary of the results for these three samples is on Table 7-1. All the results are within the acceptable parameters set for this thesis (accuracy better than 1%) and measurements of the refractive index of unknown LSC samples can begin with complete confidence in the system and employed method.

7.2 LSC Samples

In the particular case study of LSC glasses, in order to assess its viability in becoming a renewable energy source, the efficiency of solar energy conversion, through the trapping of light by total internal reflection (TIR), demonstrated in Figure 7.6, must be analysed.

$$\theta_C = arcsin(n_2/n_1) \tag{7.1}$$

As the angle of incidence θ_1 increases, the angle of refraction θ_2 increases until θ_2 is 90° (critical angle θ_C) – for even larger angles of incidence, total internal reflection occurs.

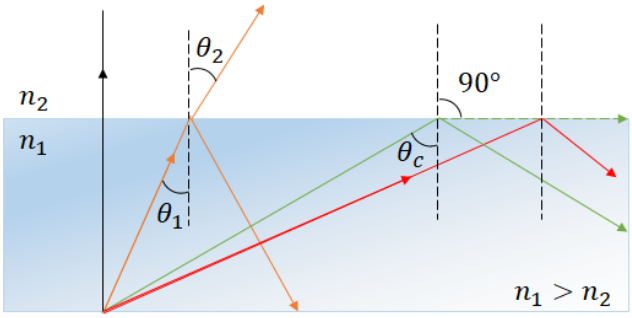

Figure 7.6 – Total internal reflection of a beam.

The TIR angle is directly related to the refractive index of the glass [3] – refraction techniques, for example, study the displacement of the beam that crosses a glass sample, determining the refractive index of the sample.

LSC glass absorbs sunlight and emits radiation at a given wavelength, which is directed through TIR for photovoltaic cells at the borders of the LSC [28]. These LSC can be transparent inorganic glasses, which have intrinsically high durability and are synthesized from widely available resources. With these characteristics they can be used as windows in which photovoltaic cells can be integrated, allowing the capture of solar energy. It is fundamental to be able to produce Luminescent Solar Concentrators using economical raw materials and through low complexity/cost characterization processes.

The efficiency of producing solar energy through a window made of LSC glass has a strong dependence associated with the radiation captured by the photovoltaic cell. The radiation captured, in turn, depends on the angle from which the radiation produced by luminescence is reflected by the inner faces of the glass plate (due to TIR) until reaching the cell and being absorbed. Considering a glass plate of thickness *t*, the distance at which conversion of luminescence incident light into the glass takes place can be calculated simply by knowing the refractive index of the LSC glass. The values for the RI of this type of material will depend not only on the entire manufacturing process, but also on the non-negligible variations between two different batches of identical glass.

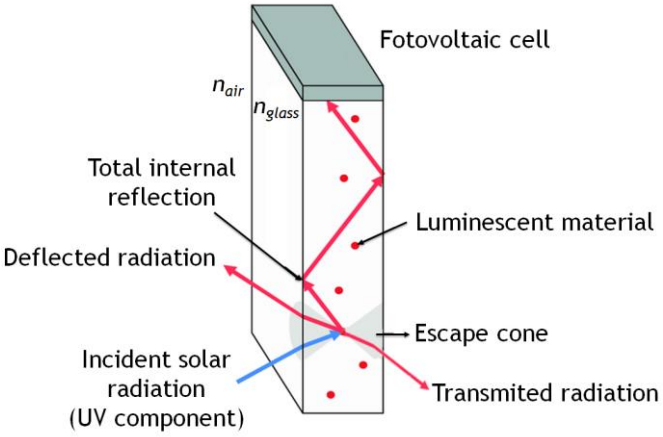

Figure 7.7 – Basic principles of using LSC glass to produce solar energy.

The quality of the surface of the samples, which depends on the manufacturing process, is also a factor influencing the results obtained, but since these are samples will be applied as windows and not in optical systems, it is not necessary to demand a higher quality.

The VICARTE research centre has at its disposal techniques that allow the manufacture of LSC glasses and has kindly provided seven different samples to be analysed by the GOLD system developed by this thesis. All samples had been labelled by VICARTE, some with a probable reference to the type of dopant used (for example, Figure 7.12), but no other type of information regarding their composition and/or characteristics was provided – it was assumed that all seven samples were different, and therefore would have a different value of the RI.

Sample Homogeneity

Upon visual inspection, it was possible to notice that some samples were in a low quality state: chipped (Figure 7.12, LSC Sn) and/or not homogeneous inside – a clear example of the latter is shown in Figure 7.8. Surface abrasion on the extremities does not usually affect the measurements since the laser beam always crosses the centre area of the sample (because of the used sample holder), but if the sample contains too many impurities (Figure 7.8) inside and/or is not, the measurements of the lateral displacement are going to be affected.

Different types of inhomogeneities can be found in a glass block [32], originated along the manufacturing process. These anomalies which cause scattering of the wavefront that traverses the sample, affect the value of the RI – spatially (striae, inclusions, bubbles) and directionally (stress birefringence).

For this reason, two of the seven provided samples were not analysed – LSC Eu and LSC Cu – because they displayed a too many anomalies, like bubbles for example, that caused a high scattering of the laser beam and produced low quality spot images. When placed in the system, a rotation of any degree produced a different irregular spot whose centroid coordinates were difficult to determine (as illustrated in the comparison between a HQ and LQ sample made in Figure 5.9 in Section 5.2).

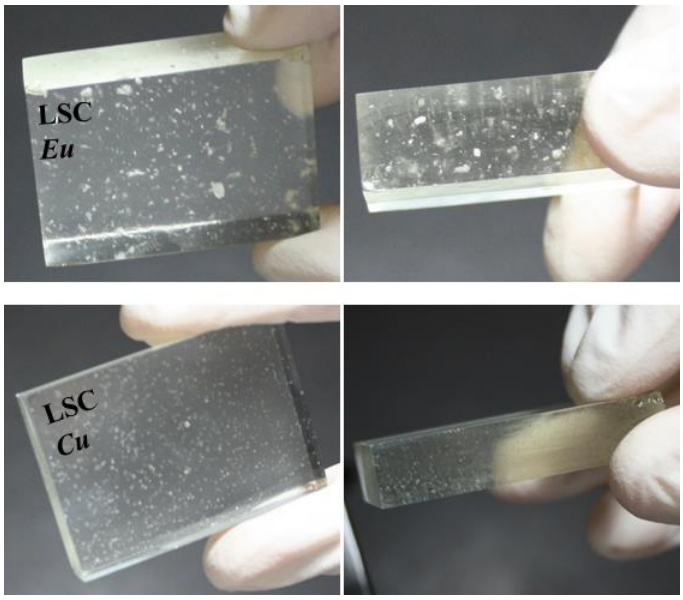

Figure 7.8 – Untested LSC samples: LSC Eu (a) and LSC Cu (b), sample surface (left) and sample thickness (right).

Of the five remaining samples, only two displayed qualities that can be associated to the production of good results and acceptable accuracy values – LSC Vidro de Janela and LSC Branco Vidro Float (Figure 7.9) – samples with no visible impurities and no apparent inhomogeneities, glass with clear transparency and smooth, damage free edges.

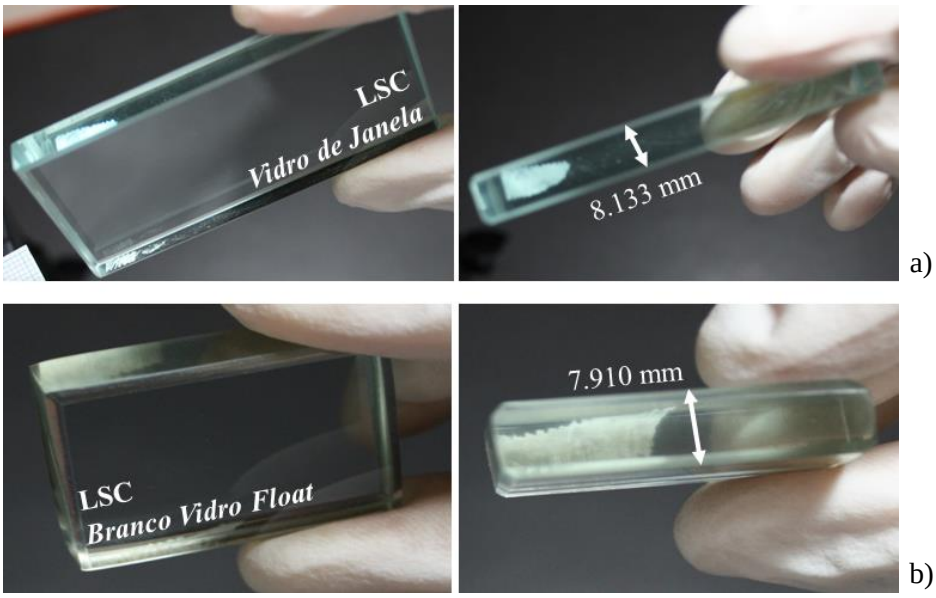

Figure 7.9 – Tested LSC samples, LSC Vidro de Janela (a) and LSC Branco Vidro Float (b), with consistent value results of its refractive index. Sample surface (left) and sample thickness (right).

Considering high quality of the sample, only five tests were made to each sample and the results can be viewed in Figure 7.10. Some dispersion is present, although small (a span of about 0.005 in the values for the RI), due to the analysis made in Section 7.1, the results were considered valid and with an

associated accuracy of 0.15 % and 0.14 % for LSC Vidro de Janela and LSC Branco Vidro Float respectively (see Table 7-2).

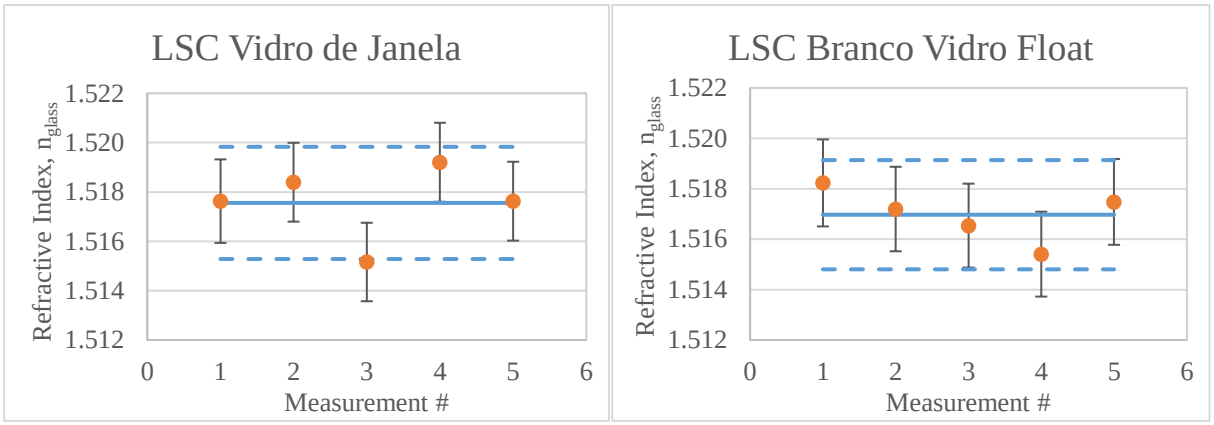

Figure 7.10 – Five measurements of the samples LSC Vidro de Janela (left) and LSC Branco Vidro Float (right) refractive index (orange) with associated individual uncertainty (black bars). The resulting average and uncertainty are depicted by blue lines: solid and dashed, respectively.

The average value of both samples, (1.518 ± 0.002) for LSC Vidro de Janela and (1.517 ± 0.002) for LSC Branco Vidro Float could suggest that the samples have a material similar composition (in Figure 7.11, both results and respective averages/uncertainties are displayed in the same graphic). However, with no more information other than the name of each sample, based only the measurements made by the GOLD system, this claim can only be considered as an hypothesis.

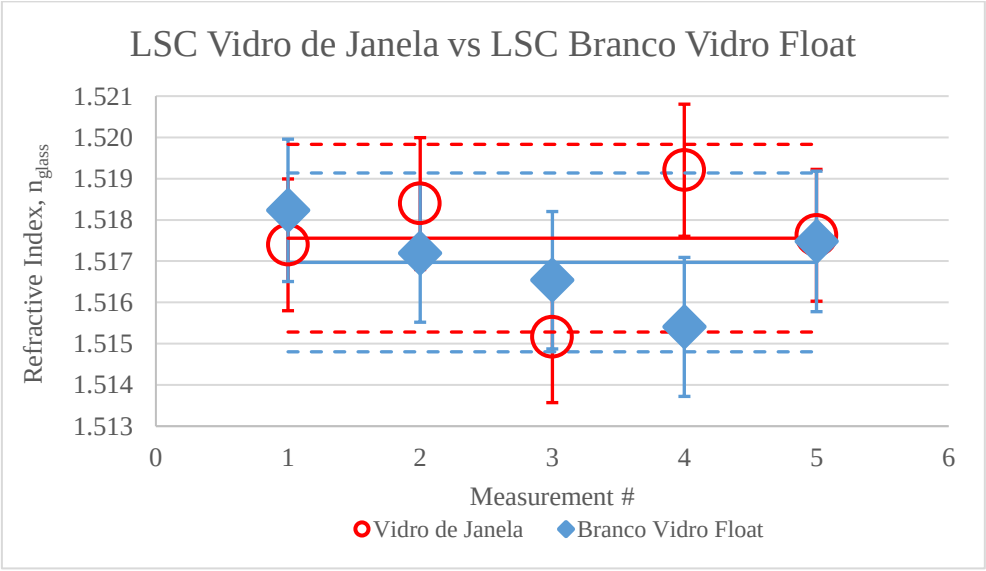

Figure 7.11 – Results comparison between LSC samples Vidro de Janela (red circles and red uncertainty bars) and Branco Vidro Float (blue squares and blue uncertainty bars). Both sample result averages are represented by solid lines and associated uncertainty intervals in dashed lines (with the same colours).

The remaining three LSC samples were in a comparatively worse condition; as depicted by Figure 7.12, the LSC Sn sample had damaged edges, as well as some surfaces scratches, both this and the LSC

Sample52 Mn displayed a dull surface and, more accentuated in LSC Sample40 Mn, some inhomogeneities were observed (b, right), as well as small bubbles (a side effect of the manufacturing process, and with consequences for the accuracy of measurements identical to impurities). Nevertheless, these three samples were subjected to ten tests each – they served as a worst-case scenario study, where the limitations of LQ samples could be evidently reflected in the decrease (and by how much?) of the accuracy of the measurements.

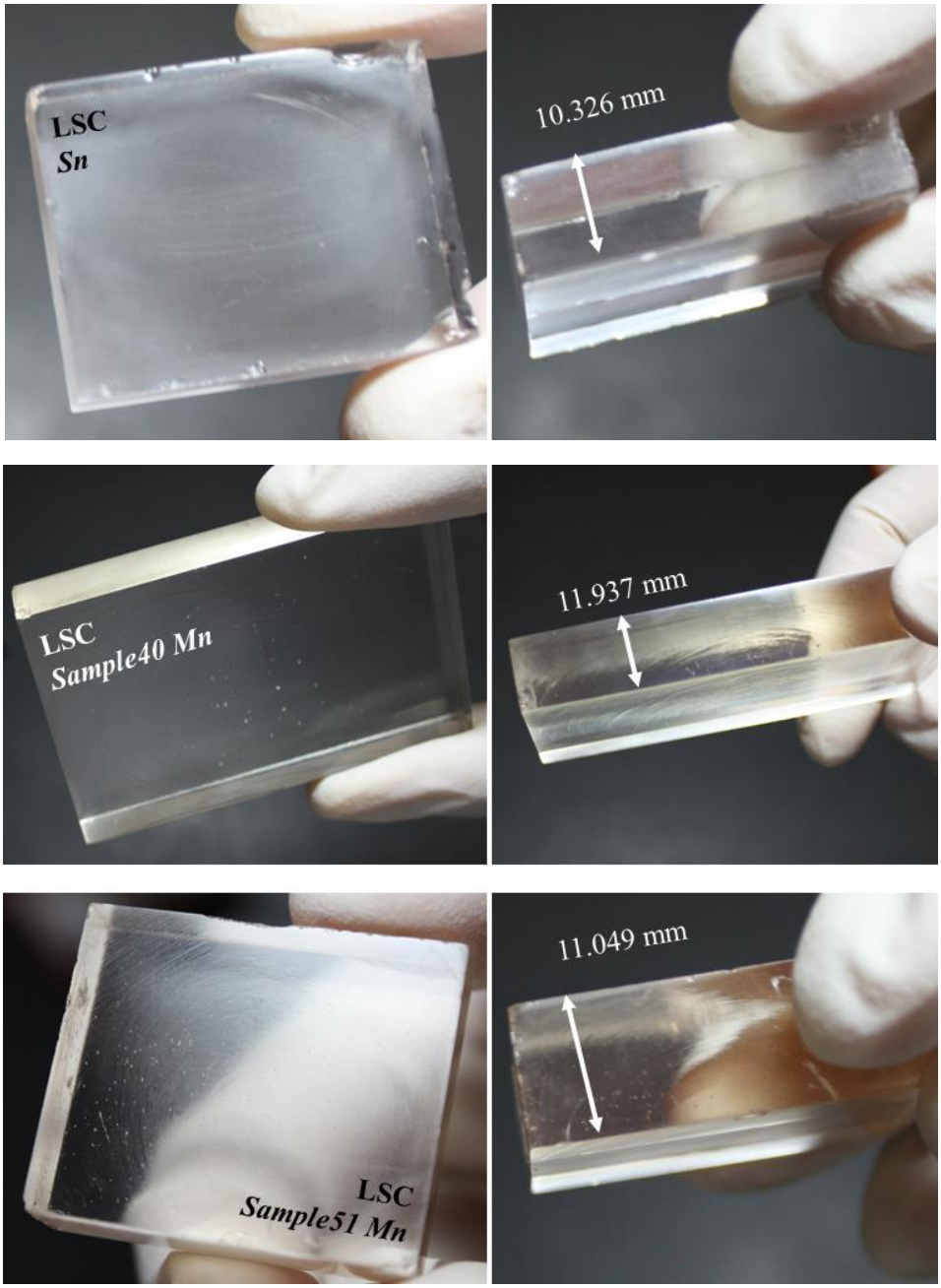

Figure 7.12 – Tested LSC samples, from top to bottom LSC Sn, LSC Sample51 Mn and LSC Sample40 Mn, with more inconsistent value results of its refractive index. Sample surface (left) and sample thickness (right).

For the LSC Sn sample only five tests were performed, due to the already mentioned LQ condition of the sample – the value of its refractive index was (1.580 ± 0.038), which corresponds to an accuracy

of about 2.4%, a value above the required 1% limit for the measurement's accuracy. Nevertheless, considering the quality of the sample this obtained value was regarded as a close guess to the value of the sample's RI.

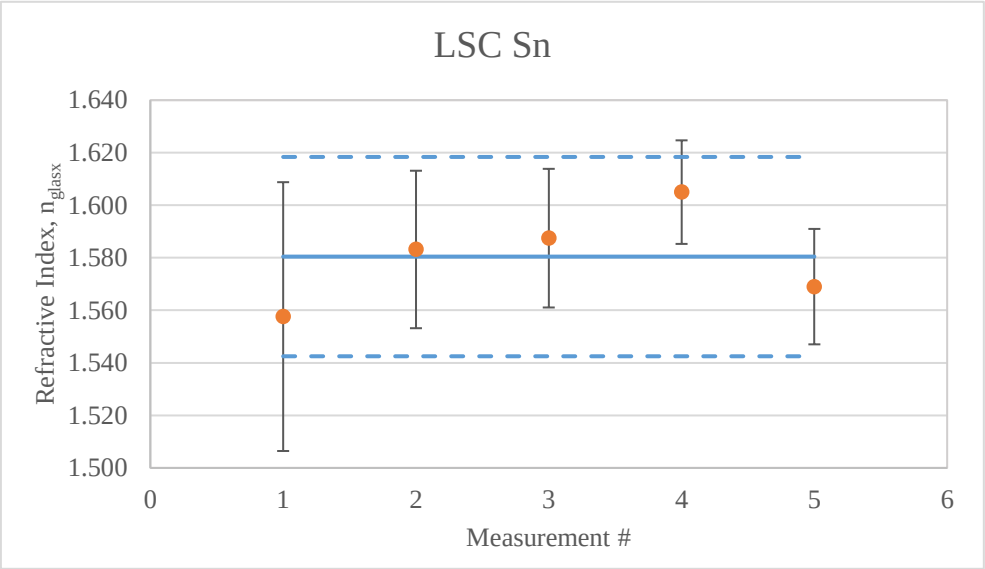

Figure 7.13 – Five measurements of the sample LSC Sn refractive index (orange) with associated individual uncertainty (black bars). The resulting average and uncertainty are depicted by blue lines: solid and dashed, respectively.

Next, the remaining LSC samples were subjected to ten tests each (even though both were also LQ samples to be tested by this method) in order to test out an hypothesis: Both sample names suggest that they contain the same luminescent dopant Mn (Manganese) so it could mean that the values of their refractive indexes could be similar, assuming the conditions that the dopant concentrations are identical, for example.

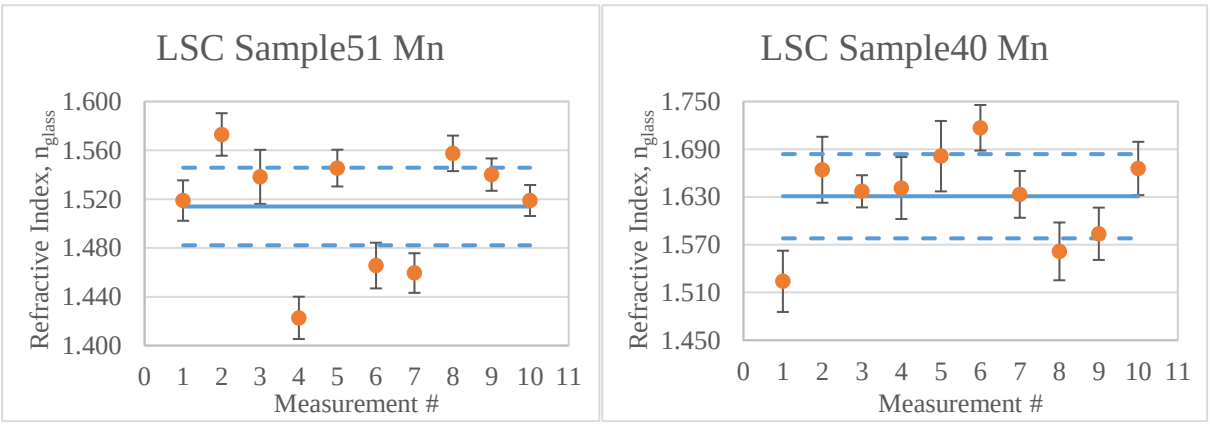

Figure 7.14 – Ten measurements of the samples LSC Sample51 Mn (left) and LSC Sample40 Mn (right) refractive index (orange) with associated individual uncertainty (black bars). The resulting average and uncertainty are depicted by blue lines: solid and dashed, respectively.

The results from LSC Sample51 Mn mainly reflect the LQ sample condition, allied to the inadequacy of the sample holder with square samples. Associated to these circumstances, both present

outliers, and the obtained average for the refractive index was (1.514 ± 0.032) and (1.631 ± 0.053) for LSC Sample51 Mn and LSC Sample40 Mn respectively, which correspond to accuracy values of 2.1% and 3.3%, both above the 1% imposed limit. In Figure 7.15, the measurements of both samples are represented in the same graphic, to better compare both values and test the hypothesis of sample similarity.

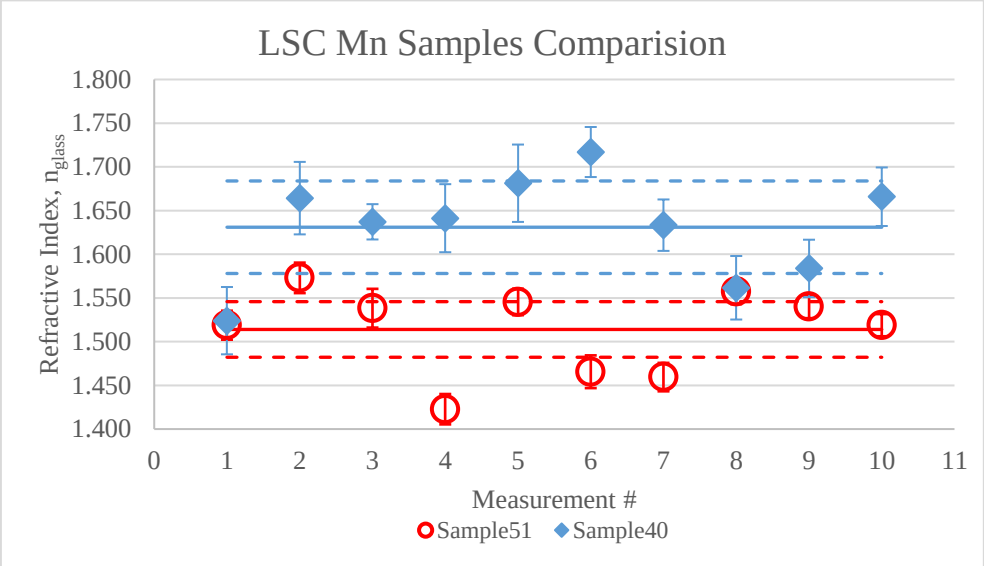

Figure 7.15 – Results comparison between LSC samples Sample51 Mn (red circles and red uncertainty bars) and Sample40 Mn (blue squares and blue uncertainty bars). Both sample result averages are represented by solid lines and associated uncertainty intervals in dashed lines (with the same colours).

As illustrated in the figure above, the average value of the refractive index is so different that no relevant overlapping of the results occurs (measurements #1 and #8 of LSC Sample40 Mn are considered outliers). This clear differentiation of results by the GOLD system strongly suggests that despite the similarities in the name, the composition is not similar – further conclusions about the relation between these samples cannot be drawn solely by using this method.

Testing this was interesting to assess the viability of the system as a sample comparator – further, more extensive studies should be made however, with proper optical samples, before its adequacy for this type of purpose can be established.

Table 7-2 – System results for the measurement of the refractive index of the five viable LSC samples: LSC Vidro de Janela, LSC Branco Vidro Float, LSC Sn, LSC Sample40 Mn and LSC Sample51 Mn, for a coverage level $k = 2$ and a confidence level of 95%.

Sample	Measured RI	± U	U (%)
LSC Vidro de Janela	1.518	± 0.002	0.15
LSC Branco Vidro Float	1.517	± 0.002	0.14
LSC Sn	1.580	± 0.038	2.4
LSC Sample40 Mn	1.631	± 0.053	3.3
LSC Sample51 Mn	1.514	± 0.032	2.1

Finally, Table 7-2 summarizes the results of the five analysed LSC samples. Considering the major quality difference between samples LSC Vidro de Janela, LSC Branco Vidro Float and LSC Sn, LCS Sample40 Mn and LSC Sample51 Mn, the system performance exceeded expectations, particularly regarding the latter three samples. Indeed, even for samples with such poor structural quality the accuracy of the results was always below 5% (in the order of 0.1% for the HQ samples), which again attests the sturdiness of the method.

In conjunction with the obtained results in Section 7.1, enough confidence in the system exists to state that the developed system is working and has achieved its purpose of producing measurements of the refractive index, for optically simple, parallel plated glass samples, with an associated uncertainty in the order of 0.1% (or 10^{-3}), better than the 1% (or 10^{-2}) that was initially requested.

8. Conclusions and future work

The goal of the present thesis was the development of a system capable of measuring the refractive index of glass samples, focusing in the optimization/refinement and improvement of a known concept, refining it for everyday use for a lab environment. A study of the state of the art was conducted and of the several techniques available, a comparison between obtained uncertainty, quantitative complexity and possibility of optimization was evaluated – both lateral displacement and interferometric methods were potential candidates.

Since both methods provided theoretical (modelled) results with an accuracy below 10^{-2}, it was decided to make a preliminary theoretical study, as well as the weight of each parameter in the accuracy, of the results obtained by both methods. Since, in theory, both methods were viable, a setup was designed that enabled the test of each method, in similar conditions – according to the data acquired by the theoretical studies, the interferometric method was expected to provide the better results. However, through experimental observations it was discovered that an interference pattern was present in both methods and could not be entirely mitigated – this pattern proved critical in the interferometric method and so the lateral displacement method was chosen to implement in the system to develop.

With the selected method, a new setup was constructed and new studies were made, mainly regarding the individual contribution of every main parameter to the measurement uncertainty of the refractive index of glass samples. It was discovered that the measurement of the lateral displacement made by the 2D sensor dominated the uncertainty in the RI measurements, so an additional study of the impact of the interference pattern in the spot measurements was conducted. There was also a concern regarding the existence of a wedge in the sample and its effect in the results – Zemax simulations were made and the effect was consequently safely discarded.

Having characterized the behaviour of the system in depth, a LabVIEW code was developed and employed to control the equipment and register results automatically. The program was used to change camera and image parameters, spot alignment and multiple continuous measurements of the lateral shift d with respect to the incident angle θ_i, which are then exported to an excel file. This acquired data is then inserted in an excel worksheet which outputs the value of the refractive index of the sample, as well as its associated uncertainty and error.

The system has been thoroughly tested – two calibrated glass samples N-BK7 and UVFS, with known refractive indexes, validated the method and the obtained results have an uncertainty of 0.07% and 0.08% (or 10^{-4}), respectively, and errors of about 0.01% (Table 6-1). These excellent results permitted further testing by using unknown samples. First, three samples from the lab were tested: Fused Silica, B270 and Acrylic, having obtained an uncertainty of 0.10%, 0.34% and 0.11% (or 10^{-3}), respectively, and all with errors below 0.05% (Table 7-1). Last but not least, five of the seven LSC samples provided by VICARTE were analysed (Table 7-2) and two groups were distinguished – HQ and LQ samples. From high quality samples, LSC Vidro de Janela and LSC Branco Vidro Float, the results were obtained with an uncertainty of 0.15% and 0.14% (or 10^{-3}), respectively. Low quality samples, LSC Sn, LSC Sample40 Mn and LSC Sample40 Mn provided results with an uncertainty of 2.4%, 3.3% and 2.1% (or 10^{-2}), respectively.

The general good results, even with samples with visible damage and that are not homogenous, attests to the robustness of the built system – due to the detailed analysis and optimization and to the fact that some uncertainties were overestimated (to ensure the safety of obtained results).

The system works and is ready to be exploited in the lab, but improvements can also be made. The following upgrades can be implemented without requiring much effort and with no significant increase to the system complexity:

- Replacement of the sample holder.
  With an adequate sample holder, some samples repeatability/reproducibility can be improved.
- Full implementation of measurements by LabVIEW.
  Although it doesn't affect system performance, it enables results to be obtained with the press of a button (valuable and time saving if bulk analysis are made to many samples).
- Use of an incoherent light source.

The latter improvement may be the one with the most impact in the performance of the system. The biggest disadvantage of using this type of source is the much bigger size of the spot (compared to the one produced by the laser) which reduces the useful area of the sensor. This setback can be circumvented with the use of a diaphragm to reduce the diameter of the spot until it is similar to that produced by the laser or by attaching a fiber and using a collimator. An incoherent light source significantly reduces the effects caused by the interference patterns, therefore its use could make improvements in the uncertainty of the *xy* position – one of the sources with most weight in the global uncertainty – as well as the fact that multiple wavelengths could easily be implemented, increasing the range of applications.

As a final remark, the work developed in this thesis was gradually reported to the scientific community in the form of oral presentations and articles. The earliest, at the *IV International Conference on Applications of Optics and Photonics* in June 2019, was the showcase of a poster highlighting the conclusions of the trade-off between the two candidate techniques and the publication of an article in the Proceedings volume of the conference [33] (see Annex 10.3). The study of the 2D sensor camera was developed as part of an awarded grant – Bolsa de Iniciação Científica (IA2019-03-BIC) – by the Instituto de Astrofísica e Ciências do Espaço (IA) in the context of the project UID/FIS/04434/2019. Final results were also reported at the 2020 *Encontro Nacional de Estudantes de Física* (ENEF) in the form of an oral presentation which was awarded with the first prize in the *Student Lectures Competition*. At the time of writing, another article is being prepared to be submitted in SPIE's *Optical Engineering* journal, showcasing the finished system and full results.

9. Bibliography

[1] S. Singh, “Refractive Index and Its Applications,” *Phys. Scr.*, vol. 65, pp. 167–180, 2001, doi: 10.4172/2157-7544.1000e117.

[2] SCHOTT, *The properties of optical glass*, vol. 29, no. 4. Springer-Verlag, 1998.

[3] R. A. Serway and J. W. Jewett, *Physic for scientists and engineers*, 9th ed. Brooks/Cole, 2013.

[4] S. S. Batsanov, E. D. Ruchkin, and I. A. Poroshina, *Refractive Indices of Solids*. 2016.

[5] V. Kolchinskiy, C. H. Shih, I. Lo, and R. Romashko, “Refractive Index Measurement Using the Laser Profiler,” *Phys. Procedia*, vol. 86, no. June 2015, pp. 176–180, 2017, doi: 10.1016/j.phpro.2017.01.018.

[6] J. D. Bass and D. J. Weidner, “Method for measuring the refractive index of transparent solids,” *Rev. Sci. Instrum.*, vol. 55, no. 10, pp. 1569–1573, 1984, doi: 10.1063/1.1137611.

[7] SCHOTT, “TIE-26 Homogeneity of optical glass,” no. February, pp. 1–12, 2016.

[8] Deepak N.Iyer, “A Michelson interferometric technique for measuring refractive index ...,” Lehigh University, 2006.

[9] M. Ohmi, T. Shiraishi, H. Tajiri, and M. Haruna, “Simultaneous Measurement of Refractive Index and Thickness of Transparent Plates by Low Coherence Interferometry,” *Opt. Rev.*, vol. 4, no. 4, pp. 507–515, 1997, doi: 10.1007/s10043-997-0507-1.

[10] J. J. Fendley, “Measurement of refractive index using a Michelson interferometer,” *Phys. Educ.*, vol. 17, no. 5, pp. 209–211, 1982, doi: 10.1088/0031-9120/17/5/001.

[11] G. Coppola, P. Ferraro, M. Iodice, and S. De Nicola, “Method for measuring the refractive index and the thickness of transparent plates with a lateral-shear, wavelength-scanning interferometer,” *Appl. Opt.*, vol. 42, no. 19, p. 3882, 2003, doi: 10.1364/AO.42.003882.

[12] U. Petzold, R. Jedamzik, P. Hartmann, and S. Reichel, “V-block refractometer for monitoring the production of optical glasses,” *Proc. SPIE 9628*, vol. 9628, pp. 1–5, 2015, doi: 10.1117/12.2191218.

[13] NIST, “Engineering Metrology Toolbox - Refractive Index of Air Calculator.” https://emtoolbox.nist.gov/Wavelength/Ciddor.asp (accessed May 16, 2019).

[14] THORLABS, “HNLS008L-EC, Self-Contained HeNe Laser.” https://www.thorlabs.com/thorproduct.cfm?partnumber=HNLS008L-EC#ad-image-0 (accessed May 20, 2019).

[15] THORLABS, “DCC3240M: High-Sensitivity USB 3.0 CMOS Camera.” https://www.thorlabs.com/thorproduct.cfm?partnumber=DCC3240M (accessed May 20, 2019).

[16] THORLABS, “PDA10A - Si Fixed Gain Detector.” https://www.thorlabs.com/thorProduct.cfm?partNumber=PDA10A (accessed May 20, 2016).

[17] Newport, “URS Series - Precision Rotation Stage,” p. 28, 2018, [Online]. Available: https://www.newport.com/mam/celum/celum_assets/resources/URS_-_User_s_Manual.pdf?1.

[18] Melles Griot, “Broadband Hybrid and Dielectric Cube Beamsplitters,” p. 2, [Online]. Available: http://pdf.datasheet.live/ee1da904/mellesgriot.com/03BSC015.pdf.

[19] P. L. Reu, W. Sweatt, T. Miller, and D. Fleming, “Camera System Resolution and its Influence on Digital Image Correlation,” 2013, doi: 10.1007/s11340-014-9886-y.

[20] Newport, “SMC100CC: Motion Controller, Single-axis DC Motor.” https://www.newport.com/p/SMC100CC (accessed May 20, 2019).

[21] Joint Committee For Guides In Metrology, “Evaluation of measurement data — Guide to the expression of uncertainty in measurement,” 2008. http://www.bipm.org/en/publications/guides/gum.html (accessed Jun. 13, 2019).

[22] EA Laboratory Committee, “EA-4 / 02 M : 2013 Evaluation of the Uncertainty of Measurement In Calibration,” 2013. https://european-accreditation.org/wp-content/uploads/2018/10/ea-4-02-m-rev01-september-2013.pdf (accessed Jun. 13, 2019).

[23] Joint Committee For Guides In Metrology, “International vocabulary of metrology - Basic and general concepts and associated terms (VIM),” 2012. https://www.bipm.org/utils/common/documents/jcgm/JCGM_200_2012.pdf (accessed Jun. 13, 2019).

[24] Newport, “Miniature Steel Linear Stage MFA-CC,” 2018. https://www.newport.com/mam/celum/celum_assets/resources/MFA_Data_Sheet.pdf?1.

[25] R. Xu, Z. Luan, H. Liu, and L. Liu, “Measurement of the diffraction-limit wavefront with double-shearing interferometers,” *J. Opt. A Pure Appl. Opt.*, vol. 8, no. 2, pp. 164–171, 2006, doi: 10.1088/1464-4258/8/2/009.

[26] THORLABS, “N-BK7 High Precision Windows.” https://www.thorlabs.com/NewGroupPage9.cfm?ObjectGroup_ID=1117 (accessed Dec. 18, 2019).

[27] THORLABS, “UV Fused Silica High-Precision Windows.” https://www.thorlabs.com/NewGroupPage9.cfm?ObjectGroup_ID=3983 (accessed Dec. 18, 2019).

[28] A.-S. Bunzli, J.-C. G. & Chauvin, *Handbook on the Physics and Chemistry of Rare Earths Includind Actinides, volume 44*, vol. 12. 2014.

[29] M. N. Polyanskiy, “Refractive Index Database.” https://refractiveindex.info/?shelf=glass&book=SCHOTT-multipurpose&page=B270 (accessed Dec. 18, 2019).

[30] E. Pawar, “A Review Article on Acrylic PMMA,” *ISOR J. Mech. Civ. Eng.*, vol. 13, no. 2, pp. 1–4, 2016, doi: 10.9790/1684-1302010104.

[31] N. Sultanova, S. Kasarova, and I. Nikolov, “Dispersion properties of optical polymers,” *Acta Phys. Pol. A*, vol. 116, no. 4, pp. 585–587, 2009, doi: 10.12693/APhysPolA.116.585.

[32] F. Reitmayer and E. Schuster, “Homogeneity of Optical Glasses,” *Appl. Opt.*, vol. 11, no. 5, pp. 1107–1111, 1972, doi: 10.1364/ao.11.001107.

[33] I. Leite and A. Cabral, “Measurement of the refractive index of glass by optical metrology,” in *Proc.SPIE*, 2019, vol. 11207, doi: 10.1117/12.2530891.

10. Annex

10.1 LabVIEW Codes

Image Filters

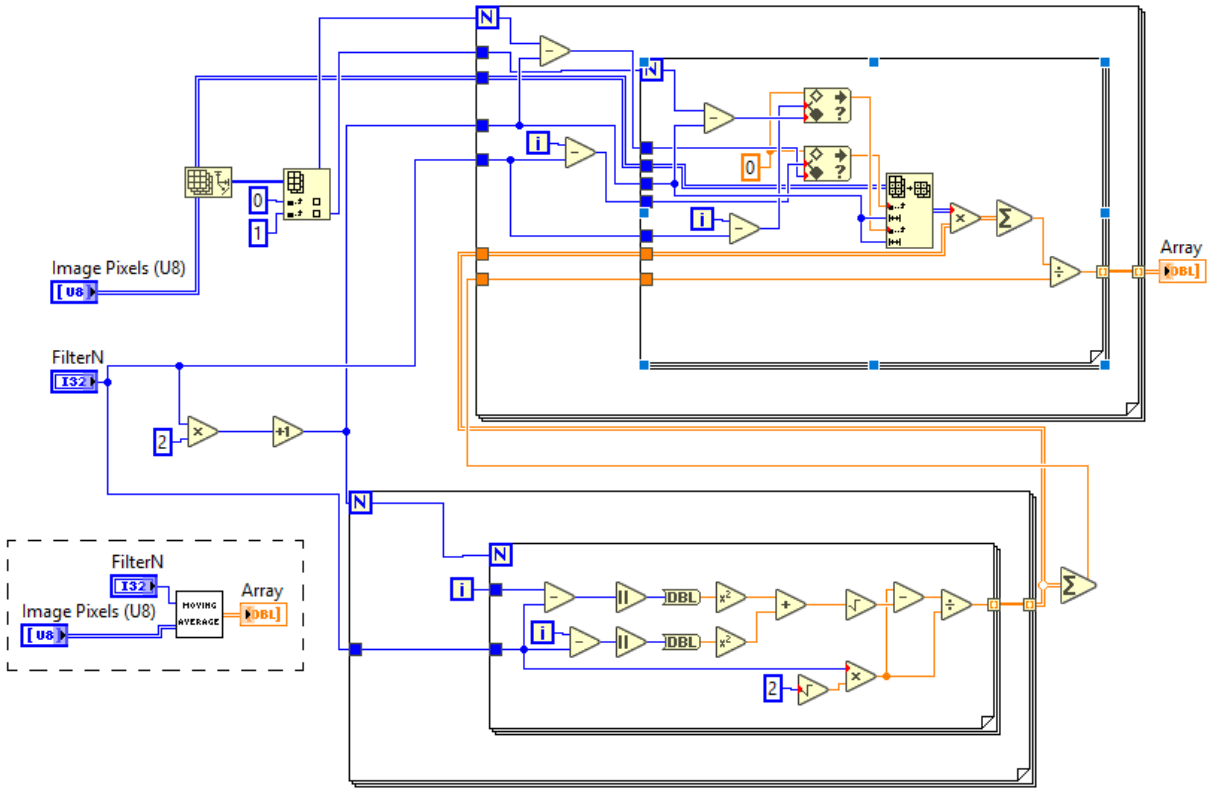

Figure 10.1 – Block diagram of the sub .vi in LabVIEW for the Moving Average filter.

The *Moving Average* filter (Figure 10.1) evaluates every pixel value and, in accordance with the user defined *FilterN* value it performs a moving average, "smoothing" the effects of unwanted reflections (Figure 5.4, bottom).

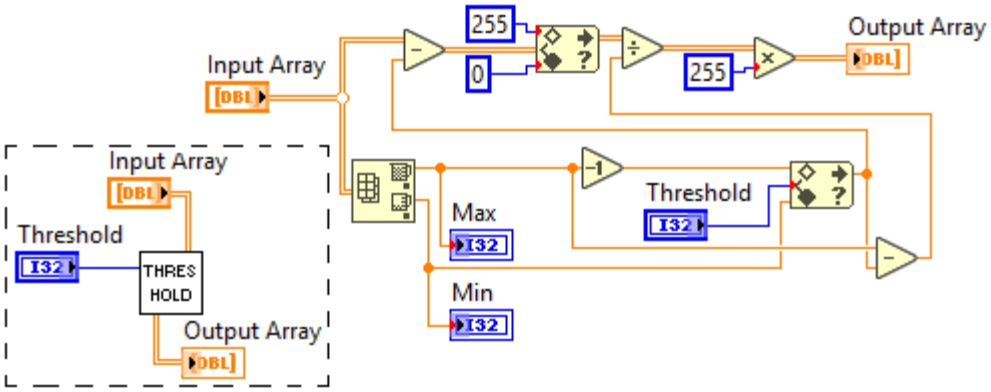

Figure 10.2 – Block diagram of the sub .vi in LabVIEW for the Threshold filter.

After passing through the *Moving Average*, if the spot size is too big or still irregular, the user can apply a threshold to the array that coerces every pixel value to fall within a fixed range, adjusted to the maximum and minimum values of the array (Figure 5.4).

Method to find the spot centre *xy* coordinates

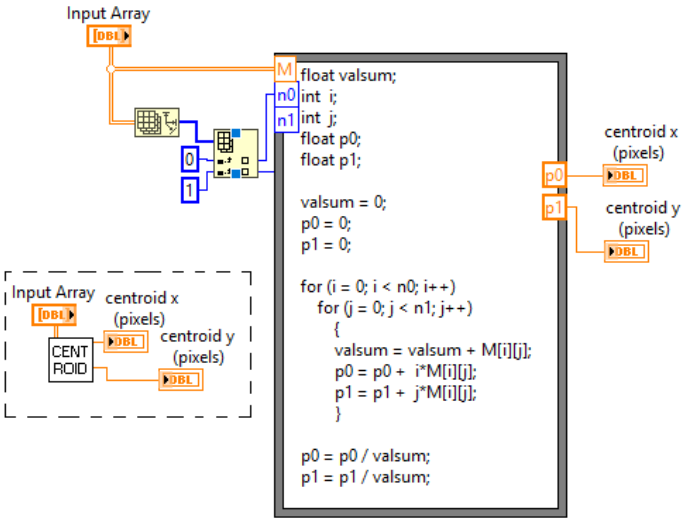

Figure 10.3 – LabVIEW code to calculate the centroid of an input 2D array. On the left corner in a box is the LabVIEW .vi that contains the code.

The centroid of a shape (in this case, the laser spot which is translated by the camera in pixels) is simply the weighted average of all the pixels constituting the shape (it can also be called the determination of the shapes' "centre of mass"). Because the captured image is rendered as 2D array of pixel values, the centroid of the image has *x* and *y* coordinates as well. In LabVIEW (), a simple code accepts a 2D data array and proceeds to compute the weighted average of the intensity peak (because this particular camera is monochrome) in *x* and *y*, therefore outputting the *x* and *y* coordinates of the centroid $C_{[x,\,y]}$, identified in Figure 10.3 as *p0* and *p1* respectively. This method presents a disadvantage if used to calculate the centroid of an irregular shape. For instance, if an image has an irregular spot (Figure 5.9), a simple code accepts a 2D data array and proceeds to compute the weighted average of the intensity peak (because this particular camera is monochrome) in *x* and *y*, therefore outputting the *x* and *y* coordinates of the centroid $C_{[x,\,y]}$, identified in Figure 10.3 as *p0* and *p1* respectively. This method

presents a disadvantage if used to calculate the centroid of an irregular shape. For instance, if an image has an irregular spot (Figure 5.9), this method will determine the “centre of mass”, which may decrease the accuracy of the method.

The Gaussian method, although more complex (compared to the centroid method), is another approach to determine the centre of a spot. The method begins by determining the point of maximum intensity by using the centroid method already described. Next, data horizontal and vertical cuts, column (x) and row (y) intensity value vectors, are made using that point as reference and a Gaussian fit is made to each vector – this pinpoints a new xy coordinate for the spot centre. To improve the accuracy, new equally spaced horizontal and vertical lines are cut and again the Gaussian fit is applied to the x and y vectors – by doing this, a set of values, vertical and horizontal maximums, are identified and a linear regression is made on x and y. The Gaussian spot centre corresponds to the intersection between these two lines.

Figure 10.4 – Block diagram of the first case structure executed by the program. Both the camera and the stage are initialized and a while loop continuously displays the captured image (real time), allowing the user to change some parameters.

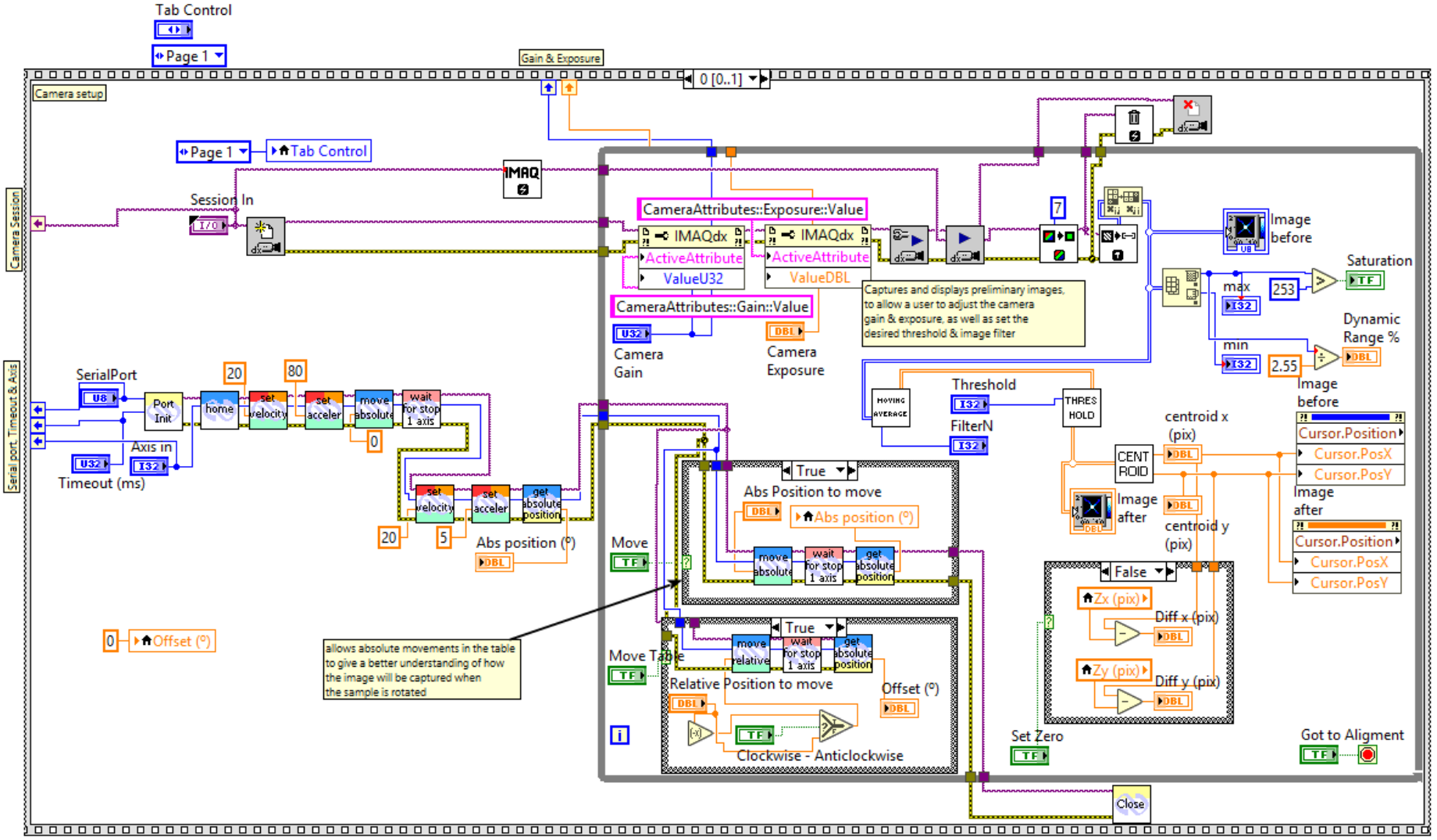

Figure 10.5 – Block diagram of the first frame of the second case structure executed by the program. The program allows the user to change some parameters, and accordingly updates others automatically. This loop ends when the user presses the button that initiates the automatic measuring procedure.

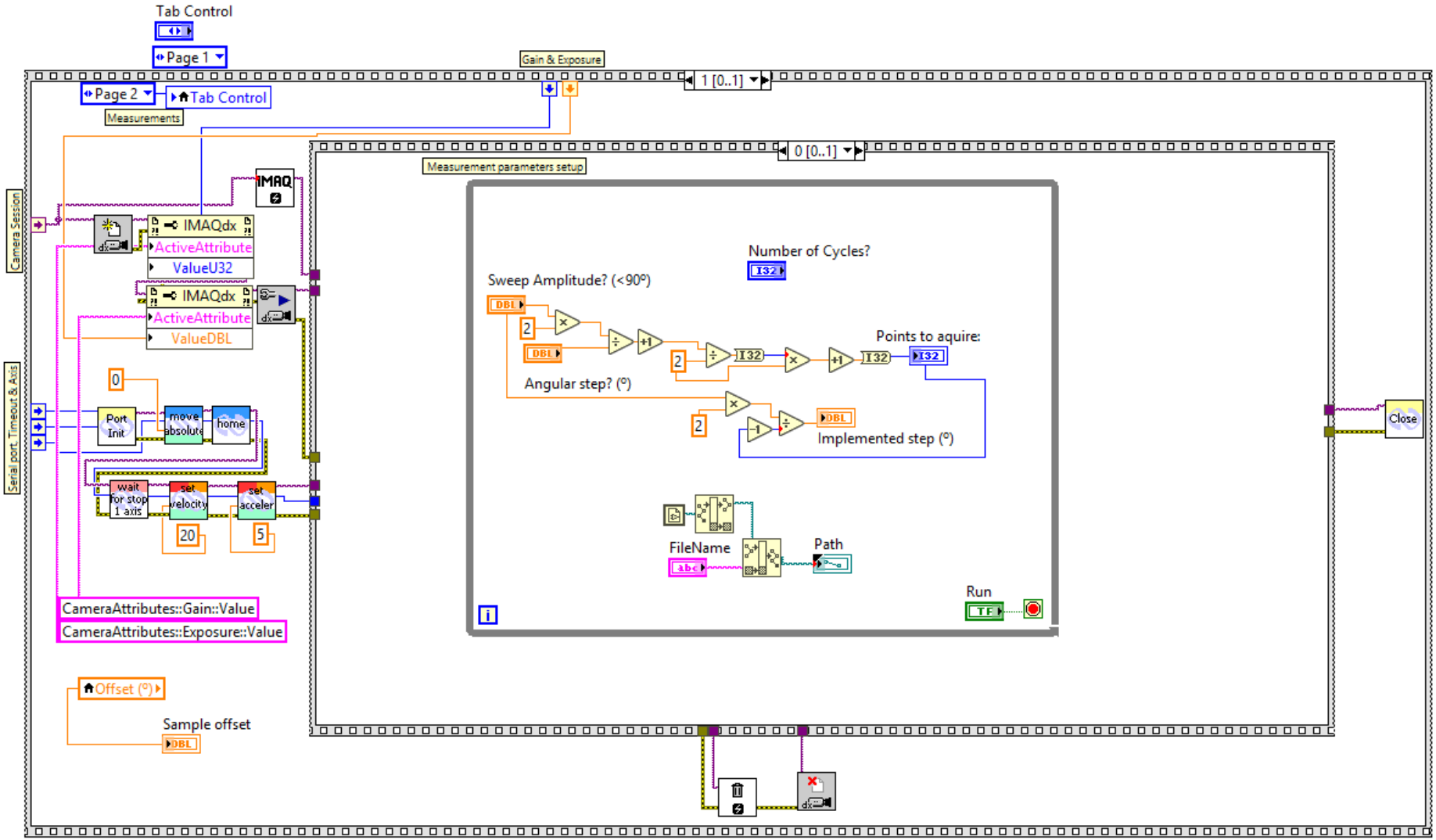

Figure 10.6 – Block diagram of the second frame of the second stacked case structure. Two for cycles are nested, the first sets the stage to the lower limit of the sweep and the second (here depicted with the first frame of its case structure) moves the stage an implemented step forward, while also calculating the current progress and estimated time left.

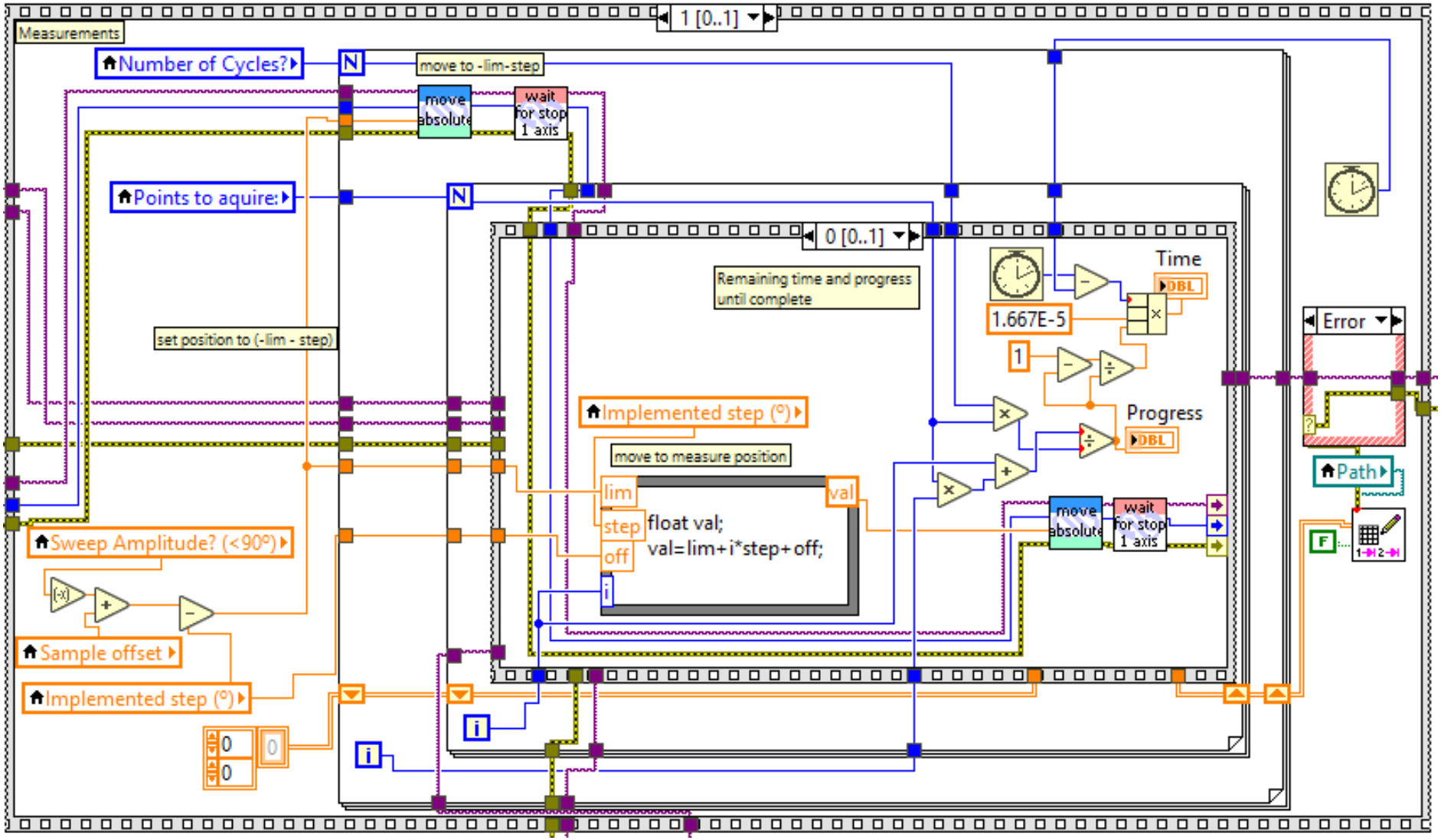

Figure 10.7 – Block diagram of the third frame of the second stacked case structure. Two for cycles are nested, the first sets the stage to the lower limit of the sweep and the second (now showing the second frame of its case structure) captures an image, determines its centroid coordinates and creates a new data row in the data array later used to determine the values of d.

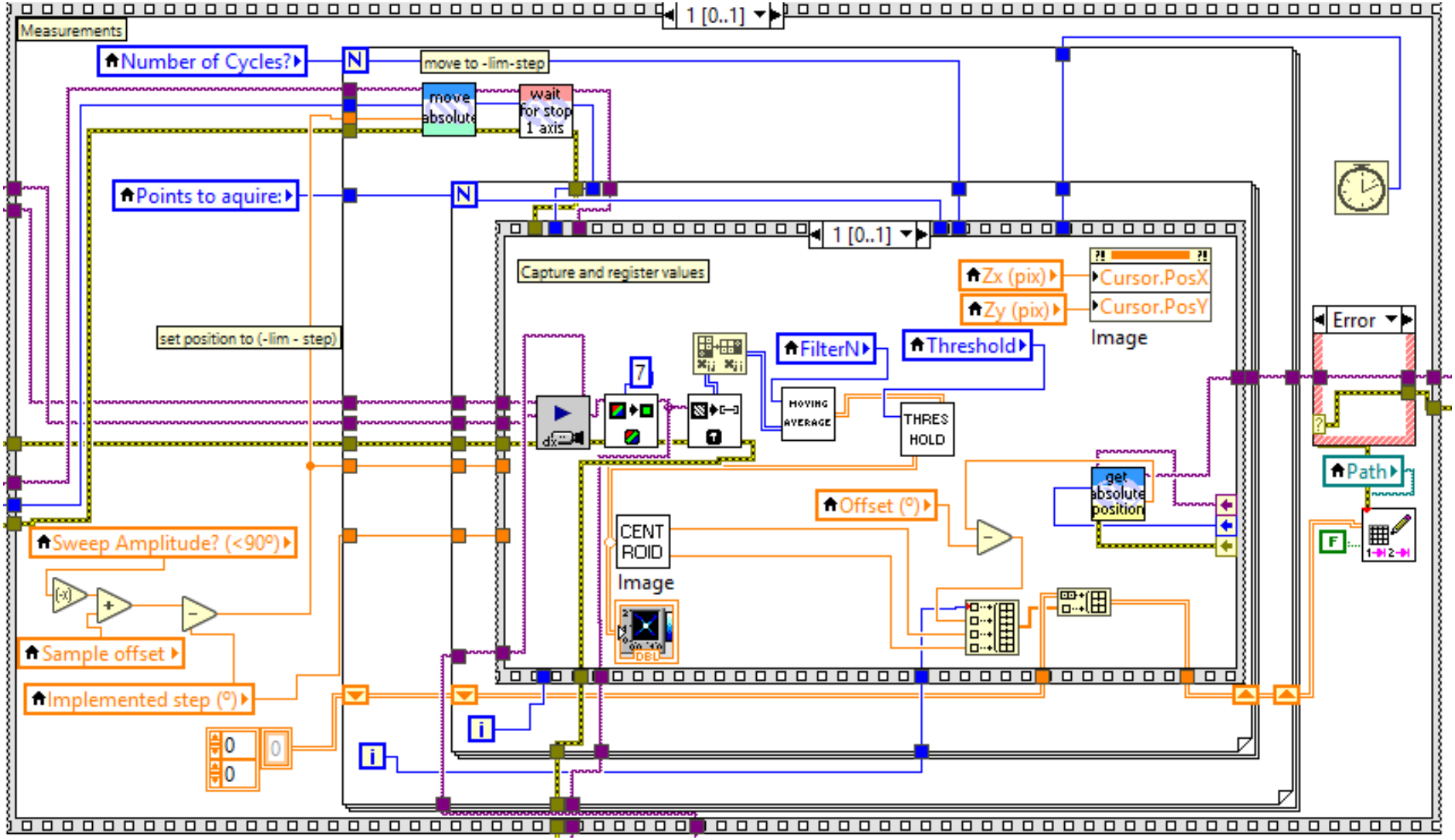

Figure 10.8 – Excel spreadsheet where the user inserts the sample thickness and spot centre coordinate measurements.

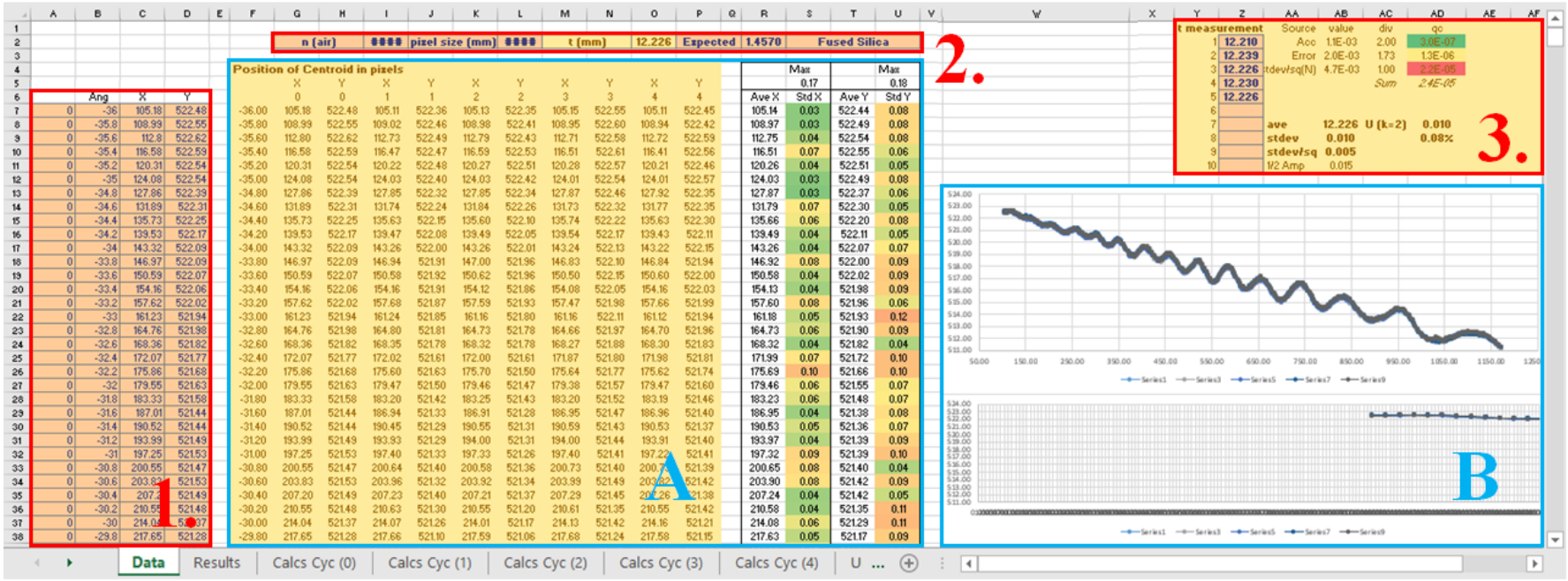

1	Data from the excel exported by LAbVIEW
2	[Orange] Values for n_{air}, pixel size and expected value for n_{glass} (if known)
3	Manual measurements of the sample thickness
A	5 cycle measurements (yellow) ; average and stdev for *x* and *y*, for every angle
B	Visualization of the (x;y) coordinates movement for every sweep/cycle

Figure 10.9 – Excel spreadsheet that calculates the lateral displacement, refractive index and angle offset for one sweep.

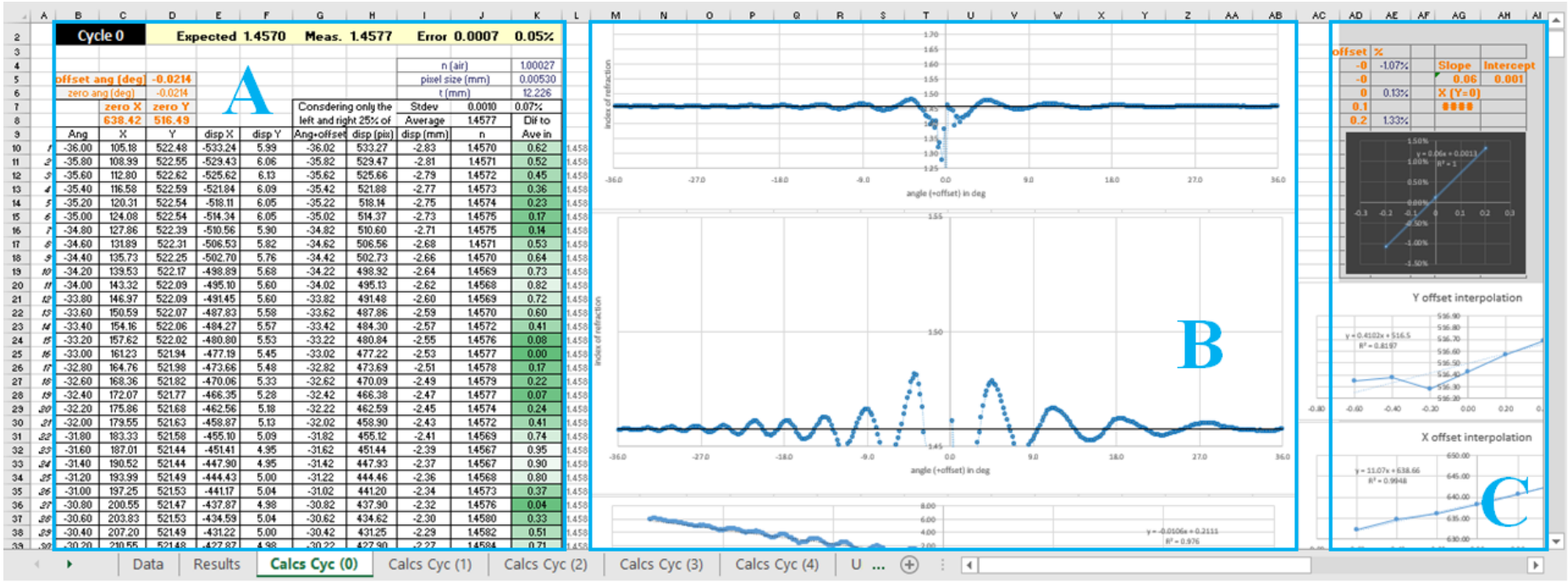

A	Computation, for every angle, of the value of *d* and n_{glass} (average, stdev and error)
B	Visualization of the value of n_{glass} versus the incident angle
C	Computation of the value of the angular offset

Figure 10.10 – Excel spreadsheet that calculates average value and expanded uncertainty of the refractive index, for one sweep.

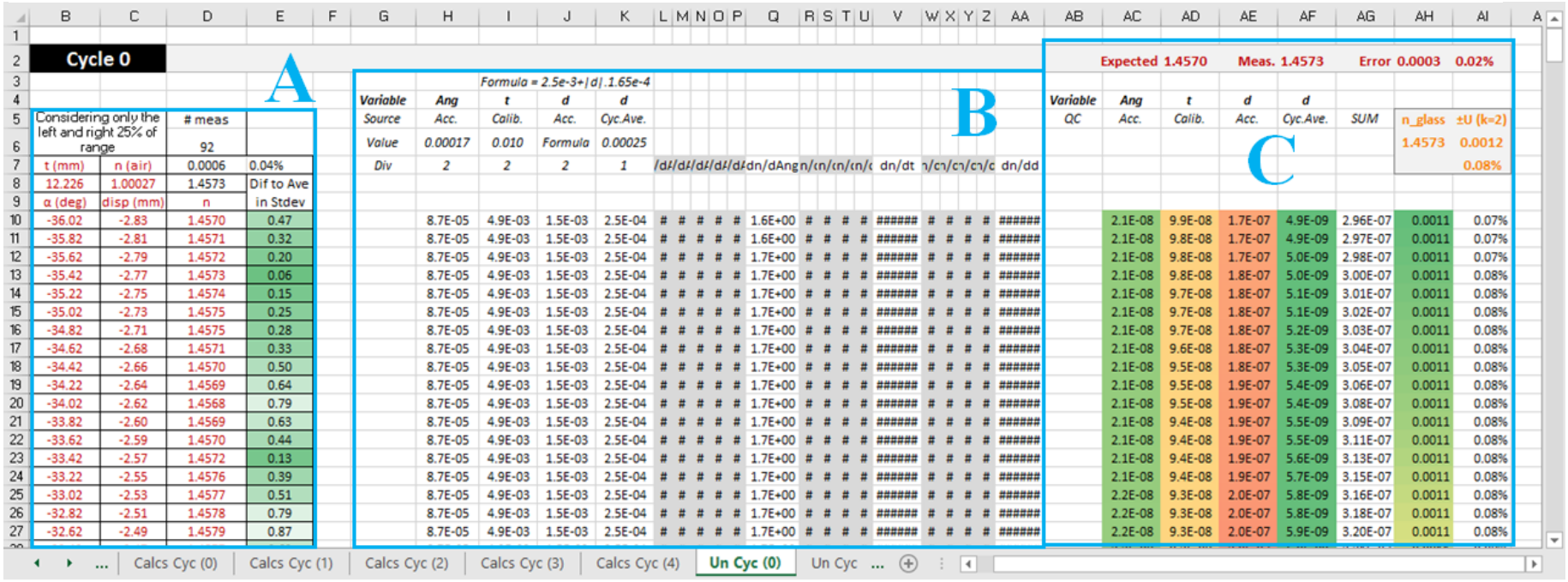

A	Computation of the value of d and n_{glass} (average, stdev and error), considering only the left and right 25% of range
B	Visualization of the uncertainty, for every considered angle value, in θ_i, *t* and *d*. Computation of the partial derivatives
C	(Top) Expected and measured values and associated uncertainty and error (Bottom)Quadratic component of every uncertainty parameter, their sum and expanded uncertainty for every considered angle value.

Figure 10.11 – Excel spreadsheet that displays the results of every sweep and calculates the average, uncertainty and error of the refractive index, of a 5 sweep test.

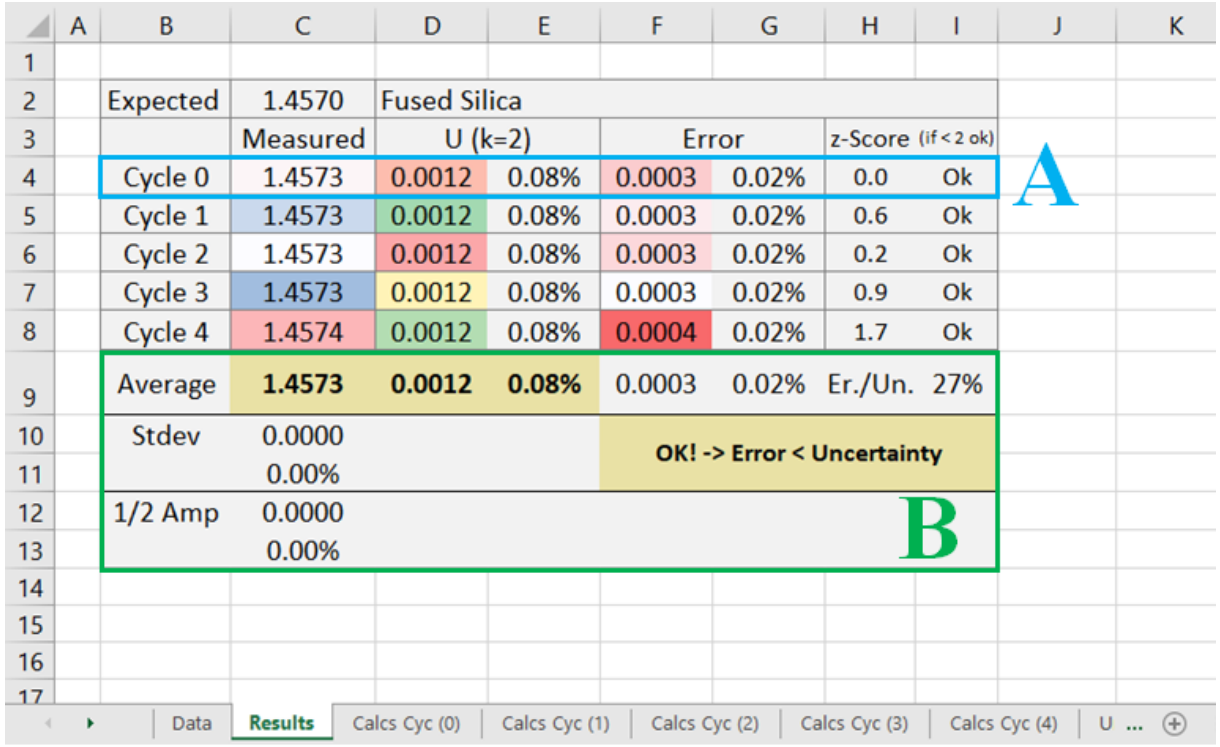

1									
2		Expected	1.4570	Fused Silica					
3			Measured	U (k=2)		Error		z-Score (if < 2 ok)	
4		Cycle 0	1.4573	0.0012	0.08%	0.0003	0.02%	0.0	Ok
5		Cycle 1	1.4573	0.0012	0.08%	0.0003	0.02%	0.6	Ok
6		Cycle 2	1.4573	0.0012	0.08%	0.0003	0.02%	0.2	Ok
7		Cycle 3	1.4573	0.0012	0.08%	0.0003	0.02%	0.9	Ok
8		Cycle 4	1.4574	0.0012	0.08%	0.0004	0.02%	1.7	Ok
9		Average	**1.4573**	**0.0012**	**0.08%**	0.0003	0.02%	Er./Un.	27%
10		Stdev	0.0000			**OK! -> Error < Uncertainty**			
11			0.00%						
12		1/2 Amp	0.0000						
13			0.00%						
14									
15									
16									
17									

A

B

Data | **Results** | Calcs Cyc (0) | Calcs Cyc (1) | Calcs Cyc (2) | Calcs Cyc (3) | Calcs Cyc (4) | U ...

A	Results summary of Calcs Cyc (0) & Un Cyc (0)
B	Final 5 cycle average results for the value of $n_{glass} \pm U$

10.3 Published Work

[33] **PAPER I**

Measurement of the refractive index of glass by optical metrology

Inês Leite, Alexandre Cabral

Proceedings Volume 11207, Fourth International Conference on Applications of Optics and Photonics; 112072P (2019) https://doi.org/10.1117/12.2530891

IV International Conference on Applications of Optics and Photonics, 2019, Lisbon, Portugal

Measurement of the Refractive Index of Glass by Optical Metrology

Inês Leite[a], Alexandre Cabral*[a,b]

[a]Faculdade de Ciências da Universidade de Lisboa, Departamento de Física, Campo Grande 1749-016 Lisboa Portugal

[b]Instituto de Astrofísica e Ciências do Espaço, Universidade de Lisboa, Campo Grande 1749-016 Lisboa Portugal

ABSTRACT

New luminescent materials have a wide range of applications in either chemistry, biology or electronics. The study of non-toxic and inexpensive luminescent materials is the key to a sustainable future. Luminescent solar concentrators are the example of a very promising application of luminescent materials and the optimization of the optical conversion efficiency of the glasses produced is essential for the development of the luminescent solar concentrators - for this it is necessary to determine the refractive index of the different glasses. There are many existing techniques for determining the refractive index - the current situation regarding systems that perform this type of measurements is that there are simple systems for low accuracy and complex systems for high accuracy of results, and the middle ground is often left unexplored. For the manufacture of luminescent solar concentrator glass, it is important to have access to a simple refractive index measurement system with an uncertainty of less than 1%. The system should be simple to implement, cost-effective and automated to allow a typical user to obtain the desired information on optically simple samples. Two independent techniques for measuring the refractive index are approached, one using the lateral displacement of a laser beam and the other the interferometric pattern obtained by an interferometer.

Keywords: refractive index, lateral displacement, interferometry, glass, luminescent solar concentrator, optical metrology.

1. INTRODUCTION

New luminescent materials have a wide range of applications in chemistry, biology or electronics. Lighting devices, chromophores and solar cells are an important part of our day-to-day life, but often require organic compounds, which are sometimes susceptible to degradation processes, toxic elements or expensive raw materials such as rare earths, indium, ruthenium or iridium. The study of non-toxic and inexpensive luminescent materials is the key to a sustainable future.

Luminescent Solar Concentrators (LSC) are the example of a very promising application of luminescent materials. The optimization of the optical conversion efficiency of the glasses produced is essential for the development of the LSC and for this it is necessary to determine the refractive index (RI) of the different glasses.

Existing techniques for determining the refractive index that produce results with a high accuracy, in the order of 10^{-5} (beyond what is necessary in the development of LSC), involve the construction of optical prisms with very tight manufacturing tolerances and are associated to very high manufacturing costs. There is also the possibility of using ellipsometry techniques, which can produce results with an accuracy of 10^{-4}, but require that the surface of the sample be extremely polished, and some contamination or corrosion of the surface can affect the results obtained. In addition, it is necessary to use an optical model that often makes data analysis quite complex.

For the manufacture of LSC glass, it is important to have access to a simple refractive index measurement system with an uncertainty of less than 1%. It has been noted that the current situation regarding systems that perform this type of measurements is the existence of simple systems for low accuracy and complex systems for high accuracy of results. From this need, and opportunity, came the idea of creating an intermediate system capable of filling the apparent technological gap between these two extremes. The system should be simple to implement, cost-effective and automated to allow a typical user to obtain the desired information on optically simple samples.

*alexandre.cabral@ciencias.ulisboa.pt; phone 351 217 500 753; www.ciencias.ulisboa.pt

1.1 LSC Glasses

LSC glass absorbs sunlight and emits radiation at a given wavelength, which is directed through total internal reflection (TIR) for photovoltaic cells mounted at the corners of the LSC. These LSC can be transparent inorganic glasses, which have intrinsically high durability and are synthesized from widely available resources. With these characteristics they can be used as windows in which photovoltaic cells can be integrated, allowing the capture of solar energy. It is fundamental to be able to produce Luminescent Solar Concentrators using economical raw materials and through low complexity/cost characterization processes.

The efficiency of producing solar energy through a window made of LSC glass has a strong dependence associated with the radiation captured by the photovoltaic cell. The radiation captured, in turn, depends on the angle from which the radiation produced by luminescence is reflected by the inner faces of the glass plate, due to Total Internal Reflection (TIR) until reaching the cell and being absorbed. The efficiency of energy production therefore depends on the refractive index of the LSC glass, n_{glass} that has direct influence over the critical angle, θ_c for TIR to occur.

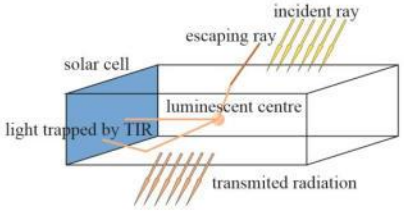

Figure 1. Simple representation of the application of a LSC glass to a window, for the production of solar energy.

1.2 Measuring Techniques Applicable to Glass

The refractive index (RI) is defined by the velocities of light in the media where it propagates, being an indication of the optical density of this medium. Its determination depends on simple concepts of optics and there are several techniques of optical measurement of the RI based on the reflection or transmission of light from a surface, among them interferometry, reflectometry and ellipsometry. Depending on the technique and method used, it is also possible to determine other relevant properties of a sample, such as surface roughness, material uniformity or its thickness.

The velocity of a monochromatic beam of light in a material medium differs from the velocity in the vacuum. If the velocities of light in vacuum and in the medium are respectively c and v, the ratio c/v is defined as the refractive index, n, of the medium: $n = c / v$. An optical path (OP) is defined as the product of the geometric distance and the refractive index of the medium. Snell's law is used to describe the relationship between incident and refracted angles when referring to a beam of light passing through a boundary between two different isotropic means, such as water, glass, or air: $n_1 . sin(\theta_i) = n_2 . sin(\theta_r)$. In the phenomenon of total internal reflection, light crosses an interface between two media with different refractive indexes n_1 and n_2 such that $n_1 > n_2$. As the angle of incidence increases, the angle of refraction also increases with respect to the normal. When the angle of incidence reaches a value known as critical angle θ_c, the refracted rays travel along the surface of the medium, and for $\theta > \theta_c$, internal reflection occurs. The critical angle can be calculated from Snell's law.

Currently, there are several methods and configurations that allow the measurement of the refractive index of glass blocks. It can be measured through the deviation pattern created by refraction, interferometric methods or ellipsometry. Existing techniques for determining the refractive index produce results with an uncertainty that is typically in the interval from 10^{-2} to 10^{-5}. Results with reduced uncertainty, in the order of 10^{-5} or below (beyond what is necessary in the development of LSC), involve the construction of optical prisms with very tight manufacturing tolerances and are associated to very high manufacturing costs. There is also the possibility of using ellipsometry techniques, which can produce results with an accuracy of 10^{-4}, but the samples must be extremely polished and some contamination or corrosion of the surface can affect the results obtained. In addition, it is necessary to use an optical model that often makes data analysis quite complex.

The analysis of several existing techniques was conducted (Table 1) and some comparisons were made: the method used, the uncertainty obtained in RI measurement, the complexity of the method (qualitative scale) and the possibility of optimization based on automated measurement techniques, improvements in the alignment system, etc..

Table 1. Summary of some techniques researched, associated uncertainties, complexity and possibility optimization to achieve the proposed objectives.

Method	Uncertainty in n	Complexity	Possibility of Optimization	Reference
Lateral Displacement	10^{-2} to 10^{-3}	Low – High	Yes	**[1]**
Interferometry				
(simple)	10^{-2} to 10^{-3}	Low – Medium	Yes	**[2, 3]**
(with piezoelectric modulation)	10^{-3}	High	No	**[4]**
(with wavelength modulation)	10^{-4}	High	No	**[5]**
Prism	10^{-3} to 10^{-5}	High	No	**[6, 7]**

In a first approach, all the techniques presented satisfy the requirement to obtain an uncertainty for the RI value greater than 10^{-2}. However, some are not the most appropriate to implement, as is the case with techniques using the prism method ([6] and [7]), which despite the high accuracy of the obtained results, resort to techniques that are too complex. Likewise, due to their high degree of complexity, techniques [4] and [5], respectively, a piezoelectric modulating interferometer and a wavelength modulated interferometer do not correspond to the type of system to be implemented, nevertheless in the future there may exist the need to consult such techniques, being that the reason by which they are kept in this table.

For the remaining techniques, lateral displacement[1] and interferometry[2][3], the uncertainty associated with the measurements lies in the range of 10^{-2} to 10^{-3} - however, the uncertainty indication in the majority of the articles is not concise and in some cases may have been incorrectly defined, so it is considered prudent not to place total confidence in the values obtained for uncertainty - considering them more as guidelines and not certainties.

Comparing the two techniques of interferometry, both use a Michelson interferometer, assuming however the knowledge in advance of some property of the plate that is used - either the material or its thickness. Two major differences between the two methods lie in reading the angle of incidence and observing the interference pattern: done manually[3] with an uncertainty at the angle of ±0.25° and manual counting by the user of the number of fringes of the pattern of interference, and automatically[2] (with an uncertainty of ±0,001° in the measured angle and the automatic acquisition of the interference pattern through a detector/oscilloscope). However, the uncertainty obtained for the RI is greater in the latter, perhaps associated to the degree of complexity of the whole process, which translates into an increase of sources of uncertainty that, if not properly minimized, limit the uncertainty of the results obtained.

Another possibility of measuring the RI is through the lateral displacement method[1] - the uncertainty associated with the RI in this article is in the order of magnitude of 10^{-3} and the technique described presents an interesting possibility of measuring the RI of the sample through the capture of the beam by a CCD camera, requiring however the prior knowledge of the thickness and geometry of the plate in study.

2. IMPLEMENTATION METHODS

After this initial study of available techniques, two families of methods were considered – refraction and (simple) interferometry – whose uncertainties lie in an approximate range from 10^{-2} to 10^{-3} and are compatible with the objective uncertainty in the value of the refractive index of LSC glass. Associated to the first technique is the method by measurement of the glass refractive index from optical lateral displacement, and associated to interferometry is the measurement of the glass refractive index from the interferometric optical path difference. In the study of either technique, a simple scheme was produced (Figure 2) to help understand what happens to the beam when it passed through the glass plate, tilted by an angle θ_i.

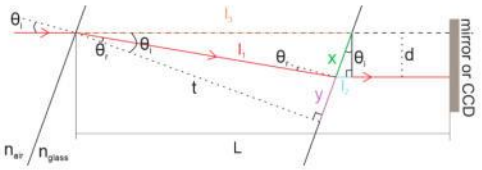

Figure 2. Simple scheme that illustrates the path of a displaced beam inside a glass plate of thickness t by an angle θ_i, displaced a distance d, from the original beam path.

An appropriate setup was drafted to allow the test of both techniques with little change of used parts. It required a simple yet effective design that could accommodate the automatic rotating table with the glass sample, the mirrors, beam splitter, a lens and detector needed for the interferometric technique, as well as the CCD camera used to measure the optical displacement of the beam after it crossed the plate. One problem was observed from the fact that by placing the camera after the glass plate, when changing to the interferometric technique, said camera obstructed the path of the measuring arm – it was solved using a part that allowed the translation of the camera away from the beam path whenever required, as seen in Figure 3. Due to the intensity of the beam, a neutral filter had to be used when taking measurements of the lateral displacement, as seen next to the CCD in Figure 2 (right).

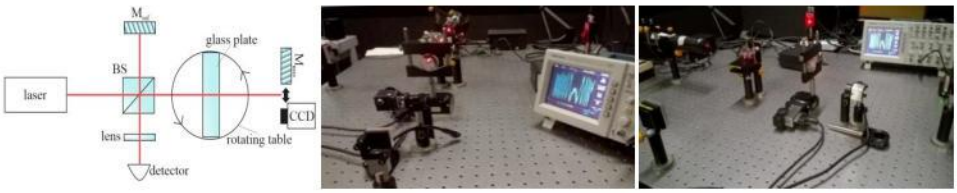

Figure 3. Schematic of the desired setup (left) and experimental setup to test both techniques (center and right).

2.1 Lateral Displacement Method

When a beam passes through a glass plate with parallel flat surfaces, such as a window, the ray emerges parallel to its original direction, but laterally displaced by a certain distance d, which increases with the angle of incidence θ_i. If we apply Snell's law and some simple trigonometric functions to the propagation beam, we can obtain the following relation between the displacement d, the thickness t, the angle of incidence θ_i and the RI of glass n_{glass} (Equation 1).

$$d = t \sin\theta_i \sqrt{1 - \frac{\cos\theta_i}{\left(\frac{n_{glass}}{n}\right)^2 - \sin^2\theta_i}} \tag{1}$$

A CCD camera is used to measure the lateral displacement of the beam that occurs when the glass plate is rotated – by capturing the beam after it crosses the plate it is possible to discover how much it was displaced from the position where $\theta_i = 0°$. The measurement can be done for a sequence of incident angles (positive and negative) allowing the reduction of the uncertainty by averaging

2.2 Interferometric Method

A Michelson interferometer (MI) is used to measure the difference in optical path length created by rotating the glass plate located in one of the arms. In the MI, the primary wave is divided into two secondary waves that have the same structure as the primary wave. Secondary waves propagate through distinct trajectories (usually referred to as reference arm and measuring arm) and subsequently are recombined to create an interference pattern. This pattern between the two linearly polarized and monochromatic waves has an intensity that depends on the optical path difference (OPD) of the recombined beam which in turn can be measured by the number of fringes that are picked off by a detector, according to Equation 2.

$$I_{OPD(t)} = I_1 + I_2 + 2\sqrt{I_1 I_2}\cos\left(\frac{2\pi}{\lambda} OPD(t)\right) \tag{2}$$

Where I_1 and I_2 are the individual intensities of the two beams and λ the wavelength of the light emitted by the laser. During the measurement process, a glass plate is placed in the measuring arm and is continuously rotated, changing the optical path difference and thus producing a fringe pattern related to the angle of incidence. According to Figure 2, the OPD is found by the path difference when $\theta_i = 0^o$ and $\theta_i \neq 0^o$. By measurement the OPD, n_{glass} can be determined solving the following equation.

$$OPD = 2\left[\left(Ln_{air} - t\left(n_{air} - n_{glass}\right)\right) - \left((L - l_3 + l_2)n_{air} + l_1 n_{glass}\right)\right] \quad (3)$$

Replacing l_1, l_2 and l_3 by their trigonometric relationship with the incident angle, we obtain the following equation that can be solved for n_{glass}.

$$OPD = 2t\left[\left(\frac{n_{glass}}{\cos\theta_r} + n_{air}\left[(\tan\theta_i - \tan\theta_r)\sin\theta_i + \frac{L}{t} - \frac{1}{\cos\theta_i}\right]\right) - \left(\frac{L}{t}n_{air} + (n_{glass} - n_{air})\right)\right] \quad (4)$$

2.3 Trade-off between lateral displacement and interferometric measurements

A mathematical model of both techniques was developed in order to better understand the contribution of each parameter (incident angle, θ_i, thickness of the plate, t, and lateral displacement, d or optical path difference, OPD) to the determination of n_{glass}, and to determine the level of uncertainty needed in each of them in order to achieve measurements of the RI with an uncertainty in n_{glass} from 1% to 0.1% (the objective and a goal).

Figure 4 and Figure 5 show the requirements in the uncertainty of all the parameters to obtain the uncertainty in RI. The relation uncertainty in parameter / uncertainty in n_{glass} is linear in all cases. In the case of the lateral displacement technique, in order to obtain an overall uncertainty in n_{glass} equal or below 1%, it is required to have an uncertainty in the measurements of θ_i, t and d below, respectively, ± 0.3°, ± 120 µm and ± 19 µm. If we wish to have measurements with an error equal or below 0.1% the value of uncertainty for these three parameters must decrease to ± 0.02°, ± 10 µm and ± 2 µm, respectively. To achieve an uncertainty in the measurement of the refractive index of glass equal or below 1% with the interferometric technique, the uncertainty needed in the measurements of θ_i, t and OPD (measured in fringes detected, according to wavelength) are respectively, ±0.18°, ±130 µm and ±19 fringes. An error equal or below 0.1% can be achieved if the uncertainty in each measurement is, respectively ±0.02°, ±10 µm and ±2 fringes.

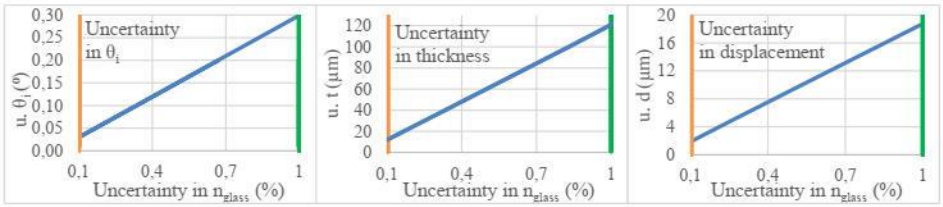

Figure 4. Evaluation of the uncertainty (u.) with the lateral displacement technique of the measurements of θ_i, t and d, respectively, required to keep the uncertainty of n_{glass} equal or below 1%.

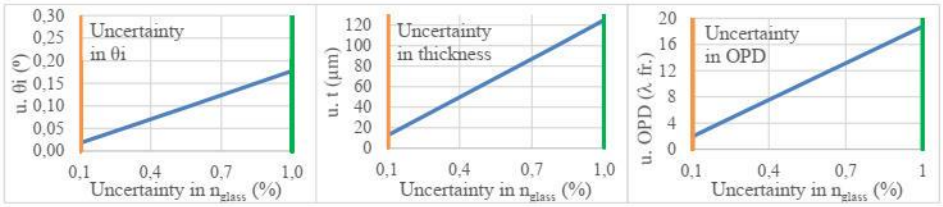

Figure 5. Evaluation of the uncertainty (u.) with the interferometer of the measurements of θ_i, t and OPD, respectively, required to keep the uncertainty of n_{glass} equal or below 1%.

The requirement on the thickness are identical to both techniques.

In terms of incident angle, the interferometric technique requires a reduced uncertainty by a factor of 2. It should be noted that a typical accuracy for an automated rotation stage is higher than 0.01°, therefore making the requirement on the interferometric technique for 0.1% uncertainty in RI not easy to achieve.

in θ_i whereas the lateral displacement technique allows a higher uncertainty to achieve an uncertainty in n_{glass} equal or below 1%.

When it comes to the detected parameter – d or OPD – the uncertainty for the latter is well within standard values (for 1% and 0.1%) of fringe detection for interferometric techniques, while the detection of the lateral displacement on the other hand begins to be limited when nearing the 0.1% goal we reach a requirement of half a pixel for a 5 μm pixel. This is nevertheless achievable.

The spurious reflection from the plate surfaces play an important role on the trade-off (note that the samples will not have any anti-reflection coating.). Although the interferometric configuration is in theory more sensible and accurate in the measurement of path differences, in practice it can become quite challenging to achieve stable systematic results. The interferometer itself requires careful alignment, in its mirrors and in the beam splitter to avoid undesired reflection. The reflections from the plate in tests cannot be avoided and when the glass surface becomes close to being perpendicular to the incoming beam, an additional interference pattern is overlapped and also captured by the sensor. This noisy effect is basically impossible to detach from expected signal.

This effect also affects the lateral displacement technique, creating a non-symmetric spot image. Nevertheless, by using, for example, a Gaussian fit to the laser spot image instead of a simple centroid calculation, reduces significatively the influence of this spurious reflection (and the process can even be optimized with other image processing techniques).

CONCLUSION

Despite the trade-off analysis between the techniques, after making some simple acquisition tests it became clear that the extra sensibility that an interferometer has to offer can become problematic and unnecessarily increase the overall complexity of the measurements of the RI of the glass plates. Although the interferometric configuration is in theory more sensible and accurate in the measurement of path differences, in practice it can become quite challenging to achieve stable systematic results.

The complexity of the interferometric technique is also considerable when compared to the lateral displacement: the later does not require any stabilized optical table and for wavelength selection we are not limited to coherent sources.

The main limitation on the lateral displacement is the resolution displacement measurement, limited by the pixel size of the CCD. There is, nevertheless, several improvements on this area based on the image processing and result of averaging a considerable number of acquisitions (easy to be done as the system is automated).

The next steps in this work are the implementation of a small size optical bench based on lateral displacement, all automated, and the development of all the data analysis. Another following area of research is the possibility to optimize the determination of the glass plate thickness and the offset in the angle of rotation by the analysis of the acquired data.

ACKNOWLEDGMENTS

This work was supported by the Science and Technology Foundation (FCT, Portugal) through the research grants UID/FIS/04434/2019, PTDC/FIS-AST/29245/2017 and PTDC/FIS-AST/1526/2014.

REFERENCES

[1] Kolchinskiy V., Shih C. H., Lo I., and Romashko R., "Refractive Index Measurement Using the Laser Profiler," *Phys. Procedia*, vol. 86, no. June 2015, pp. 176–180, 2017.

[2] N.Iyer D., A Michelson interferometric technique for measuring refractive index of sodium zinc tellurite glasses Lehigh University, 2006.

[3] Fendley J. J., "Measurement of refractive index using a Michelson interferometer," *Phys. Educ.*, vol. 17, no. 5, pp. 209–211, 1982.

[4] Ohmi M., Shiraishi T., Tajiri H., and Haruna M., "Simultaneous Measurement of Refractive Index and Thickness of Transparent Plates by Low Coherence Interferometry," *Opt. Rev.*, vol. 4, no. 4, pp. 507–515, 1997.

[5] Coppola G., Ferraro P., Iodice M., and De Nicola S., "Method for measuring the refractive index and the thickness of transparent plates with a lateral-shear, wavelength-scanning interferometer," *Appl. Opt.*, vol. 42, no. 19, p. 3882, 2003.

[6] Petzold U., Jedamzik R., Hartmann P., and Reichel S., "V-block refractometer for monitoring the production of optical glasses", Proc. SPIE 9628, 2015

[7] Bass J. D. and Weidner D. J., "Method for measuring the refractive index of transparent solids," Rev. Sci. Instrum., vol. 55, no. 10, pp. 1569–1573, 1984